universität
wien

MASTERARBEIT / MASTER'S THESIS

Titel der Masterarbeit / Title of the Master's Thesis

„Bound Entanglement Detection via GSIC- and SIC-POVMs & Identification of Separable States in the Magic Simplex"

verfasst von / submitted by

Alexander Hübner, BSc

angestrebter akademischer Grad / in partial fulfilment of the requirements for the degree of

Master of Science (MSc)

Wien, 2023 / Vienna, 2023

Studienkennzahl lt. Studienblatt / degree programme code as it appears on the student record sheet:	A 066 876
Studienrichtung lt. Studienblatt / degree programme as it appears on the student record sheet:	Masterstudium Physics
Betreut von / Supervisor:	Mag. Dr. Beatrix Hiesmayr, Privatdoz.

Abstract

In bipartite quantum systems, a separability problem deals with the question of whether a quantum state is separable or entangled. An important approach to solving such a problem is the Peres-Horodecki criterion, which constitutes a necessary and sufficient condition for separability in 2×2 and 2×3 systems. However, in higher dimensions, separability problems are complicated by the occurrence of bound entanglement. This term refers to a distinct type of entanglement that cannot be used to distill maximally entangled states through local operations and classical communications.

Even though the Peres-Horodecki criterion fails to recognize bound entanglement, there exist criteria that detect subsets of these states. In this context, necessary separability criteria constructed from general symmetric informationally complete positive operator-valued measures (GSIC-POVMs) and symmetric informationally complete positive operator-valued measures (SIC-POVMs) are of great interest. Both types of POVMs offer feasible construction methods even in higher dimensions. Therefore, these measurements are suitable to obtain information on a variety of quantum states.

In this thesis, we investigate separability problems in selected families of states within the so-called magic simplex. Utilizing GSIC-POVMs and SIC-POVMs, we detect substantial areas of bound entangled states in all but one family. Furthermore, we verify separable states by assembling a family of separable states and applying entanglement-class-conserving symmetries within the magic simplex. As a result, we confirm that the detected areas of bound entangled states directly border regions of separable states in several investigated state families.

Zusammenfassung

In bipartiten Quantensystemen beschäftigt sich ein Separabilitätsproblem mit der Frage, ob ein Quantenzustand separabel oder verschränkt ist. Ein wichtiger Ansatz, um ein solches Problem zu lösen ist das Peres-Horodecki-Kriterium, welches in 2×2- und 2×3-Systemen eine notwendige und ausreichende Bedingung für Separabilität bildet. In höheren Dimensionen verkomplizieren sich Separabilitätsprobleme jedoch durch das Auftreten von gebundener Verschränkung. Dieser Begriff bezieht sich auf eine Art von Verschränkung, die nicht dazu verwendet werden kann, um mittels lokaler Operationen und klassischer Kommunikation maximal verschränkte Zustände zu destillieren.

Wenngleich das Peres-Horodecki-Kriterium gebundene Verschränkung nicht detektiert, existieren Kriterien, die Teilmengen dieser Zustände erkennen. In diesem Kontext sind notwendige Separabilitätskriterien konstruiert aus allgemeinen, symmetrischen, informationsvollständigen, positiven, operatorwertigen Maßen (GSIC-POVMs) und symmetrischen, informationsvollständigen, positiven, operatorwertigen Maßen (SIC-POVMs) von großem Interesse. Beide Arten von POVMs verfügen selbst in höheren Dimensionen über realisierbare Konstruktionsmethoden. Damit eignen sich diese Maße, um über eine Vielzahl verschiedener Quantensysteme Informationen zu gewinnen.

In dieser Arbeit untersuchen wir Separabilitätsprobleme ausgewählter Zustandsfamilien im sogenannten magischen Simplex. Unter Verwendung von GSIC-POVMs und SIC-POVMs detektieren wir substanzielle Gebiete gebundener Verschränkung in allen Zustandsfamilien außer einer. Des Weiteren verifizieren wir separable Zustände, indem wir eine Familie separabler Zustände konstruieren und verschränkungsklassenerhaltende Symmetrien innerhalb des magischen Simplexes anwenden. Infolgedessen bestätigen wir, dass die erkannten Gebiete gebundener Verschränkung in mehreren der untersuchten Zustandsfamilien direkt an Regionen separabler Zustände anschließen.

Acknowledgements

I would like to sincerely thank Mag. Dr. Beatrix Hiesmayr for her guidance throughout the facets of this project. Right from the beginning, her encouraging attitude and valuable advice helped me to familiarize myself with the topic and overcome all kinds of obstacles on my way. She invested a lot of time and effort in answering my questions and always showed patience when I needed further explanations to understand her message. I really enjoyed our conversations, which enhanced my abilities to formulate and pursue ideas. Her contributions were essential to the creation of this thesis.

I am also very grateful to my friends Michael Adam, Michael Becker, Marius Binder, and Felix Hubmann, who always lent an ear to my problems and offered me welcome distractions when I needed a break from my thesis.

Finally, I would like to thank my family, especially my parents Nicole and Johannes Hübner, who continuously supported me morally and financially over the course of two studies. Although my sudden turn to physics was unexpected at that time, they enabled me to follow my interests. Without their encouragement, I would not have made it this far.

Contents

1. Introduction

Quantum entanglement is a valuable resource used in numerous applications like quantum computing [1], quantum teleportation [2], and quantum cryptography [3]. It occurs whenever a quantum system formed by multiple particles is inseparable. Hence, this means that the particles cannot be described independently from each other.
Specifying whether a quantum state is separable or entangled constitutes the so-called separability problem. An important approach to tackle this problem is the Peres-Horodecki criterion [4], which states that all separable states must remain positive under partial transposition (PPT). In the case of 2×2 and 2×3 systems, every entangled state must violate the Peres-Horodecki criterion [5]. Consequently, the separability problem is fully solved in these low-dimensional systems. However, in higher dimensions there exist entangled states that do not violate the Peres-Horodecki criterion. It turns out that these states cannot be transformed into pure maximally entangled states by means of entanglement distillation [6] and therefore are referred to as bound entangled states. Conversely, their distillable counterparts are denoted as free entangled states. The task of detecting PPT entangled states is an NP-hard problem that has not been fully solved for arbitrary quantum mechanical systems. However, there exist separability criteria and entanglement witnesses that have shown their capability to detect bound entanglement in certain cases. In addition, they can also be useful for detecting subsets of entangled states that do not remain positive under partial transposition. This is convenient since the Peres-Horodecki criterion lacks a direct physical implementation.
An important entanglement witness suitable for bound entanglement detection consists of mutually unbiased bases (MUBs) [7, 8, 9]. In general, MUBs from the same set are known to be maximally incompatible measurements. This means that measuring an eigenstate of a MUB results in a completely random outcome, if we perform the measurement in a different MUB of the same set. Altogether, a complete set of MUBs contains $d+1$ bases, where d refers to the dimension. Unfortunately, such complete sets have only been successfully constructed in systems, which correspond to dimensions $d = p^n$ [10, 11], where p is a prime number and n is a positive integer. This circumstance also restricts the efficiency of the MUB witness.
In the domain of bound entanglement detection, our main interest relates to necessary separability criteria utilizing general symmetrically informationally complete positive operator-valued measures (GSIC-POVMs) [12, 13] and symmetrically informationally complete positive operator valued-measures (SIC-POVMs) [14, 15, 16]. The notion of informationally completeness refers to the fact that both branches of POVMs can be used to reconstruct quantum states from measurement probabilities. Overall, GSIC- and SIC-POVMs each consist of d^2 elements whose pairwise inner Hilbert-Schmidt products result in a fixed value. In more detail, the elements of SIC-POVMs are rank-one projection operators. Like MUBs, SIC operators from the same POVM are maximally incompatible. In contrast, GSIC-POVMs can be understood

as generalizations of SIC-POVMs that also admit operators with arbitrary rank. The big advantage of GSIC- and SIC-POVMs over MUBs is more feasible construction methods in higher dimensions. In fact, numerical SIC-POVMs have been constructed in all consecutive dimensions up to $d = 151$ [17], while exact-GSIC POVMs can be obtained in all finite dimensions [18]. This makes GSIC- and SIC-POVMs promising candidates for entanglement detection even in high-dimensional quantum systems.

In this thesis, we investigate separability problems of bipartite $d \times d$ systems within the so-called magic simplex [19]. Considering an orthonormal basis of d^2 pure maximally entangled states, the magic simplex comprises all convex combinations of the associated projection operators. The resulting geometric object, a simplex, offers a variety of symmetries. Certain structures in the phase space denoted as lines give rise to a kernel including only separable states. Furthermore, there exist symmetry transformations that conserve the entanglement class [20] of all states within the magic simplex. For $d \geq 3$, this includes separable, free entangled, and bound entangled states as well. Our main focus lies on selected state families corresponding to slices of the magic simplex with different properties with respect to bound entanglement. On one hand, we aim to use GSIC- and SIC-POVMs to detect free and bound entangled areas in these families. This also involves comparisons to results of the MUB witness, a generalized linear witness, and the quasi-pure concurrence [21] for reference. On the other hand, we intend to identify separable areas by reconstructing separable states and applying certain symmetries of the magic simplex. Ultimately, our goal is to employ these strategies to answer the question of whether the separability criteria using GSIC- and SIC-POVMs detect bound entanglement optimally in the examined state families.

Our thesis is structured as follows. The second chapter presents the mathematical formalism of quantum states as well as a method to compare two arbitrary states. The topic of entanglement in bipartite systems is then addressed in chapter three. This includes the definitions of separable and entangled states, entanglement detection via positive maps, the Peres-Horodecki criterion, the concept of bound entanglement, and a general description of entanglement witnesses. Throughout chapter four, MUBs and the MUB witness are properly introduced. Chapter five deals with GSIC- and SIC-POVMs. After laying out the basic concept of POVMs, both variants are defined, and constructing methods of GSIC- and SIC-POVMs are provided. Subsequently, a separability bound is presented that gives rise to separability criteria utilizing GSIC- and SIC-POVMs. The sixth chapter introduces the magic simplex, a kernel consisting only of separable states, entanglement-class-conserving symmetries, and the quasi-pure concurrence. Furthermore, the state families examined in the following two chapters are defined. Chapter seven contains the results of entanglement detection via GSIC- and SIC-POVMs, while comparing the obtained areas of (bound) entangled states with the results of other criteria eligible for entanglement detection. For 3×3 state families, also adapted separability criteria for incomplete GSIC- and SIC-POVMs are tested. In chapter eight, a separable 3×3 state family is constructed and utilized to detect separable states in the magic simplex. In this process, the separably constructed state family is expanded by using entanglement-class-conserving symmetries. The ninth chapter eventually summarizes the results of the two previous chapters and highlights the conclusions.

2. Quantum States

Quantum states are a basic tool to study the properties and behavior of quantum mechanical systems. In the beginning of this chapter we will present the mathematical formalism to describe such systems. This involves the distinction between pure and mixed states. Through the Bloc vector decomposition we will present a method to construct quantum states in dimensions $d \geq 2$. Therefore, we will also introduce Gell-Mann matrices and the Weyl operator basis, which both will play essential roles in the course of this thesis. At the end of this chapter, we will introduce the fidelity as a method to compare two arbitrary quantum states.

2.1. Pure and Mixed States

A quantum state is a mathematical object that contains all available information about a particular quantum mechanical system. In the simplest case, it can be represented by a normalized vector $|\psi\rangle$ that lives in a d-dimensional Hilbert space $\mathcal{H} = \mathbb{C}^d$. Thereby, $|\psi\rangle$ is called a state vector.
In the density matrix formalism a so-called pure state is constituted by taking the outer product of $|\psi\rangle$ with itself. Consequently, the density matrix ρ of a pure state is given by

$$\rho = |\psi\rangle \langle\psi| \,. \tag{2.1}$$

For pure states, we know precisely in which state our quantum mechanical system is. However, there is a class of quantum states in which we only have partial knowledge about the state of the system. Let us consider a set of state vectors $\{|\psi_i\rangle\}$, where $i = 1, 2, ..., n$. The density matrix of a so-called mixed state can be described by a convex mixture of pure states

$$\rho = \sum_{i=1}^{n} p_i \, |\psi_i\rangle \langle\psi_i| \,, \tag{2.2}$$

where $p_i \leq 1$ and $\sum_{i=1}^{n} p_i = 1$. Note that for $n = 1$ and $p_1 = 1$ equation (2.2) describes a pure state. Generally, any density matrix must satisfy the following conditions:

$$\begin{aligned} &Tr(\rho) = 1, \\ &\rho \geq 0, \\ &Tr(\rho^2) \leq Tr(\rho) = 1. \end{aligned} \tag{2.3}$$

The first line of equation (2.3) states that ρ has trace class 1. The second line requires the density matrix to be positive semidefinite. This condition is satisfied, if all eigenvalues of ρ are real and non-negative. In the course of our thesis, we will refer to this condition as the positivity criterion. The third line provides information about whether a state is pure or mixed. If $Tr(\rho^2) = 1$ the examined state is pure, else it is mixed.

2.2. Bloch Vector Decomposition

A core property of quantum states is that they can live in superpositions of multiple states. In order to illustrate this concept, let us consider $d = 2$. In this case, classical bits either take the values 0 or 1. However, the situation changes fundamentally for their quantum mechanical counterparts known as qubits. Any pure qubit state can be described by the general form

$$|\psi\rangle = cos\frac{\theta}{2}|0\rangle + e^{i\phi}sin\frac{\theta}{2}|1\rangle, \tag{2.4}$$

where $\theta \in [0, \pi]$ and $\phi \in [0, 2\pi)$. In Bloch's sphere [22, 23] the basis states $|0\rangle$ and $|1\rangle$ represent north and south pole, while θ and ϕ describe the polar and azimuthal angle. Equation (2.4) produces a continuum of pure qubit states that form the surface of Bloch's sphere. However, qubit states are generally not limited to the surface of this sphere. Using the density matrix formalism, the general expression of qubit states is given by

$$\rho = \frac{1}{2}(\mathbb{1}_2 + \vec{b} \cdot \vec{\sigma}), \tag{2.5}$$

where $\mathbb{1}_2$ is the identity matrix for $d = 2$, $\vec{b} \in \mathbb{R}^3$ with $|\vec{b}| \leq 1$, and $\vec{\sigma} = (\sigma_x, \sigma_y, \sigma_z)^T$ is a vector consisting of the Pauli matrices. The three-dimensional Bloch vector $\vec{b}$ describes pure qubit states for $|\vec{b}| = 1$ and mixed qubit states for $|\vec{b}| < 1$. In the former case $\vec{b}$ creates points on the surface of Bloch's sphere, while in the latter case $\vec{b}$ corresponds to points inside the sphere.
Let us now consider d-dimensional quantum states, also known as qudits. Equation (2.5) can be generalized for arbitrary $d \geq 2$. Any qudit state can be represented by the Bloch vector decomposition [24]

$$\rho = \frac{1}{d}\mathbb{1}_d + \vec{b} \cdot \vec{\Gamma}, \tag{2.6}$$

where $\vec{b} \in \mathbb{R}^{d^2-1}$, and $\vec{\Gamma} = (\Gamma_1, \Gamma_2, ..., \Gamma_{d^2-1})^T$ consists of $d \times d$ matrices $\{\Gamma_i\}$ that satisfy

$$\begin{aligned} &Tr(\Gamma_i) = 0, \\ &Tr(\Gamma_i^\dagger \Gamma_j) = N\delta_{i,j}, \quad N \in \mathbb{R}. \end{aligned} \tag{2.7}$$

The first line of equation (2.7) refers to traceless matrices, and the second line implies orthogonality under the Hilbert-Schmidt inner product. Both requirements are met by many sets of matrices. For example, convenient choices for $\{\Gamma_i\}$ are the generalized Gell-Mann matrices or certain subsets of Weyl matrices. Both families of matrices can be viewed as higher-dimensional extensions of Pauli matrices. The $(d^2 - 1)$-dimensional Bloch vector must satisfy

$$|\vec{b}| \leq \frac{\sqrt{d-1}}{Nd}. \tag{2.8}$$

Thereby, pure qudit states correspond to Bloch vectors with maximal length, while mixed states result in $|\vec{b}| < \frac{\sqrt{d-1}}{Nd}$. For $d > 2$, there exist Bloch vectors for which the result of equation (2.6) violates the positivity criterion. In these cases, $\vec{b}$ does not constitute qudit states, and the corresponding points must be excluded from Bloch's hypersphere. Therefore, it is said that Bloch's hypersphere has holes.

2.3. Generalized Gell-Mann Matrices

The generalized Gell-Mann matrices [25, 24] constitute the generators of the special unitary group $SU(n)$, which for $n = d$ consists of all unitary $d \times d$ matrices that have a determinant equal to 1. However, the generalized Gell-Mann matrices themselves are not unitary but Hermitian. They form sets of $d^2 - 1$ matrices given by

$$\begin{aligned}
\Lambda_{j,k} &= |j\rangle\langle k| + |k\rangle\langle j|, \quad 0 \leq j < k \leq d-1, \\
\Lambda_{j,k} &= i(|j\rangle\langle k| - |k\rangle\langle j|), \quad 0 \leq k < j \leq d-1, \\
\Lambda_{j,j} &= \sqrt{\tfrac{2}{(j+1)(j+2)}}\left(\sum_{l=0}^{j} |l\rangle\langle l| - (j+1)\,|j+1\rangle\langle j+1|\right), \quad 0 \leq j \leq d-2.
\end{aligned} \tag{2.9}$$

Thereby, the $\{\Lambda_{j,k}\}$ correspond to $\frac{d(d-1)}{2}$ symmetric matrices for $j < k$, $\frac{d(d-1)}{2}$ asymmetric matrices for $j > k$, and $d-1$ diagonal matrices for $j = k$. The definitions in equation (2.9) imply that all generalized Gell-Mann matrices are traceless and satisfy

$$Tr(\Lambda_{j,k}^{\dagger}\Lambda_{l,m}) = 2\,\delta_{j,l}\delta_{k,m}. \tag{2.10}$$

Therefore, they also obey equation (2.7) and can be utilized for the Bloch vector decompositions in $d \geq 2$. Furthermore, expanding the set of $d^2 - 1$ generalized Gell-Mann matrices by the d-dimensional identity matrix $\mathbb{1}_d$ generates a basis of the Hilbert-Schmidt space.
For $d = 3$, equation (2.9) results in a set of 8 matrices denoted as Gell-Mann matrices. They are given by

$$\begin{aligned}
&\Lambda_{0,0} = \begin{pmatrix} 1 & 0 & 0 \\ 0 & -1 & 0 \\ 0 & 0 & 0 \end{pmatrix}, \quad \Lambda_{0,1} = \begin{pmatrix} 0 & 1 & 0 \\ 1 & 0 & 0 \\ 0 & 0 & 0 \end{pmatrix}, \quad \Lambda_{0,2} = \begin{pmatrix} 0 & 0 & 1 \\ 0 & 0 & 0 \\ 1 & 0 & 0 \end{pmatrix}, \\
&\Lambda_{1,0} = \begin{pmatrix} 0 & -i & 0 \\ i & 0 & 0 \\ 0 & 0 & 0 \end{pmatrix}, \quad \Lambda_{1,1} = \frac{1}{\sqrt{3}}\begin{pmatrix} 1 & 0 & 0 \\ 0 & 1 & 0 \\ 0 & 0 & -2 \end{pmatrix}, \quad \Lambda_{1,2} = \begin{pmatrix} 0 & 0 & 0 \\ 0 & 0 & 1 \\ 0 & 1 & 0 \end{pmatrix},
\end{aligned} \tag{2.11}$$

$$\Lambda_{2,0} = \begin{pmatrix} 0 & 0 & -i \\ 0 & 0 & 0 \\ i & 0 & 0 \end{pmatrix}, \quad \Lambda_{2,1} = \begin{pmatrix} 0 & 0 & 0 \\ 0 & 0 & -i \\ 0 & i & 0 \end{pmatrix}.$$

2.4. Weyl Matrices

The Weyl operator basis [26, 24] consists of d^2 operators denoted as Weyl matrices. Contrary to Gell-Mann matrices, the Weyl matrices are generally not Hermitian but unitary. They are given by

$$W_{k,l} = \sum_{j=0}^{d-1} \omega^{jk} \left|j\right\rangle \left\langle (j+l)_{mod(d)}\right|, \quad j,k = 0,1,...,d-1, \tag{2.12}$$

where $\omega = e^{\frac{2\pi i}{d}}$ describes the d-th root of unity. From equation (2.12) we conclude that $W_{0,0} = \mathbb{1}_d$ has a non-vanishing trace, while all other $W_{k,l}$ are traceless. Furthermore, Weyl matrices satisfy the orthogonality condition

$$Tr(W^{\dagger}_{j,k} W_{l,m}) = d\, \delta_{j,l} \delta_{k,m}. \tag{2.13}$$

Consequently, the subset of $d^2 - 1$ traceless Weyl matrices can be utilized for Bloch vector decompositions in $d \geq 2$. In general, the Weyl operator basis forms an orthonormal basis of the d-dimensional Hilbert-Schmidt space. Weyl matrices also play a crucial role in the generation of bases formed by d^2 maximally entangled qudit states. We will further elaborate on this application in the sixth chapter.
In the case of $d = 3$, $\omega = e^{\frac{2\pi i}{3}}$ and equation (2.12) results in a set of 9 Weyl matrices that are given by

$$\begin{aligned} W_{0,0} &= \begin{pmatrix} 1 & 0 & 0 \\ 0 & 1 & 0 \\ 0 & 0 & 1 \end{pmatrix} = \mathbb{1}_3, \quad W_{0,1} = \begin{pmatrix} 0 & 1 & 0 \\ 0 & 0 & 1 \\ 1 & 0 & 0 \end{pmatrix}, \quad W_{0,2} = \begin{pmatrix} 0 & 0 & 1 \\ 1 & 0 & 0 \\ 0 & 1 & 0 \end{pmatrix}, \\ W_{1,0} &= \begin{pmatrix} 1 & 0 & 0 \\ 0 & \omega & 0 \\ 0 & 0 & \omega^* \end{pmatrix}, \quad W_{1,1} = \begin{pmatrix} 0 & 1 & 0 \\ 0 & 0 & \omega \\ \omega^* & 0 & 0 \end{pmatrix}, \quad W_{1,2} = \begin{pmatrix} 0 & 0 & 1 \\ \omega & 0 & 0 \\ 0 & \omega^* & 0 \end{pmatrix}, \\ W_{2,0} &= \begin{pmatrix} 1 & 0 & 0 \\ 0 & \omega^* & 0 \\ 0 & 0 & \omega \end{pmatrix}, \quad W_{2,1} = \begin{pmatrix} 0 & 1 & 0 \\ 0 & 0 & \omega^* \\ \omega & 0 & 0 \end{pmatrix}, \quad W_{2,2} = \begin{pmatrix} 0 & 0 & 1 \\ \omega^* & 0 & 0 \\ 0 & \omega & 0 \end{pmatrix}. \end{aligned} \tag{2.14}$$

2.5. Fidelity

Comparing different quantum states with each other is a fundamental task in quantum information science. As an example, we may want to transmit a quantum state via a quantum

communication channel. Then, the quality of transmission is determined by the closeness between the input and the output state. This can be measured by the fidelity [27].
Consider two mixed states $\rho_1 = \sum_i \alpha_i \left|\alpha_i\right\rangle \left\langle\alpha_i\right|$ and $\rho_2 = \sum_i \beta_i \left|\beta_i\right\rangle \left\langle\beta_i\right|$ with $\alpha_i, \beta_i \geq 0$ and $\sum_i \alpha_i = \sum_i \beta_i = 1$. Assume that both states are displayed in their spectral decomposition. In this representation, the coefficients α_i, β_i denote the eigenvalues of the respective state and the vectors $\left|\alpha_i\right\rangle, \left|\beta_i\right\rangle \in \mathcal{H}_A$ can be identified with the corresponding eigenvectors. Then, the purifications of our mixed states can be written in the form [28]

$$\begin{aligned} \left|\phi_1\right\rangle &= \sum_i \alpha_i \left|\alpha_i\right\rangle \otimes \left|f_i\right\rangle , \\ \left|\phi_2\right\rangle &= \sum_i \beta_i \left|\beta_i\right\rangle \otimes \left|g_i\right\rangle , \end{aligned} \tag{2.15}$$

where $\{\left|f_i\right\rangle \ , \{\left|g_i\right\rangle\} \in \mathcal{H}_B$ denote freely selectable orthonormal bases and $\left|\phi_1\right\rangle, \left|\phi_2\right\rangle$ are pure states in $\mathcal{H}_A \otimes \mathcal{H}_B$. Utilizing these purifications, the fidelity of two mixed states can be formulated in terms of [27]

$$F(\rho_1, \rho_2) = \max \left| \left\langle \phi_1 | \phi_2 \right\rangle \right|^2. \tag{2.16}$$

From this result, it follows that $F(\rho_1, \rho_2) = F(\rho_2, \rho_1)$, $F(\rho_1, \rho_2) \in [0, 1]$, and that the upper bound of this interval is saturated if $\rho_1 = \rho_2$. As a rule, the closer two states are, the greater is the resulting value of the fidelity. It was shown [27] that the fidelity of two mixed states, as defined in equation (2.16), is equivalent to [29]

$$F(\rho_1, \rho_2) = (Tr\sqrt{\sqrt{\rho_1}\rho_2\sqrt{\rho_1}})^2. \tag{2.17}$$

3. Entanglement in Bipartite Systems

Entanglement is a curious phenomenon that is observed in certain quantum systems shared by multiple parties. In this thesis we will solely discuss the bipartite case. We will start this chapter with the basic definitions of separability and entanglement and then present how positive maps theory gives rise to the Peres-Horodecki criterion. After that, we will explain the link between entanglement distillation and bound entanglement. Therefore, we will also introduce the entanglement witness as a possible method to detect such bound entangled states.

3.1. Separable and Entangled States

Let us consider a composite system consisting of two spatially separated parties held by Alice and Bob. Alice's subsystem lives in the Hilbert space $\mathcal{H}_A$, while Bob's subsystem can be identified with $\mathcal{H}_B$. Together they form a bipartite quantum system in the Hilbert space $\mathcal{H}_A \otimes \mathcal{H}_B$ with dimension $d_A \times d_B$.
Suppose a bipartite pure state $|\psi\rangle_{AB}$. Such a state is defined as separable if it can be written as the tensor product

$$|\psi\rangle_{AB} = |\psi\rangle_A \otimes |\psi\rangle_B \,, \tag{3.1}$$

where $|\psi\rangle_A$ and $|\psi\rangle_B$ are the pure states assigned to Alice's and Bob's party. Note that separable pure states are also referred to as product states. However, if $|\psi\rangle_{AB}$ cannot be written in terms of equation (3.1), it is entangled.
Now, let us consider a bipartite mixed state denoted by ρ_{AB}. This density matrix is defined as separable if it can be written as

$$\rho_{AB} = \sum_i p_i \, \rho_i^A \otimes \rho_i^B, \tag{3.2}$$

where ρ_i^A and ρ_i^B are the density matrices of Alice's and Bob's subsystem, $0 \leq p_i \leq 1$ and $\sum_i p_i = 1$. Again, if ρ_{AB} cannot be written in terms of equation (3.2), it is entangled.
Specifying whether a bipartite state is separable or entangled constitutes a separability problem. In the case of pure states, this problem can be solved by writing $|\psi\rangle_{AB}$ in terms of the Schmidt decomposition [23, 30]

$$|\psi\rangle_{AB} = \sum_{i=1}^{n} \sqrt{\lambda_i} \, |i_a\rangle_A \otimes |i_b\rangle_B \,, \tag{3.3}$$

where the Schmidt coefficients λ_i satisfy $0 \leq \lambda_i \leq 1$ and $\sum_i \lambda_i = 1$. Also, note that $n = min\{d_A, d_B\}$ and the sets $\{|i_a\rangle_A\}$ and $\{|i_b\rangle_B\}$ form orthonormal bases in the subspaces of Alice

and Bob. Generally, $|\psi\rangle_{AB}$ is separable if there exists only one non-zero Schmidt coefficient and is entangled if there are multiple non-vanishing Schmidt coefficients. The notion of a maximally entangled state refers to the case, where $|\psi\rangle_{AB}$ has only non-vanishing Schmidt coefficients that have all the same value.
However, for mixed states there is no criterion that can always determine whether an arbitrary qudit state is separable or entangled. Instead, we make use of criteria that all separable states must satisfy. If a mixed state violates such a necessary separability criterion it must be entangled. In order to show that a mixed state is separable, we have to explicitly write it in terms of equation (3.2) or utilize that the set of all separable states is convex. Therefore, any convex combination of separable states is also confirmed to be separable. During this and the next three chapters, we will discuss several criteria that will enable us to solve the separability problem for certain mixed states.

3.2. Entanglement Detection via Positive Maps

Suppose a positive operator ρ and a linear map Λ act on the Hilbert space. Λ is denoted as a positive map, if

$$\Lambda(\rho) \geq 0, \quad \forall \rho \geq 0. \tag{3.4}$$

Furthermore, a positive map is called a completely positive if it also satisfies

$$(\Lambda \otimes \mathbb{1}_d)\rho \geq 0, \quad \forall \rho \geq 0, \tag{3.5}$$

where $\mathbb{1}_d$ is the identity operator of dimension d. From now on, consider Λ to be a positive but not completely positive map. Hence, Λ generally does not satisfy equation (3.5) for arbitrary positive operators. Also, assume that ρ represents the density matrix of a bipartite mixed state. If ρ is a separable state, equations (3.2) and (3.4) imply that

$$(\Lambda \otimes \mathbb{1}_d)\rho = (\Lambda \otimes \mathbb{1}_d)(\sum_i p_i\, \rho_i^A \otimes \rho_i^B) = \sum_i p_i\, \Lambda(\rho_i^A) \otimes \rho_i^B \geq 0. \tag{3.6}$$

Consequently, this inequality constitutes a necessary condition for bipartite separability. However, there may also exist entangled states that satisfy $(\Lambda \otimes \mathbb{1})\rho \geq 0$. Therefore, applying this separability condition, we cannot know whether ρ is separable, but conversely we can conclude that ρ must be an entangled state if [5]

$$(\Lambda \otimes \mathbb{1})\rho \ngeq 0. \tag{3.7}$$

Note that this statement also holds using the map $(\mathbb{1} \otimes \Lambda)$ instead. In summary, positive but not completely positive maps can be utilized to detect entanglement.

3.3. Peres-Horodecki Criterion

An example for a positive but not completely positive map is given by the transposition T. In its general form, the density matrix of a bipartite state can be written as

$$\rho = \sum_{i,j,k,l=0}^{d-1} \rho_{ij,kl} \left|i\right\rangle_A \left\langle j\right|_A \otimes \left|k\right\rangle_B \left\langle l\right|_B . \tag{3.8}$$

Applying the maps $(T \otimes \mathbb{1})$ and $(\mathbb{1} \otimes T)$ to our bipartite state results in

$$\begin{aligned} \rho^{T_A} &:= (T \otimes \mathbb{1})\rho = \sum_{i,j,k,l=0}^{d-1} \rho_{ij,kl} (\left|i\right\rangle_A \left\langle j\right|_A)^T \otimes \left|k\right\rangle_B \left\langle l\right|_B \\ &= \sum_{i,j,k,l=0}^{d-1} \rho_{ij,kl} \left|j\right\rangle_A \left\langle i\right|_A \otimes \left|k\right\rangle_B \left\langle l\right|_B , \\ \rho^{T_B} &:= (\mathbb{1} \otimes T)\rho = \sum_{i,j,k,l=0}^{d-1} \rho_{ij,kl} \left|i\right\rangle_A \left\langle j\right|_A \otimes (\left|k\right\rangle_B \left\langle l\right|_B)^T \\ &= \sum_{i,j,k,l=0}^{d-1} \rho_{ij,kl} \left|i\right\rangle_A \left\langle j\right|_A \otimes \left|l\right\rangle_B \left\langle k\right|_B . \end{aligned} \tag{3.9}$$

We can see that these maps each transpose only one subsystem while leaving the other invariant. Therefore, ρ^{T_A} is referred to as the partial transposition of Alice's party, and ρ^{T_B} is called the partial transposition of Bob's party. A state is denoted as positive under partial transposition (PPT) if its partial transposition remains positive semidefinite, which means that all eigenvalues remain non-negative. The Peres-Horodecki criterion [4] states that any separable bipartite state is PPT. Therefore, we conclude that a state must be entangled if its partial transposition has at least one negative eigenvalue. Generally, the Peres-Horodecki criterion is only a necessary condition for separability. This means that states which are positive under partial transposition can be separable but also entangled.
However, in 2×2 and 2×3 systems the situation changes fundamentally. In these bipartite systems, all positive maps Λ can be decomposed into [31, 32]

$$\Lambda = \Lambda_1^{CP} + \Lambda_2^{CP} T, \tag{3.10}$$

where $= \Lambda_1^{CP}$ and $= \Lambda_2^{CP}$ are completely positive maps. Applying the map $(\Lambda \otimes \mathbb{1})$ to the density matrix ρ results in

$$(\Lambda \otimes \mathbb{1})\rho = (\Lambda_1^{CP} \otimes \mathbb{1})\rho + (\Lambda_2^{CP} T \otimes \mathbb{1})\rho = (\Lambda_1^{CP} \otimes \mathbb{1})\rho + (\Lambda_2^{CP} \otimes \mathbb{1})\rho^{T_A}. \tag{3.11}$$

Consequently, ρ must be negative under partial transposition (NPT) to violate $(\Lambda \otimes \mathbb{1})\rho \geq 0$. This is also the case for $(\mathbb{1} \otimes \Lambda)\rho \geq 0$. It follows that in 2×2 and 2×3 systems any PPT state must be separable [5]. In these dimensions, the Peres-Horodecki criterion is not only a necessary but also a sufficient condition for separability.

3.4. Entanglement Distillation and Bound Entanglement

Decoherence effects and experimental imperfections limit our capability to prepare pure maximally entangled states. Suppose that we possess many copies of a mixed entangled state that does not sufficiently resemble a pure maximally entangled state. Then we can often utilize local operations and classical communications (LOCC) to distill (almost) pure maximally entangled states. In such entanglement distillation protocols [33] we usually start with many copies of our mixed entangled state. Thereby, each copy consists of a pair of particles that is shared between the parties Alice and Bob. During the entanglement distillation process the parties are allowed to perform local operations on their respective particles and communicate their results classically to the other party. Conditioned on the transmitted information, Alice and Bob can then decide to perform further operations on their particles. The process is considered successful if we were able to generate some (almost) pure maximally entangled states.

In general, all entangled states that can be used to distill maximally entangled states through LOCC are called distillable. In their paper M. Horodecki et al. [6] showed that any distillable state must be NPT. Furthermore, the authors constructed an entangled bipartite qutrit state that is PPT. Consequently, there exist entangled states that are not distillable. This type of entanglement is referred to as bound entanglement, whereas distillable entanglement is denoted as free entanglement.

A goal of this thesis is to detect bound entanglement in various bipartite qudit systems with $d := d_A = d_B \geq 3$. We will achieve this by first checking whether the state in question is PPT. If this is the case, we will apply entanglement witnesses or necessary separability criteria to determine whether the PPT state is also entangled and, therefore, classifiable as bound entangled.

3.5. Entanglement Witness

The definition of separable states from equation (3.2) implies that the set of all separable states Ω_{sep} is convex and compact. Suppose a state $\rho_{ent} \notin \Omega_{sep}$. From the Hahn-Banach theorem [34, 35] follows that there must be a hyper-plane separating those two objects. This fact gives rise to an observable that enables us to detect specific entangled states. Let us consider a Hermitian operator $\mathcal{W}$. We call this operator an entanglement witness [36] if

$$\begin{aligned} &Tr(\mathcal{W}\rho) \geq 0, \quad \forall \rho \in \Omega_{sep} \\ &Tr(\mathcal{W}\rho_{ent}) < 0, \end{aligned} \tag{3.12}$$

where the first line of equation (3.12) must be satisfied for all separable states, and the second line must hold for at least one entangled state ρ_{ent}, which implies that $\mathcal{W}$ has at the minimum one negative eigenvalue. Consequently, all states ρ resulting in $Tr(\mathcal{W}\rho) < 0$ are confirmed to be entangled.

In practice, we rank different entanglement witnesses by comparing the sets of detected entangled states. Let us consider three entanglement witnesses $\mathcal{W}_1$, $\mathcal{W}_2$, and $\mathcal{W}_{opt}$. $\mathcal{W}_2$ is said to be finer than $\mathcal{W}_1$, if detects all entangled states obtained by $\mathcal{W}_1$ plus some additional entangled states. The optimal entanglement witness $\mathcal{W}_{opt}$ [37] refers to the case, where no finer entanglement witness exists. This means that there must be at least one separable state such that

$$Tr(\mathcal{W}_{opt}\rho) = 0, \quad \rho \in \Omega_{sep}. \tag{3.13}$$

Geometrically, the detection boundary $Tr(\mathcal{W}_{opt}\rho) = 0$ can be interpreted as a tangent plane to Ω_{sep}, as shown in figure 3.1.

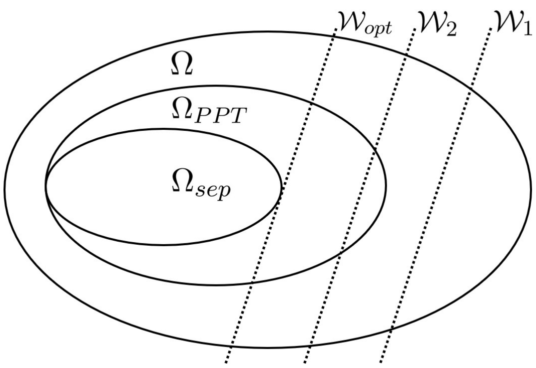

Figure 3.1.: This illustration contains the sets of all states Ω as well as its subsets Ω_{PPT} and Ω_{sep}. The detection boundaries of the entanglement witnesses $\mathcal{W}_1$, $\mathcal{W}_2$, and $\mathcal{W}_{opt}$ are marked by dotted lines.

Another useful way to classify entanglement witnesses is to determine whether they are decomposable. In our bipartite case, any decomposable $\mathcal{W}$ can be written in the form [37]

$$\mathcal{W} = aP + (1-a)Q^{T_A} \quad \text{or} \quad \mathcal{W} = aP + (1-a)Q^{T_B}, \tag{3.14}$$

where $a \in [0, 1]$ and $P, Q \geq 0$. Decomposable witnesses cannot detect PPT entangled states since

$$Tr[(aP + (1-a)Q^{T_A})\rho] = aTr(P\rho) + (1-a)Tr(Q\rho^{T_A}) \geq 0 \quad \forall \rho \in \Omega_{PPT}, \tag{3.15}$$

where Ω_{PPT} denotes the set of all PPT states. Therefore, we must utilize non-decomposable witnesses to detect bound entanglement. Concerning the witnesses shown in figure 3.1 this indicates that $\mathcal{W}_{opt}$ and $\mathcal{W}_2$ must be non-decomposable, while $\mathcal{W}_1$ can also be decomposable.

4. MUBs

A very effective entanglement witness, which even detects some bound entangled states, can be constructed using mutually unbiased bases (MUBs). In the beginning of this chapter, we will discuss the concept of complementarity and provide a proper definition of MUBs. Following that we give an overview about how generalized Pauli operators can be utilized for the construction of MUBs. In the end of this chapter, we will present a separability bound involving MUBs that gives rise to the so-called MUB witness.

4.1. Definition of MUBs

From Heisenberg's uncertainty principle, it is well known that we cannot gain full information about both the position and momentum of a quantum system. In consequence, position and momentum are said to be complementary. In principle, the concept of complementarity [38, 39] refers to any pair of observables whose measurement results cannot both be predicted with certainty. This corresponds to the observables having different eigenbases. Let $\{|i_a\rangle\}$ and $\{|j_b\rangle\}$ be the eigenbases assigned to the observables a and b. The complementarity of two observables reaches its most extreme form if the overlap $|\langle i_a|j_b\rangle|$ is equal $\forall i, j$. In this case, measuring an eigenstate of a in the eigenbasis of b and vice versa results in completely random outcomes. Accordingly, such observables are said to be maximally incompatible.
For example, this concept applies to Mutually unbiased bases [7]. Suppose k orthonormal bases $\mathcal{B}_k = \{|i_k\rangle\} = \{|0_k\rangle, |1_k\rangle, \ldots, |(d-1)_k\rangle\}$ that live in d-dimensional Hilbert space $\mathcal{H}$. Such bases are referred to as mutually unbiased if

$$|\langle i_k|j_{k'}\rangle|^2 = \delta_{k,k'}\,\delta_{i,j} + (1-\delta_{k,k'})\frac{1}{d}, \tag{4.1}$$

where the vectors of each $\mathcal{B}_k$ satisfy the completeness relation $\sum_{i=0}^{d-1} |i_k\rangle\langle i_k| = \mathbb{1}$. A set consisting of $d+1$ MUBs is called complete. This maximal number of mutually unbiased bases can be found in any finite $d = p^n$ [10, 11], where p is a prime number and $n \in \mathbb{N}_{>0}$. However, in other dimensions it is not even clear whether complete sets of MUBs do exist. The lowest dimension for which a complete set of mutually unbiased bases has not been found is $d = 6$.

4.2. Construction of MUBs

The task of constructing complete sets MUBs can be achieved in many ways. Here, we will present the methods involving generalized Pauli matrices as introduced by S. Bandyopadhyay et al. [40].

The original Pauli matrices form a set of three Hermitian and unitary 2×2 matrices σ_x, σ_y, and σ_z. By calculating their normalized eigenvectors, we can find a complete set of MUBs for $d = 2$. As we discussed in the second chapter, the Hermitian Gell-Mann matrices and unitary Weyl matrices can be seen as higher-dimensional extensions of the Pauli matrices. In this case, we will utilize the latter. Let us define the unitary operators X and Z as d-dimensional generalizations of the Pauli operators σ_x and σ_z, if they satisfy [41]

$$\begin{aligned} X_d \left|j\right\rangle &= \left|(j+1)_{mod(d)}\right\rangle , \\ Z_d \left|j\right\rangle &= \omega^j \left|j\right\rangle , \end{aligned} \tag{4.2}$$

where $\omega = e^{\frac{2\pi i}{d}}$. In any $d \geq 2$ there are two Weyl matrices that meet these requirements such that we can set $X_d = W_{0,(d-1)}$ and $Z_d = W_{1,0}$. Consequently, our generalized Pauli operators can be written in terms of

$$\begin{aligned} X_d &= \sum_{j=0}^{d-1} \left|(j+1)_{mod(d)}\right\rangle \left\langle j\right| , \\ Z_d &= \sum_{j=0}^{d-1} \omega^j \left|j\right\rangle \left\langle j\right| , \end{aligned} \tag{4.3}$$

where X_d and Z_d satisfy the commutation relation $Z_d X_d = \omega X_d Z_d$. This is important since J. Schwinger [7] used unitary operators that obey this relation to introduce MUBs. It turns out that the eigenvectors of the operators X_d and Z_d are mutually unbiased. Furthermore, in $d = p$ the eigenvectors of

$$\{Z_p, X_p, X_p Z_p, X_p (Z_p)^2, \ldots, X_p (Z_p)^{d-1}\} \tag{4.4}$$

form complete sets MUBs. For $d = 3$ this method results in

$$\begin{aligned} \mathcal{B}_1 &= \left\{ \begin{pmatrix} 1 \\ 0 \\ 0 \end{pmatrix}, \begin{pmatrix} 0 \\ 1 \\ 0 \end{pmatrix}, \begin{pmatrix} 0 \\ 0 \\ 1 \end{pmatrix} \right\}, \\ \mathcal{B}_2 &= \left\{ \frac{1}{\sqrt{3}} \begin{pmatrix} 1 \\ 1 \\ 1 \end{pmatrix}, \frac{1}{\sqrt{3}} \begin{pmatrix} 1 \\ \omega \\ \omega^* \end{pmatrix}, \frac{1}{\sqrt{3}} \begin{pmatrix} 1 \\ \omega^* \\ \omega \end{pmatrix} \right\}, \\ \mathcal{B}_3 &= \left\{ \frac{1}{\sqrt{3}} \begin{pmatrix} 1 \\ \omega \\ \omega \end{pmatrix}, \frac{1}{\sqrt{3}} \begin{pmatrix} 1 \\ \omega^* \\ 1 \end{pmatrix}, \frac{1}{\sqrt{3}} \begin{pmatrix} 1 \\ 1 \\ \omega^* \end{pmatrix} \right\}, \end{aligned} \tag{4.5}$$

$$\mathcal{B}_4 = \left\{ \frac{1}{\sqrt{3}} \begin{pmatrix} 1 \\ \omega^* \\ \omega^* \end{pmatrix}, \frac{1}{\sqrt{3}} \begin{pmatrix} 1 \\ 1 \\ \omega \end{pmatrix}, \frac{1}{\sqrt{3}} \begin{pmatrix} 1 \\ \omega \\ 1 \end{pmatrix} \right\}.$$

In $d = p^n$ we must adapt our approach to construct $d+1$ mutually unbiased bases. Consider the generalized Pauli operators X_p, Z_p, and the Pauli products $X_p^i Z_p^j$ with $0 \leq i, j \leq p-1$. By calculating tensor products composed of these elements, we eventually find $d+1$ sets C_i each consisting of d pairwise commuting $d \times d$ matrices. All C_i must contain the identity matrix $\mathbb{1}_d$ and satisfy $C_i \cap C_j = \{\mathbb{1}_d\}$ for $i \neq j$. In each C_i the pairwise commuting matrices share a basis of common eigenvectors. Altogether, the eigenbases obtained from

$$\{C_0, C_1, \ldots, C_{d-1}\}. \tag{4.6}$$

form a complete set of MUBs.

4.3. MUB Entanglement Witness

Because of their intriguing properties, MUBs can be used to detect quantum entanglement. The corresponding criterion was introduced by Spengler et al. [8].
Suppose a bipartite quantum state composed of two d-dimensional subsystems held by Alice and Bob. Note that Alice has the observable a and Bob the observable b, which are linked to the orthonormal bases $\{|i_a\rangle\}$ and $\{|i_b\rangle\}$. If both parties carry out measurements on their respective subsystem, each of them can obtain d possible results $\{0, 1, \ldots, d-1\}$. The joint probability $P_{a,b}(i,j)$ that Alice receives the result i, while Bob obtains the outcome j is given by

$$P_{a,b}(i,j) = Tr(|i_a\rangle \langle i_a| \otimes |j_b\rangle \langle j_b| \rho). \tag{4.7}$$

Using this quantity, we can introduce a correlation function $C_{a,b}$ that allows us to determine how well we can predict the outcome of one observable by measuring the other. This so-called mutual predictability is given by

$$C_{a,b} = \sum_{i=0}^{d-1} P_{a,b}(i,i) = \sum_{i=0}^{d-1} Tr(|i_a\rangle \langle i_a| \otimes |i_b\rangle \langle i_b| \rho), \tag{4.8}$$

where the upper bound $C_{a,b} = 1$ corresponds to fully correlated observables, and the lower bound $C_{a,b} = \frac{1}{d}$ indicates completely uncorrelated observables.
In order to utilize the mutual predictability for entanglement detection, Alice and Bob each must carry out their measurements in at least two bases. This becomes apparent when considering the general forms of a pure entangled state $|\psi\rangle = \sum_{i=0}^{d-1} \sqrt{\lambda_i} |i_a\rangle \otimes |i_b\rangle$ and a separable state $\rho = \sum_{i=0}^{d-1} \lambda_i |i_a\rangle \langle i_a| \otimes |i_b\rangle \langle i_b|$, where $0 \leq \lambda_i \leq 1$ and $\sum \lambda_i = 1$. If Alice performs her measurements in the basis $\{|i_a\rangle\}$ and Bob carries out his measurements in $\{|i_b\rangle\}$,

the correlation functions of both states result in $C_{a,b} = 1$. However, the situation changes if we operate with two mutually unbiased bases $\{|i_1\rangle\}$ and $\{|i_2\rangle\}$. Suppose the separable product state $|\psi_{pr}\rangle = |0_1\rangle \otimes |0_1\rangle = |0_1, 0_1\rangle$ and let Alice and Bob both carry out their measurements in the basis $\{|i_1\rangle\}$. Then the mutual predictability again results in $C_{1,1} = 1$. Now, let them both perform their respective measurements in the basis $\{|i_2\rangle\}$. From the definition of mutually unbiased bases follows that

$$\begin{aligned} P_{2,2}(i,i) &= Tr(|i_2\rangle\langle i_2| \otimes |i_2\rangle\langle i_2|\ |0_1,0_1\rangle\langle 0_1,0_1|) \\ &= \langle i_2,i_2|0_1,0_1\rangle\langle 0_1,0_1|i_2,i_2\rangle = |\langle i_2|0_1\rangle|^4 = \frac{1}{d^2} \end{aligned} \tag{4.9}$$

and subsequently $C_{2,2} = \frac{1}{d}$. In this case, the sum of the correlation functions results in $I_2 = \sum_{k=1}^{2} C_{k,k} = 1 + \frac{1}{d}$. For m mutually unbiased bases it can be shown [8] that the upper bound for all separable states ρ_{sep} is given by

$$I_m = \sum_{k=1}^{m} C_{k,k} = \sum_{k=1}^{m}\sum_{i=0}^{d-1} Tr(|i_k\rangle\langle i_k| \otimes |i_k\rangle\langle i_k|\,\rho_{sep}) \leq 1 + \frac{m-1}{d}. \tag{4.10}$$

Regarding a complete set of MUBs this corresponds to $I_{d+1} \leq 2$. Note that there also exist lower bounds [42], which can even depend on the chosen set of MUBs. However, throughout our thesis we will only utilize the upper bound for entanglement detection. To achieve this, let us consider the quantity

$$\mathcal{W}_{MUB}(m) = (1 + \frac{m-1}{d})\mathbb{1}_{d^2} - (\sum_{k=1}^{m}\sum_{i=0}^{d-1} |i_k\rangle\langle i_k| \otimes |i_k\rangle\langle i_k|). \tag{4.11}$$

From equation (4.10) it follows that

$$\langle \mathcal{W}_{MUB}(m)\rangle_\rho = Tr(\mathcal{W}_{MUB}\rho) \geq 0, \quad \forall \rho \in \Omega_{sep}. \tag{4.12}$$

We can conclude that $\mathcal{W}_{MUB}(m)$ constitutes an entanglement witness, if it has at least one negative eigenvalue. As an example, $\mathcal{W}_{MUB}(d+1)$ does not meet this condition, but its partial transposition $\mathcal{W}_{MUB}^{T_B}(d+1)$ gives rise to a decomposable entanglement witness [43]. Furthermore, applying certain combinations of Weyl operators to the MUBs of Bob's subsystem enables the witness to detect bound entanglement [9], thus making it non-decomposable. Overall, these changes correspond to rearrangements in the order of Bob's mutually unbiased bases. Taking the mentioned adaptations into account, we substitute the mutual detectability by the correlation function

$$\tilde{C}_{k,k}(p,q) = \sum_{i=0}^{d-1} Tr(|i_k\rangle\langle i_k| \otimes (W_{p,q}|i_k\rangle)^*(\langle i_k| W_{p,q}^\dagger)^*\rho). \tag{4.13}$$

In this case, it must be checked whether the resulting MUB witness $\tilde{\mathcal{W}}_{MUB}(m)$ still satisfies $\langle \tilde{\mathcal{W}}_{MUB}(m) \rangle_\rho \geq 0$ for all separable states. Therefore, we minimize the expression $Tr(\tilde{\mathcal{W}}_{MUB}(m)\rho)$, where $\rho = (U \otimes U) |0,0\rangle \langle 0,0| (U^\dagger \otimes U^\dagger)$ covers the convex hull of Ω_{sep}. The corresponding unitary matrix U can be constructed through composite parameterization of unitary groups [44, 45] using the Wolfram Mathematica package "Composite parameterization and Haar measure for unitary groups" [46]. For some combinations of Weyl operators, the separability bound may be slightly adjusted.

As we mentioned in the first section of this chapter, there are dimensions in which we cannot construct complete sets of MUBs. However, the MUB witness $\tilde{\mathcal{W}}_{MUB}(d+1)$ itself can be set up for any bipartite system of dimension $d \times d$. The resulting generalized linear witness is given by [9]

$$\begin{aligned} \mathcal{W}_{lin,i} = &- \sum_{k=0}^{d-1} \sum_{n=1}^{d-1} |k,k\rangle \langle n,n| + \sum_{k=0}^{d-1} 2\, |k,k\rangle \langle k,k| + \\ &\sum_{k=0}^{d-1} \sum_{n=1}^{d-1} (1-\delta_{ni}) \left|(k-n)_{mod(d)}, k\right\rangle \left\langle (k-n)_{mod(d)}, k\right| \end{aligned} \tag{4.14}$$

where the parameter $i \in \{0, 1, \ldots, d-1\}$ has the same effect as applying the Weyl operator $W_{0,i}$ to the first MUB of Bob's system.

5. GSIC- & SIC-POVMs

Like MUBs, also GSIC- and SIC-POVMs can be utilized to detect entangled states. We will start this chapter by introducing the concept of POVMs and defining SIC-POVMs. Then, we will discuss GSIC-POVMs as a generalization of the latter. Following this, we will continue with an explicit construction method of GSIC-POVMs for all $d \geq 2$. In comparison, we will discuss a strategy to obtain SIC-POVMs from so-called fiducial vectors by exploiting the property of group covariance. At the end of this chapter, we will present a separability bound applicable to GSIC- and SIC-POVMs that is suitable for entanglement detection.

5.1. The Concept of POVMs

In their most general form, quantum measurements correspond to positive operator-valued measures (POVMs) [23]. Consider a d-dimensional Hilbert space $\mathcal{H}$. A set of Hermitian operators $\{E_m\}_{m=1}^n$ constitutes a POVM if all operators satisfy

$$\begin{aligned} &E_m \geq 0, \\ &\sum_{m=1}^{n} E_m = \mathbb{1}_d, \end{aligned} \tag{5.1}$$

where the the second line of equation (5.1) is referred to as the completeness relation. Let $p(m) = Tr(E_m\rho)$ be the probability of obtaining the result m when measuring the state ρ. Then the completeness relation ensures that all probabilities add up to one.

Generally, POVMs are called informationally complete [47], if we can utilize the obtained probabilities to reconstruct any quantum state from the measured observables. Since all density matrices satisfy the constraint $Tr(\rho) = 1$, we only need $d^2 - 1$ real parameters corresponding to $d^2 - 1$ linearly independent measurements to fully determine an arbitrary state. However, the normalization of the probabilities provided by the completeness relation renders the result of one $p(m)$ fully dependent on all other probabilities. Taking this into account, an informationally complete set of POVMs cannot contain less than d^2 elements.

5.2. Definition of GSIC- & SIC-POVMs

Consider a set of Hermitian rank-one operators $\{\Pi_i \geq 0\}_{i=1}^{d^2}$ acting on $\mathcal{H}$. It is denoted as a symmetrically informationally complete (SIC) POVM [14, 15], if all operators in this set satisfy

$$Tr(\Pi_i \Pi_j) = \frac{1}{d^2(d+1)}(1 + d\,\delta_{i,j}) \tag{5.2}$$

and the completeness relation $\sum_{i=1}^{d^2} \Pi_i = \mathbb{1}_d$. Likewise, we can write these rank-one operators in terms of

$$\begin{aligned} \Pi_i &= \frac{1}{d} \left| S_i \right\rangle \left\langle S_i \right|, \\ \left| \left\langle S_i | S_j \right\rangle \right|^2 &= \frac{1}{d+1}, \quad \forall i \neq j, \end{aligned} \tag{5.3}$$

where $|S_i\rangle$ is referred to as a SIC vector. The key property of SIC-POVMs is that pairs of SIC vectors always have the same inner product for $i \neq j$. This symmetrical quality of SIC-POVMs resembles MUBs, which in contrast have a different amount of overlap. However, both definitions correspond to quantum 2-designs [42].
As a result of Zauner's conjecture, there should be SIC-POVMs in all finite dimensions $d \geq 2$. For example, numerical solutions of SIC-POVMs have been obtained in all consecutive dimensions up to $d = 151$ and, furthermore, in selected higher dimensions [17]. However, we still do not know whether SIC-POVMs exist in arbitrary dimensions.
If we remove the condition that all operators must have rank one, this allows us to generalize the concept of SIC-POVMs. Let us now consider a set of Hermitian operators $\{P_i \geq 0\}_{i=1}^{d^2}$ with arbitrary rank acting on $\mathcal{H}$. This set is defined as a general symmetrically informationally complete (GSIC) POVM [12, 18] if its operators satisfy

$$\begin{aligned} Tr(P_i^2) &= a, \\ Tr(P_i P_j) &= \frac{1 - da}{d(d^2 - 1)}, \quad \forall i \neq j, \end{aligned} \tag{5.4}$$

and the completeness relation $\sum_{i=1}^{d^2} P_i = \mathbb{1}_d$. GSIC-POVMs are symmetric in the sense that pairs of GSIC operators always have the same Hilbert-Schmidt inner product for $i \neq j$. Generally, the parameter a can have any value in the interval $(\frac{1}{d^3}, \frac{1}{d^2}]$. If we set $a = \frac{1}{d^2}$ and only permit rank-one operators, then equation (5.4) describes ordinary SIC-POVMs. Furthermore, it turns out that the trace of each GSIC operator is solely dependent on the dimension. Using the defining properties of GSIC-POVMs, we obtain

$$Tr(P_i) = Tr(P_i \mathbb{1}_d) = \sum_{j=1}^{d^2} Tr(P_i P_j) = a + (d^2 - 1) \frac{1 - da}{d(d^2 - 1)} = \frac{1}{d}. \tag{5.5}$$

The great advantage of GSIC-POVMs over SIC-POVMs is that they can be obtained in all finite dimensions $d \geq 2$ [18].

5.3. Construction of GSIC-POVMs

A straightforward method to construct GSIC-POVMs in all $d \geq 2$ was introduced by A. Kalev and G. Gour [18]. To present their approach, we consider a set of Hermitian $d \times d$ matrices $\{G_\alpha\}_{\alpha=1}^{d^2-1}$ that satisfy

$$\begin{aligned} Tr(G_\alpha) &= 0, \\ Tr(G_\alpha G_\beta) &= \delta_{\alpha,\beta}. \end{aligned} \tag{5.6}$$

In this thesis, we will use the generalized Gell-Mann matrices as defined in equation (2.9) and multiply the normalization factor $\frac{1}{\sqrt{2}}$ to each matrix such that $\{G_1, G_2, \ldots, G_{d^2-1}\} := \{\frac{1}{\sqrt{2}}\Lambda_{0,0}, \frac{1}{\sqrt{2}}\Lambda_{0,1}, \ldots, \frac{1}{\sqrt{2}}\Lambda_{d,d-1}\}$. However, any other set of Hermitian $d \times d$ matrices that meet the conditions in equation (5.6) can as well be utilized for this purpose.
Furthermore, let us denote the sum of the proposed matrices by $G = \sum_{\alpha=1}^{d-1} G_\alpha$. Then, in any $d \geq 2$ a complete set of GSIC operators is given by

$$\begin{aligned} P_\alpha &= \frac{1}{d^2}\mathbb{1}_d + t[G - d(d+1)G_\alpha], \quad \alpha = 1, 2, ..., d^2 - 1, \\ P_{d^2} &= \frac{1}{d^2}\mathbb{1}_d + t(d+1)G, \end{aligned} \tag{5.7}$$

where the value of the nonzero parameter t must be chosen such that all resulting GSIC operators are positive semidefinite. Note that $t \neq 0$ ensures their linear independence. The construction of GSIC operators given in equation (5.7) also allows us to obtain a general expression for the parameter a, which was previously introduced in the definition of GSIC-POVMs. Therefore, we again consider the trace properties of the matrices G_i. From equation (5.6) it follows that $Tr(G) = 0$, $Tr(G^2) = d^2 - 1$, and $Tr(G_\alpha G) = 1$. Using these relations we obtain [18]

$$Tr(P_\alpha P_\beta) = \frac{1}{d^3} + t^2(d+1)^2(d^2\delta_{\alpha,\beta} - 1). \tag{5.8}$$

This corresponds to $Tr(P_\alpha^2) = \frac{1}{d^3} + t^2(d+1)^3(d-1)$ and $Tr(P_\alpha P_\beta) = \frac{1}{d^3} - t^2(d+1)^2$ for $\alpha \neq \beta$. Comparing these results with the definition of GSIC-POVMs leads to

$$a = \frac{1}{d^3} + t^2(d+1)^3(d-1). \tag{5.9}$$

In the case of $d = 3$, equation (5.7) results in the GSIC operators

$$P_1 = \begin{pmatrix} \left(\frac{1}{\sqrt{2}} - 6\sqrt{2} + \frac{1}{\sqrt{6}}\right)t + \frac{1}{9} & \frac{(1-i)t}{\sqrt{2}} & \frac{(1-i)t}{\sqrt{2}} \\ \frac{(1+i)t}{\sqrt{2}} & \left(-\frac{1}{\sqrt{2}} + 6\sqrt{2} + \frac{1}{\sqrt{6}}\right)t + \frac{1}{9} & \frac{(1-i)t}{\sqrt{2}} \\ \frac{(1+i)t}{\sqrt{2}} & \frac{(1+i)t}{\sqrt{2}} & \frac{1}{9} - \sqrt{\frac{2}{3}}t \end{pmatrix}, \tag{5.10}$$

$$P_2 = \begin{pmatrix} \left(\frac{1}{\sqrt{2}} + \frac{1}{\sqrt{6}}\right) t + \frac{1}{9} & \left(-6\sqrt{2} + \frac{1-i}{\sqrt{2}}\right) t & \frac{(1-i)t}{\sqrt{2}} \\ \left(-6\sqrt{2} + \frac{1+i}{\sqrt{2}}\right) t & \left(\frac{1}{\sqrt{6}} - \frac{1}{\sqrt{2}}\right) t + \frac{1}{9} & \frac{(1-i)t}{\sqrt{2}} \\ \frac{(1+i)t}{\sqrt{2}} & \frac{(1+i)t}{\sqrt{2}} & \frac{1}{9} - \sqrt{\frac{2}{3}} t \end{pmatrix},$$

$$P_3 = \begin{pmatrix} \left(\frac{1}{\sqrt{2}} + \frac{1}{\sqrt{6}}\right) t + \frac{1}{9} & \frac{(1-i)t}{\sqrt{2}} & \left(-6\sqrt{2} + \frac{1-i}{\sqrt{2}}\right) t \\ \frac{(1+i)t}{\sqrt{2}} & \left(\frac{1}{\sqrt{6}} - \frac{1}{\sqrt{2}}\right) t + \frac{1}{9} & \frac{(1-i)t}{\sqrt{2}} \\ \left(-6\sqrt{2} + \frac{1+i}{\sqrt{2}}\right) t & \frac{(1+i)t}{\sqrt{2}} & \frac{1}{9} - \sqrt{\frac{2}{3}} t \end{pmatrix},$$

$$P_4 = \begin{pmatrix} \left(\frac{1}{\sqrt{2}} + \frac{1}{\sqrt{6}}\right) t + \frac{1}{9} & \left(\frac{1-i}{\sqrt{2}} + 6i\sqrt{2}\right) t & \frac{(1-i)t}{\sqrt{2}} \\ \left(\frac{1+i}{\sqrt{2}} - 6i\sqrt{2}\right) t & \left(\frac{1}{\sqrt{6}} - \frac{1}{\sqrt{2}}\right) t + \frac{1}{9} & \frac{(1-i)t}{\sqrt{2}} \\ \frac{(1+i)t}{\sqrt{2}} & \frac{(1+i)t}{\sqrt{2}} & \frac{1}{9} - \sqrt{\frac{2}{3}} t \end{pmatrix},$$

$$P_5 = \begin{pmatrix} \left(\frac{1}{\sqrt{2}} + \frac{1}{\sqrt{6}} - 2\sqrt{6}\right) t + \frac{1}{9} & \frac{(1-i)t}{\sqrt{2}} & \frac{(1-i)t}{\sqrt{2}} \\ \frac{(1+i)t}{\sqrt{2}} & \left(-\frac{1}{\sqrt{2}} + \frac{1}{\sqrt{6}} - 2\sqrt{6}\right) t + \frac{1}{9} & \frac{(1-i)t}{\sqrt{2}} \\ \frac{(1+i)t}{\sqrt{2}} & \frac{(1+i)t}{\sqrt{2}} & \left(4\sqrt{6} - \sqrt{\frac{2}{3}}\right) t + \frac{1}{9} \end{pmatrix},$$

$$P_6 = \begin{pmatrix} \left(\frac{1}{\sqrt{2}} + \frac{1}{\sqrt{6}}\right) t + \frac{1}{9} & \frac{(1-i)t}{\sqrt{2}} & \frac{(1-i)t}{\sqrt{2}} \\ \frac{(1+i)t}{\sqrt{2}} & \left(\frac{1}{\sqrt{6}} - \frac{1}{\sqrt{2}}\right) t + \frac{1}{9} & \left(-6\sqrt{2} + \frac{1-i}{\sqrt{2}}\right) t \\ \frac{(1+i)t}{\sqrt{2}} & \left(-6\sqrt{2} + \frac{1+i}{\sqrt{2}}\right) t & \frac{1}{9} - \sqrt{\frac{2}{3}} t \end{pmatrix},$$

$$P_7 = \begin{pmatrix} \left(\frac{1}{\sqrt{2}} + \frac{1}{\sqrt{6}}\right) t + \frac{1}{9} & \frac{(1-i)t}{\sqrt{2}} & \left(\frac{1-i}{\sqrt{2}} + 6i\sqrt{2}\right) t \\ \frac{(1+i)t}{\sqrt{2}} & \left(\frac{1}{\sqrt{6}} - \frac{1}{\sqrt{2}}\right) t + \frac{1}{9} & \frac{(1-i)t}{\sqrt{2}} \\ \left(\frac{1+i}{\sqrt{2}} - 6i\sqrt{2}\right) t & \frac{(1+i)t}{\sqrt{2}} & \frac{1}{9} - \sqrt{\frac{2}{3}} t \end{pmatrix},$$

$$P_8 = \begin{pmatrix} \left(\frac{1}{\sqrt{2}} + \frac{1}{\sqrt{6}}\right) t + \frac{1}{9} & \frac{(1-i)t}{\sqrt{2}} & \frac{(1-i)t}{\sqrt{2}} \\ \frac{(1+i)t}{\sqrt{2}} & \left(\frac{1}{\sqrt{6}} - \frac{1}{\sqrt{2}}\right) t + \frac{1}{9} & \left(\frac{1-i}{\sqrt{2}} + 6i\sqrt{2}\right) t \\ \frac{(1+i)t}{\sqrt{2}} & \left(\frac{1+i}{\sqrt{2}} - 6i\sqrt{2}\right) t & \frac{1}{9} - \sqrt{\frac{2}{3}} t \end{pmatrix},$$

$$P_9 = \begin{pmatrix} 4\left(\frac{1}{\sqrt{2}} + \frac{1}{\sqrt{6}}\right) t + \frac{1}{9} & (2-2i)\sqrt{2}t & (2-2i)\sqrt{2}t \\ (2+2i)\sqrt{2}t & 4\left(\frac{1}{\sqrt{6}} - \frac{1}{\sqrt{2}}\right) t + \frac{1}{9} & (2-2i)\sqrt{2}t \\ (2+2i)\sqrt{2}t & (2+2i)\sqrt{2}t & \frac{1}{9} - 4\sqrt{\frac{2}{3}} t \end{pmatrix},$$

where the parameter t must lie in the interval $[-0.012, 0.012]\backslash\{0\}$.

5.4. Construction of SIC-POVMs

A fundamental feature of all SIC-POVMs constructed so far is that they possess the property of group covariance [17]. In general, a SIC-POVM Π is confirmed to be a group covariant if we can find a group G, whose unitary representation $\{U_g\}$ satisfies two conditions [48]:

- First, all elements U_g must leave this SIC-POVM unchanged. To illustrate this, consider the SIC vector $|s_j\rangle \in \Pi$. Then, it must hold that

$$U_g |s_j\rangle \in \Pi, \quad \forall U_g \in G. \tag{5.11}$$

- Second, there must be a U_g that transforms any SIC vector into another, i.e.

$$U_g |S_j\rangle = |S_k\rangle, \quad |S_j\rangle, |S_k\rangle \in \Pi. \tag{5.12}$$

These conditions give rise to a method that uses a so-called fiducial vector $|\psi_f\rangle$ to construct the SIC-POVM $\Pi = \{U_g |\psi_f\rangle\}$ under the action of the elements of a certain group. In this thesis, we utilize the discrete Weyl-Heisenberg group to construct our SIC-POVMs. Therefore, we consider its generators ω, X_d, and Z_d, which obey the Weyl commutation relation [49]

$$X_d^\alpha Z_d^\beta = \omega^{-\alpha\beta} Z_d^\beta X_d^\alpha, \tag{5.13}$$

where $\omega = e^{\frac{2\pi i}{d}}$. Note, that we already introduced the unitary operators X_d and Z_d in the fourth chapter as d-dimensional generalizations of the Pauli matrices, when we discussed the construction of MUBs. Their definition and explicit form can be found in equations (4.2) and (4.3). It turns out that all elements of the Weyl-Heisenberg group can be expressed by the displacement operators [17]

$$D_{\alpha,\beta} = (-\sqrt{\omega})^{\alpha\beta} X_d^\alpha Z_d^\beta. \tag{5.14}$$

Consequently, we obtain the SIC vectors of the general form

$$|S_{\alpha,\beta}\rangle = \sqrt{\omega}^{\alpha\beta} X_d^\alpha Z_d^\beta |\psi_f\rangle, \tag{5.15}$$

where we omitted the global phase $(-1)^{\alpha\beta}$ of the displacement operators, since it does not influence the resulting SIC operators. In the case of $d = 3$, a fiducial vector for the Weyl-Heisenberg group is given by

$$|\psi_f\rangle = \frac{1}{\sqrt{2}}(|1\rangle - |2\rangle). \tag{5.16}$$

Using the discussed construction method, we obtain the SIC vectors

$$
\begin{aligned}
|S_1\rangle &= \frac{1}{\sqrt{2}}\begin{pmatrix}0\\1\\-1\end{pmatrix}, \quad |S_2\rangle = \frac{1}{\sqrt{2}}\begin{pmatrix}0\\e^{\frac{2i\pi}{3}}\\-e^{-\frac{2i\pi}{3}}\end{pmatrix} \quad |S_3\rangle = \frac{1}{\sqrt{2}}\begin{pmatrix}0\\e^{-\frac{2i\pi}{3}}\\-e^{\frac{2i\pi}{3}}\end{pmatrix}, \\
|S_4\rangle &= \frac{1}{\sqrt{2}}\begin{pmatrix}-1\\0\\1\end{pmatrix}, \quad |S_5\rangle = \frac{1}{\sqrt{2}}\begin{pmatrix}-e^{-\frac{i\pi}{3}}\\0\\-1\end{pmatrix} \quad |S_6\rangle = \frac{1}{\sqrt{2}}\begin{pmatrix}-e^{-\frac{2i\pi}{3}}\\0\\1\end{pmatrix}, \\
|S_7\rangle &= \frac{1}{\sqrt{2}}\begin{pmatrix}1\\-1\\0\end{pmatrix}, \quad |S_8\rangle = \frac{1}{\sqrt{2}}\begin{pmatrix}e^{-\frac{2i\pi}{3}}\\-1\\0\end{pmatrix} \quad |S_9\rangle = \frac{1}{\sqrt{2}}\begin{pmatrix}e^{\frac{2i\pi}{3}}\\-1\\0\end{pmatrix}.
\end{aligned}
\tag{5.17}
$$

In order to ensure consistency with equation (5.3) we changed the numbering scheme from $\{S_{0,0}, S_{0,1}, \ldots, S_{2,2}\}$ to $\{S_1, S_2, \ldots, S_9\}$.

5.5. Entanglement Detection via GSIC- and SIC-POVMs

The properties of GSIC- and SIC-POVMs make them interesting objects with respect to entanglement detection. In this section, we present a powerful criterion derived for GSIC-POVMs, which can even be used to detect bound entangled states. It was introduced by L.-M. Lai et. al [13] as a generalization of the enhanced SIC criterion [16].

Suppose an arbitrary quantum state ρ. Using GSIC-POVMs, any density matrix can be written in terms of [18]

$$\rho = \frac{d(d^2-1)}{ad^3-1}\sum_{\alpha=1}^{d^2} p_\alpha P_\alpha - \frac{d(1-ad)}{ad^3-1}\mathbb{1}_d, \tag{5.18}$$

where $p_\alpha = Tr(P_\alpha \rho)$ denotes the probability of obtaining the result α. After multiplying equation (5.18) times ρ and taking the trace, we can use the resulting equation to obtain an expression for the sum of all squared probabilities with the upper bound

$$\sum_{\alpha=1}^{d^2} p_\alpha^2 = \frac{(ad^3-1)Tr(\rho^2) + d(1-ad)}{d(d^2-1)} \leq \frac{ad^2+1}{d(d+1)}, \tag{5.19}$$

which corresponds to pure states. From now on assume the case of a bipartite state composed of a d_A-dimensional subsystem held by Alice and a subsystem of dimension d_B held by Bob. Additionally, let each party have a suitable GSIC-POVM $\{P_i^A\}_{i=1}^{d_A^2}$ or $\{P_i^B\}_{i=1}^{d_B^2}$ assigned to them. If Alice and Bob perform measurements on their respective subsystems, we can define the correlation matrix

$$[\mathcal{P}_{ij}] = Tr(P_i^A \otimes P_j^B \rho), \tag{5.20}$$

which entries consist of the joint probability $\mathcal{P}_{ij}$ that Alice obtains the outcome i, while Bob receives the result j. Note that the trace norm of the correlation matrix is denoted by $\|\mathcal{P}\|_{Tr} = Tr(\sqrt{\mathcal{P}^\dagger \mathcal{P}})$.
Let us further narrow down the case to a pure separable state of the form $\rho = \rho_A \otimes \rho_B$. Then, equation (5.20) simplifies to $[\mathcal{P}_{ij}] = p_{A,i} p_{B,j}$ with the probabilities $p_{A,i} = Tr(P_i^A \rho_A)$ and $p_{B,j} = Tr(P_j^B \rho_B)$. In this case, the correlation matrix is given by

$$\mathcal{P} = \begin{pmatrix} p_{A,1} \\ \dots \\ p_{A,d_A^2} \end{pmatrix} (p_{B,1} \, \dots \, p_{B,d_B^2}) := \vec{p}_A \vec{p}_B^T, \tag{5.21}$$

where $\vec{p}_A$ and $\vec{p}_B$ are vectors consisting of the respective probabilities. Consequently, the trace norm of this correlation matrix results in

$$\begin{aligned} \|\mathcal{P}\|_{Tr} &= Tr\left(\sqrt{(\vec{p}_A \vec{p}_B^T)^T \vec{p}_A \vec{p}_B^T}\right) = Tr\left(\sqrt{\vec{p}_B \vec{p}_A^T \vec{p}_A \vec{p}_B^T}\right) \\ &= \sqrt{\sum_{i=1}^{d^2} p_{A,i}^2}\; Tr\left(\sqrt{\vec{p}_B \vec{p}_B^T}\right) = \sqrt{\sum_{i=1}^{d^2} p_{A,i}^2} \sqrt{\sum_{j=1}^{d^2} p_{B,j}^2} \\ &\leq \sqrt{\frac{a_A d_A^2 + 1}{d_A(d_A+1)}} \sqrt{\frac{a_B d_B^2 + 1}{d_B(d_B+1)}}, \end{aligned} \tag{5.22}$$

where we inserted the upper bound of equation (5.19). Since the convex hull of Ω_{sep} is formed by pure separable states, we can conclude that [13]

$$\|\mathcal{P}\|_{Tr} \leq \sqrt{\frac{a_A d_A^2 + 1}{d_A(d_A+1)}} \sqrt{\frac{a_B d_B^2 + 1}{d_B(d_B+1)}}, \quad \forall \rho \in \Omega_{sep}. \tag{5.23}$$

Therefore, any state that violates this criterion must be entangled. If we use the simplifications $a_A = \frac{1}{d_A^2}$ and $a_B = \frac{1}{d_B^2}$ for the special case of SIC-POVMs, equation (5.23) coincides with the enhanced SIC criterion [16]. In this thesis we only examine bipartite states with subsystems of equal dimension $d = d_A = d_B$. In addition, we set the parameter $t = t_A = t_B$. Therefore, also $a = a_A = a_B$ holds. Thus, the resulting GSIC criterion denoted by $\mathscr{C}_{GSIC}$ detects entanglement if

$$\mathscr{C}_{GSIC} = \|\mathcal{P}\|_{Tr} - \frac{ad^2 + 1}{d(d+1)} > 0. \tag{5.24}$$

In the case of SIC-POVMs, we insert $d = \frac{1}{d^2}$. From this it follows that the SIC criterion $\mathscr{C}_{SIC}$ detects entanglement if

$$\mathscr{C}_{SIC} = \|\mathcal{P}\|_{Tr} - \frac{2}{d(d+1)} > 0. \tag{5.25}$$

6. The Magic Simplex

The magic simplex is an intriguing object in the state space of bipartite qudits that exhibits numerous symmetries. It is shaped by mixtures of generalized Bell states, which will be discussed in the beginning of this chapter. Following the formal definition of the magic simplex, we will present the concept of line states and how they give rise to a kernel including only separable states. In order to simplify the separability problems in the magic simplex, we will have a look into entanglement-class conserving symmetries. Furthermore, we will discuss a lower bound of the concurrence that was derived specifically to detect entangled states in the magic simplex. In the end of this chapter, we will provide an overview of the state families that will be investigated in the remainder of this thesis.

6.1. ONB with Maximally Entangled States

In the third chapter, we discussed quantum entanglement in bipartite systems. Thereby, we mentioned that a bipartite state is maximally entangled if all Schmidt coefficients are non-vanishing and equal. For the case of bipartite qubit states, an orthonormal basis (ONB) of pure maximally entangled states is given by the so-called Bell states [23]

$$\begin{aligned} \left|\Phi^{\pm}\right\rangle &= \frac{1}{\sqrt{2}}(|0,0\rangle \pm |1,1\rangle), \\ \left|\Psi^{\pm}\right\rangle &= \frac{1}{\sqrt{2}}(|0,1\rangle \pm |1,0\rangle). \end{aligned} \tag{6.1}$$

To find such a basis in arbitrary $d \times d$ systems with $d \geq 2$, we consider the seed state

$$|\Omega_{0,0}\rangle = \frac{1}{\sqrt{d}} \sum_{i=0}^{d-1} |i,i\rangle\,, \tag{6.2}$$

which can be seen as a generalization of $|\Phi^{+}\rangle$. By applying Weyl operators to $|\Omega_{0,0}\rangle$, we obtain an ONB consisting of d^2 maximally entangled states of the form [50]

$$|\Omega_{k,l}\rangle = (W_{k,l} \otimes \mathbb{1}_d)\,|\Omega_{0,0}\rangle\,. \tag{6.3}$$

In this thesis, we refer to these states as generalized Bell states. Their density matrices are given by the Bell projection operators

$$P_{k,l} = |\Omega_{k,l}\rangle\,\langle\Omega_{k,l}|\,. \tag{6.4}$$

6.2. Definition of the Magic Simplex

The concept of the magic simplex is partly borrowed from geometry. Broadly speaking, a k-simplex can be viewed as the k-dimensional generalization of a triangle. Its geometric shape describes a polytope given by the convex hull of $k+1$ vertices. These, in turn, must correspond to affinely independent points $\vec{p}_0, \ldots, \vec{p}_k \in \mathbb{R}^k$. Hence, we require that the point subtractions $\vec{p}_1 - \vec{p}_0, \ldots, \vec{p}_k - \vec{p}_0 \in \mathbb{R}^k$ are linearly independent. Let us consider the coefficients $\lambda_1, \ldots, \lambda_k$. Then, the k-simplex $\mathcal{S}_k$ is defined by

$$\mathcal{S}_k = \{\sum_{i=0}^{k} \lambda_i \, \vec{p}_i | \lambda_i \geq 0, \sum_{i=0}^{k} \lambda_i = 1\}. \tag{6.5}$$

Analog to the k-simplex, we can define the magic simplex as convex combinations of the Bell projection operators $P_{k,l}$. Consider the Bell coefficients $\lambda_{k,l}$. Then, the magic simplex is given by [19]

$$\mathcal{M}_d = \{\sum_{k,l=0}^{d-1} \lambda_{k,l} P_{k,l} | \lambda_{k,l} \geq 0, \sum_{k,l=0}^{d-1} \lambda_{k,l} = 1\}. \tag{6.6}$$

A key property of all states in the magic simplex is that they are locally maximally mixed. This means that taking the partial trace over a subsystem of any $\rho \in \mathcal{M}_d$ results in the maximally mixed state $Tr_A(\rho) = Tr_B(\rho) = \frac{1}{d}\mathbb{1}_d$. For bipartite qubit systems, the magic simplex contains all locally maximally mixed states, which is not the case in higher dimensions [51].

6.3. A Kernel Including only Separable States

A simplified way of handling the magic simplex can be achieved by utilizing its symmetries, which render specific mixtures of generalized Bell states equivalent regarding separability. Let us again consider the Bell projection operators. Each $P_{k,l}$ can be identified by a point in the discrete classical phase space [19, 52], where the index k represents the coordinate of the momentum and l indicates the coordinate of the position. Together, the Bell projection operators form a point lattice as depicted in figure 6.1 for the case of $d = 3$. If d is not a prime number, there can furthermore also exist sublattices. It follows from the definition of generalized Bell states that an arbitrary point $P_{k,l}$ in the discrete classical phase space can be transformed into $P_{k+p,l+q}$ by calculating

$$W_{p,q} P_{k,l} W_{p,q}^{\dagger} = P_{k+p,l+q}, \tag{6.7}$$

where $W_{p,q}$ is a suitable Weyl operator and we assume the modulus d. Now, consider a set of Weyl operators $\{W_{p,q}^n\}_{n=0}^{d-1}$ and apply each on the same $P_{k,l}$. The resulting set of points $\{P_{k+np,l+nq}\}_{n=0}^{d-1}$ creates a line in the phase space. An equal mixture of these Bell projection operators forms a so-called line state [19], which is always separable. In each $d \times d$ system, the combined number of lines and sublattices with d points is given by $N(d) = d(d + 1 + \sum_i b_i)$, where the b_i's are integer divisors of d. As an example, let us take a look at our phase-space lattice for $d = 3$. In figure 6.1, we marked four non-parallel lines with red color. Together with all parallel-shifted lines, we obtain in total 12 lines, which corresponds to a complete set of line states for bipartite qutrits.

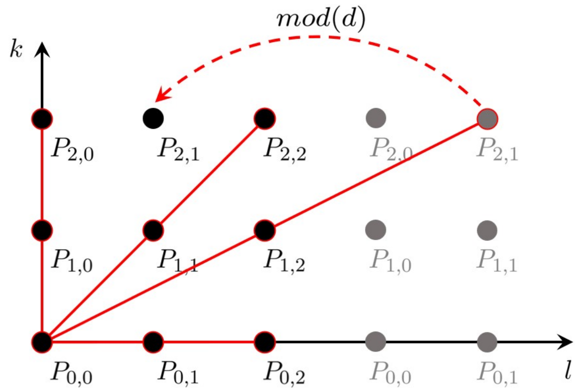

Figure 6.1.: Illustration of the discrete classical phase space formed by the Bell projection operators $P_{k,l}$ for $d = 3$. The four non-parallel phase space lines are marked with red color.

Since all line states $\rho_{line\,i}$ are separable, every convex combination of line states must also be separable. This gives rise to the kernel polytope

$$\mathcal{K}_d = \{\sum_i c_i \, \rho_{line\,i} | c_i \geq 0, \sum_i c_i = 1\}, \tag{6.8}$$

which marks a region in the magic simplex that only consists of separable states. A closely related geometrical object inside the magic simplex is the so-called enclosure polytope given by [19, 51]

$$\mathcal{E}_d = \{\sum_{k,l=0}^{d-1} \lambda_{k,l} P_{k,l} | \lambda_{k,l} \in [0, \frac{1}{d}], \sum_{k,l=0}^{d-1} \lambda_{k,l} = 1\}. \tag{6.9}$$

Overall, the states in this polytope are not necessarily separable. However, any magic simplex state outside of $\mathcal{E}_d$ must be free entangled. In the two-qubit magic simplex, the kernel polytope and the enclosure polytope are the same. This means that for $\mathcal{M}_2$ these two geometrical objects are sufficient to fully solve the separability problem. On the other hand, in higher dimensions, the two polytopes do not fully coincide with each other. The states inside the enclosure polytope but outside the kernel polytope can be either separable, bound entangled or free entangled.

In general, the concept of the kernel polytope can be generalized beyond the line states. Since every convex combination of arbitrary separable states remains separable, we can utilize customized separable states to create an extended polytope that covers a greater area of separable states than an exclusive combination of line states.

6.4. Entanglement-Class-Conserving Symmetries

In the context of this thesis, we mainly classify states according to whether they are separable, bound entangled, or free entangled. These three properties can be summarized by the term entanglement class. The structure of the magic simplex gives rise to a group S of symmetry transformations that conserve the respective entanglement class of any state $\rho \in \mathcal{M}_d$ [20, 51]. This means that each transformation $s \in S$ maps

$$\begin{aligned} s &: \Omega_{sep} \cap \mathcal{M}_d \to \Omega_{sep} \cap \mathcal{M}_d, \\ s &: \Omega_{bound} \cap \mathcal{M}_d \to \Omega_{bound} \cap \mathcal{M}_d, \\ s &: \Omega_{free} \cap \mathcal{M}_d \to \Omega_{free} \cap \mathcal{M}_d, \end{aligned} \tag{6.10}$$

where Ω_{sep}, Ω_{bound}, and Ω_{free} are the sets of separable, bound entangled, and free entangled states. To describe the symmetry transformations in S more closely, let us again consider a point lattice of Bell projection operators in the discrete classical phase space. The group elements of S correspond to point transformations and translations in the phase space that can be implemented through suitable Weyl operators. In detail, the generators of S are translations $P_{k,l} \to P_{k+m,l+n}$, momentum inversion $P_{k,l} \to P_{-k,l}$, quarter rotation $P_{k,l} \to P_{l,-k}$, and vertical shear $P_{k,l} \to P_{k+l,l}$ [51]. By definition, all magic simplex states can be written in the form $\rho = \sum_{k,l} \lambda_{k,l} P_{k,l}$. It turns out that the symmetry transformations induced by the discussed generators result in certain permutations of the Bell projection operators. Collectively, the discrete classical phase space consists of a finite number of $P_{k,l}$'s. Therefore, we can only find a finite number of symmetries. In the case of the two-qutrit magic simplex, there exist 432 permutations of Bell projection operators that act as entanglement-class-conserving symmetry transformations [20].

6.5. Quasi-Pure Concurrence

In the previous chapters, we discussed several criteria that have the capability to detect (some) entangled states. Furthermore, we presented the Schmidt decomposition as a method for recognizing pure maximally entangled states in the case of bipartite systems. In some way, the concurrence [53] goes one step further. This quantity is a non-negative function that monotonically increases with the amount of entanglement. Therefore, the concurrence C can be used as a measure of entanglement. Its minimum value is zero, and the maximum value of C is one. Generally, the concurrence detects entanglement if $C > 0$. For bipartite pure states $|\psi\rangle$ of arbitrary dimension, the concurrence is given by [54]

$$C(\psi) = \sqrt{\langle\psi| \otimes \langle\psi| \mathcal{A} |\psi\rangle \otimes |\psi\rangle}, \tag{6.11}$$

where the projection-valued measure $\mathcal{A} = 4\sum_{i<j,k<l}(|i,k,j,l\rangle - |j,k,i,l\rangle - |i,l,j,k\rangle + |j,l,i,k\rangle) \cdot (h.c.)$ [21]. Note that the indices i and j correspond to the basis vectors of the first subsystem, whereas k and l denote the basis vectors of the second subsystem.
In the case of mixed states, the situation is much more complicated. For two-qubit states there exists an explicit solution [55] for the concurrence, but in higher-dimensional systems we must rely on algebraic estimates. Consider weakly mixed states with the spectral decomposition $\rho = \sum_i \mu_i |\psi_i\rangle \langle\psi_i|$, where μ_i are the eigenvalues and $|\psi_i\rangle$ the eigenstates of ρ. In this case, an estimate for the lower bound of the concurrence [21, 56] can be derived from the matrix $\mathcal{T}$, which entries are defined by

$$\mathcal{T}_{ij} = \sqrt{\mu_i \mu_j}\, \langle\psi_i| \otimes \langle\psi_j|\chi\rangle\,. \tag{6.12}$$

Note that $|\chi\rangle \propto \mathcal{A}\,|\psi_0\rangle \otimes |\psi_0\rangle$ and $|\psi_0\rangle$ is the eigenvector that corresponds to the largest eigenvalue of our weakly mixed state. Calculating the singular values of $\mathcal{T}$ gives us an expression for the lower bound of C. This so-called quasi-pure concurrence C_{qp} results in

$$C_{qp}(\rho) = \max(0, S_0 - \sum_{i>0} S_i), \tag{6.13}$$

where S_i are the singular values of $\mathcal{T}$ and S_0 indicates the largest singular value. Let us now specifically consider the magic simplex. From equation (6.6) we know that all states in $\mathcal{M}_d$ can be written in terms of $\rho = \sum_{k,l} \lambda_{k,l} P_{k,l}$ with the probabilities $\lambda_{k,l}$ and the Bell projection operators $P_{k,l} = |\Omega_{k,l}\rangle \langle\Omega_{k,l}|$. However, this equation also aligns with the spectral decomposition of ρ. Consequently, we can interpret the $\lambda_{k,l}$'s as the eigenvalues and the $|\Omega_{k,l}\rangle$'s as the eigenstates of any $\rho \in \mathcal{M}_d$. Let $\lambda_{n,m}$ be the largest eigenvalue. By choosing $|\chi\rangle \propto A\,|\Omega_{n,m} \otimes \Omega_{n,m}\rangle$, the singular values $S_{k,l}$ of $\mathcal{T}$ result in [21]

$$S_{k,l} = \sqrt{\frac{d}{2(d-1)}\lambda_{k,l}[(1-\frac{2}{d})\lambda_{n,m}\delta_{k,n}\delta_{l,m} + \frac{1}{d^2}\lambda_{(2n-k)mod(d),(2m-l)mod(d)}]}. \tag{6.14}$$

Analogously to equation (6.13), the quasi-pure concurrence for weakly mixed states in the magic simplex is given by $C_{qp}(\rho) = \max(0, S_{n,m} - \sum_{(k,l)\neq(n,m)} S_{k,l})$, where $S_{n,m}$ denotes the largest singular value.

6.6. State Families

In the next two chapters, we will examine separability problems in several families of states within the magic simplex. Most of the time, our focus lies on two-qutrit systems, but we will also test some of the discussed criteria in higher-dimensional systems.
Two interesting slices of the two-qutrit magic simplex are families A and B. Family A [57, 52] can be described by a mixture of three Bell projection operators and the maximally mixed state. The ratio of this mixture depends on the three parameters α, β, and γ. Altogether,

family A is given by

$$\rho_A = \frac{(1-\alpha-\beta-\gamma)}{9}\mathbb{1}_9 + \alpha P_{0,0} + \beta P_{0,1} + \gamma P_{0,2}. \tag{6.15}$$

For $\alpha = \beta = \gamma = \frac{1}{3}$ we obtain a line state, whereas $\alpha = \beta = \gamma = 0$ gives rise to the maximally mixed state. In this thesis, we will set $\gamma = 0$, while varying the other two parameters. Let us denote this subfamily of states as family A1.
The structure of family B [57, 9] is more complicated. It involves a mixture of nine Bell projection operators as well as the maximally mixed state. In total, the whole family is characterized by the four parameters α, β, γ, and δ. Its density matrix results in

$$\rho_B = (1 - \frac{\alpha}{5} - \frac{\beta}{4} - \gamma - \delta)\frac{1}{9}\mathbb{1}_9 + \frac{\alpha}{5}P_{0,0} + \frac{\beta}{8}\sum_{i=1}^{2} P_{i,0} + \frac{\gamma}{2}\sum_{i=0}^{2} P_{i,1} + \frac{\delta}{3}\sum_{i=0}^{2} P_{i,2}. \tag{6.16}$$

Families B1, B2, and B3 denote simplified versions of family B, where we assigned fixed numerical values to two parameters each. The definitions of these subfamilies are given in table 6.1.

Family	Fixed Parameters
B1	$\gamma = -\frac{1}{\sqrt{3}}$, $\delta = 0$
B2	$\gamma = -0.83$, $\delta = 0$
B3	$\alpha = \frac{5}{3}(-1+\sqrt{3})$, $\beta = -\frac{1}{10}$

Table 6.1.: Subfamilies of ρ_B.

Kilian's state family [9] describes an extension of family B for arbitrary $d \times d$ systems. Overall, it contains a mixture of d^2 Bell projection operators and the maximally mixed state. The whole family is characterized by a set of $d+1$ parameters $\{q(i)\}_{i=1}^{d+1}$ and defined by the density matrix

$$\begin{aligned}\rho_K = &\left(1 - \frac{q(1)}{d^2-(d+1)} - \frac{q(2)}{d+1} + \sum_{j=3}^{d+1}(-q(j))\right)\frac{1}{d^2}\mathbb{1}_{d^2} + \frac{q(1)}{d^2-(d+1)}P_{0,0} + \\ &\frac{q(2)}{(d+1)(d-1)}\sum_{i=1}^{d-1} P_{i,0} + \sum_{j=3}^{d+1}\sum_{i=0}^{d-1}\frac{q(j)}{d}P_{i,j-2}.\end{aligned} \tag{6.17}$$

For $d = 4$, $d = 5$, and $d = 6$, we will examine certain subfamilies of ρ_K. Their fixed parameters are listed in table 6.2.

Family	d	Fixed Parameters
K4	4	$q(1) = 2 + \frac{1}{16}$, $q(2) = 0$, $q(4) = \frac{3}{16}$
K5a	5	$q(1) = \frac{19}{25}(13 - 5\sqrt{5})$, $q(2) = -\frac{48}{25}$, $q(3) = q(6) = \frac{1}{5} - \frac{1}{\sqrt{5}}$
K5b	5	$q(1) = \frac{228-95\sqrt{5}}{25}$, $q(2) = -\frac{72}{25}$, $q(4) = q(5) = -\frac{1}{\sqrt{5}}$
K6a	6	$q(1) = -\frac{29}{72}(-20 + 7\sqrt{6})$, $q(2) = -\frac{35}{72}(4 + \sqrt{6})$, $q(4) = q(5) = q(6) = -\frac{1}{\sqrt{6}}$
K6b	6	$q(1) = -\frac{29}{72}(-22 + 7\sqrt{6})$, $q(2) = -\frac{35}{72}(2 + \sqrt{6})$, $q(3) = q(5) = q(7) = \frac{1}{6} - \frac{1}{\sqrt{6}}$

Table 6.2.: Subfamilies of ρ_K.

7. Bound Entanglement Detection in Bipartite Systems

In the course of this chapter we aim to detect bound entanglement in the magic simplex using GSIC-POVMs and SIC-POVMs. In the first section, we examine the case for bipartite qutrit states. Therefore, we apply $\mathscr{C}_{GSIC}$ and $\mathscr{C}_{SIC}$ to families A1, B1, B2, and B3 and compare the results to the bound entangled areas obtained by the quasi-pure concurrence and the MUB witness. Since the MUB witness still detects bound entanglement for incomplete sets of MUBs [43], we also examine whether $\mathscr{C}_{GSIC}$ and $\mathscr{C}_{SIC}$ retain this capability if we leave out one GSIC/SIC operator. In the second section of this chapter, we focus on higher-dimensional systems. Therefore, we examine selected state families that belong to ρ_K for $d = \{4, 5, 6\}$. Similarly to before, we apply $\mathscr{C}_{GSIC}$ and $\mathscr{C}_{SIC}$ to these states. For $d = 4$ and $d = 5$ we compare the results to the bound entangled areas detected by the MUB witness. In $d = 6$ we use the bound entangled areas obtained by the generalized linear witness as a reference.
In this (and also the next) chapter we plot the examined state families as functions of their state parameters. The families are modeled in such a way that the values of the state parameters have to be in certain numerical ranges to satisfy the positivity criterion and therefore constitute well-defined states. In our figures, these areas are marked with green, blue, and red shapes. The subset of blue and red areas indicates PPT, and the red shapes show the areas in which either the MUB witness, the generalized linear witness, or the quasi-pure concurrence detect bound entanglement. On top of that, the results of $\mathscr{C}_{GSIC}$ or $\mathscr{C}_{SIC}$ are represented by rainbow spectra. We mention the specific criteria used, if relevant, in the text and captions of the figures in question.

7.1. Bipartite Qutrit Systems

7.1.1. Complete GSIC- & SIC-POVMs

Consider the GSIC and SIC operators given in equations (5.10) and (5.17). The resulting expressions for $\mathscr{C}_{GSIC}$ and $\mathscr{C}_{SIC}$ detect entanglement if

$$\mathscr{C}_{GSIC} = \|\mathcal{P}\|_{Tr} - \frac{9a+1}{12} > 0, \quad \mathscr{C}_{SIC} = \|\mathcal{P}\|_{Tr} - \frac{1}{6} > 0. \tag{7.1}$$

For our calculations that involve the three-dimensional GSIC criterion, we set the parameter $t = 0.012$. This choice leads to the maximum violation of the separability bound for the entangled states obtained.
Let us start with applying the GSIC criterion to families A1, B1, B2, and B3. The results are shown in figure 7.1. In family A1 the region that satisfies $\mathscr{C}_{GSIC} > 0$ borders the PPT area, but there is no overlap between these regions. Therefore, $\mathscr{C}_{GSIC}$ detects all free entangled states in family A1 but does not obtain any bound entanglement. In contrast, calculating the

quasi-pure concurrence, we find two small bound entangled areas that are represented by red shapes in figure 7.1a.

For families B1 and B2, the regions that satisfy $\mathscr{C}_{GSIC} > 0$ actually intersect the PPT areas. In both state families $\mathscr{C}_{GSIC}$ detects less free entangled states than the Peres-Horodecki criterion, but obtains substantial areas of bound entangled states. In figures 7.1b–7.1c the red shapes indicate the bound entangled states found by the MUB witness. Comparing these areas with the results of the GSIC citerion, we conclude that in families B1 and B2, $\mathscr{C}_{GSIC}$ detects bound entanglement more successfully than the MUB witness.

In family B3 $\mathscr{C}_{GSIC}$ detects all free entangled states and also large regions consisting of bound entangled states. In figure 7.1d the bound entangled states detected by the MUB witness are marked by two red shapes. Again, by comparing the results, we can clearly see that $\mathscr{C}_{GSIC}$ outperforms the MUB witness.

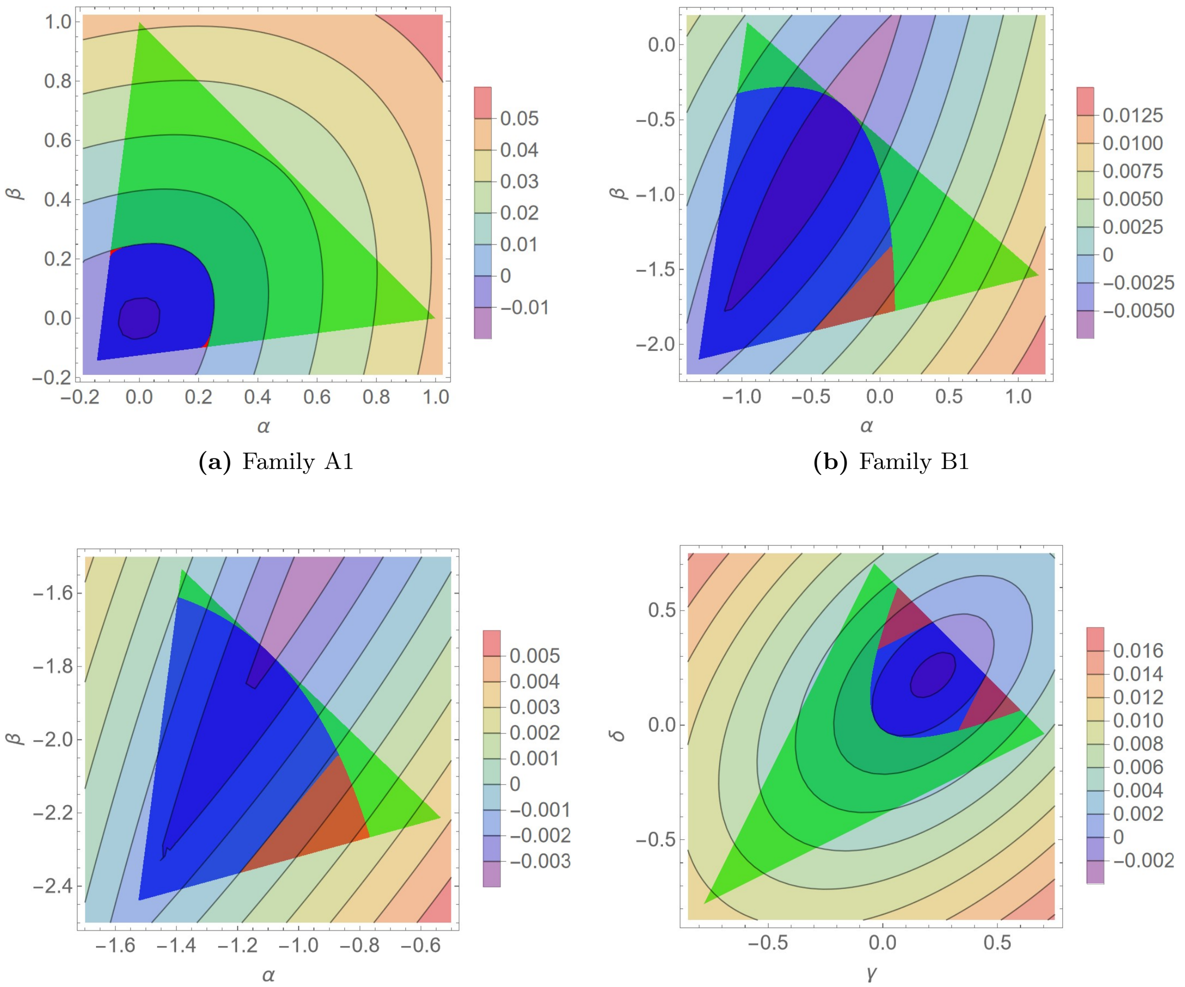

(a) Family A1

(b) Family B1

(c) Family B2

(d) Family B3

Figure 7.1.: The results of $\mathscr{C}_{GSIC}$ are represented by the rainbow spectra. In (a) the red shapes mark the area where the quasi-pure concurrence detects bound entanglement. In (b)–(d) the red shapes show the regions in which the MUB witness detects bound entanglement.

Next we apply the SIC citerion to families A1, B1, B2, and B3. The results are shown in figure 7.2. It turns out that $\mathscr{C}_{SIC}$ detects exactly the same free and bound entangled areas as $\mathscr{C}_{GSIC}$. This is not entirely surprising considering that SIC-POVMs satisfy all definition equations of GSIC-POVMs and can therefore be viewed as a special case of GSIC-POVMs. However, comparing the results from $\mathscr{C}_{SIC}$ and $\mathscr{C}_{GSIC}$ we find one difference. That is, the gradient of $\mathscr{C}_{SIC}$ is steeper. It follows that for the entangled states obtained, the separability bound is violated more strongly for $\mathscr{C}_{SIC}$.

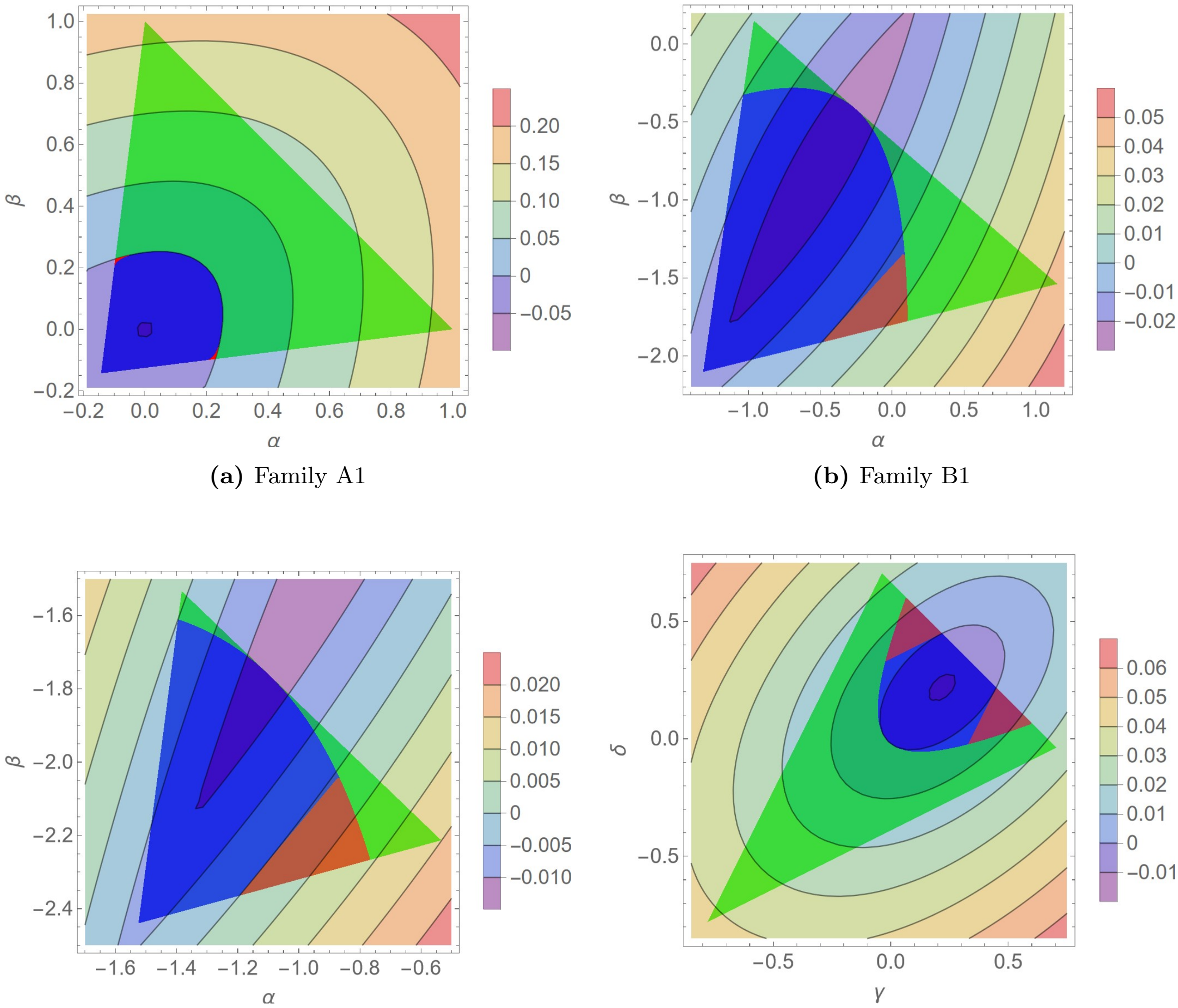

(a) Family A1

(b) Family B1

(c) Family B2

(d) Family B3

Figure 7.2.: The results of $\mathscr{C}_{SIC}$ are represented by the rainbow spectra. In (a) the red shapes mark the area where the quasi-pure concurrence detects bound entanglement. In (b)–(d) the red shapes show the regions in which the MUB witness detects bound entanglement.

Looking at the results of $\mathscr{C}_{GSIC}$ and $\mathscr{C}_{SIC}$, the question arises whether any criterion could potentially do better in detecting bound entanglement in families B1, B2, and B3. Have we even detected all bound entangled states in these state families? We will revisit these considerations in the next chapter.

7.1.2. Incomplete GSIC- & SIC-POVMs

As we have seen in the fifth chapter, the bound for $\mathscr{C}_{GSIC}$ is derived by using equation (5.19). For $d = 3$, this expression simplifies to

$$\sum_{\alpha=1}^{9} p_\alpha^2 \leq \frac{9a+1}{12}. \tag{7.2}$$

Let us now consider any incomplete GSIC-POVM consisting of 8 such measurements. This means that the i-th GSIC operator P_i is left out. For such a configuration it makes sense to alter equation (7.2) to

$$\sum_{\alpha \neq i} p_\alpha^2 \leq \frac{9a+1}{12} - \min\{p_i^2\}. \tag{7.3}$$

The minimum of $p_i^2 = (Tr(P_i \rho))^2$ can be calculated by applying all unitary transformations U to the seed state $\rho = U |0\rangle \langle 0| U^\dagger$. The general form of U is found through composite parameterization of unitary groups [44, 45] and was calculated using the Wolfram Mathematica package "Composite parameterization and Haar measure for unitary groups" [46]. Leaving out the i-th GSIC operator also changes $\mathcal{P}$ to a 8×8-matrix. Using equation (7.3) and following the same procedure as for the deviations of $\mathscr{C}_{GSIC}$, we obtain criteria $\mathscr{C}_{GSIC \setminus P_i}$ for the discussed incomplete GSIC-POVMs. The various $\mathscr{C}_{GSIC \setminus P_i}$ detect entanglement if

$$\mathscr{C}_{GSIC \setminus P_i} = \|\mathcal{P}\|_{Tr} - \frac{9a+1}{12} + \min\{p_i^2\} > 0. \tag{7.4}$$

Using the GSIC operators from equation (5.10),

$$\begin{aligned}
&\min\{p_1^2\} = 0.000410892, \quad \min\{p_2^2\} = 0.000340122, \quad \min\{p_3^2\} = 0.000289205, \\
&\min\{p_4^2\} = 0.000410892, \quad \min\{p_5^2\} = 0.00177793, \quad \min\{p_6^2\} = 0.0000668195, \\
&\min\{p_7^2\} = 0.000235938, \quad \min\{p_8^2\} = 0.0000901996, \quad \min\{p_9^2\} = 0.000758359.
\end{aligned} \tag{7.5}$$

Since SIC-POVMs can be viewed as a special case of GSIC-POVMs, equation (7.4) also gives rise to criteria $\mathscr{C}_{SIC \setminus \Pi_i}$ for incomplete SIC-POVMs consisting of 8 operators Π_i. Note that in this case we obtain $a = 1/9$ and $\min\{p_i^2\} = 0$, $\forall i \in 1, 2, ..., 9$. Therefore, the respective $\mathscr{C}_{SIC \setminus \Pi_i}$ detect entanglement if

$$\mathscr{C}_{SIC \setminus \Pi_i} = \|\mathcal{P}\|_{Tr} - \frac{1}{6} > 0. \tag{7.6}$$

Let us start with the GSIC criteria consisting of eight GSIC operators. Again, we examine state families A1, B1, B2, and B3. Figures 7.3–7.4 show the results of $\mathscr{C}_{GSIC \setminus P_5}$ and $\mathscr{C}_{GSIC \setminus P_7}$. The outcomes of the remaining criteria can be found in the appendix. For reasons of comparison, we also apply a MUB witness consisting of an incomplete set of mutually unbiased bases to families A1, B1, B2 and B3. Using three MUBs, we detect a small region of bound entangled states in family B2. In figures 7.3c and 7.4c this area is marked by a red shape. Unlike this MUB witness, neither of the $\mathscr{C}_{GSIC\setminus P_i}$ detects any bound entanglement in the examined state families.

However, the situation changes when it comes to obtaining free entanglement. In family A1 all $\mathscr{C}_{GSIC\setminus P_i}$ detect free entangled areas. In total, each of these regions is substantially smaller than the free entangled area obtained by $\mathscr{C}_{GSIC}$. Also, looking at the different $\mathscr{C}_{GSIC\setminus P_i}$, the results slightly vary depending on which GSIC operator P_i is left out. Comparing the results of $\mathscr{C}_{GSIC\setminus P_5}$ and $\mathscr{C}_{GSIC\setminus P_7}$, these differences are especially obvious. It turns out that in family A $\mathscr{C}_{GSIC\setminus P_5}$ detects a larger area of free entangled states than $\mathscr{C}_{GSIC\setminus P_7}$. In families B1, B2, and B3 we can also find visible deviations comparing the results of the different $\mathscr{C}_{GSIC\setminus P_i}$. Unfortunately, none of these criteria detect any free entanglement in these families.

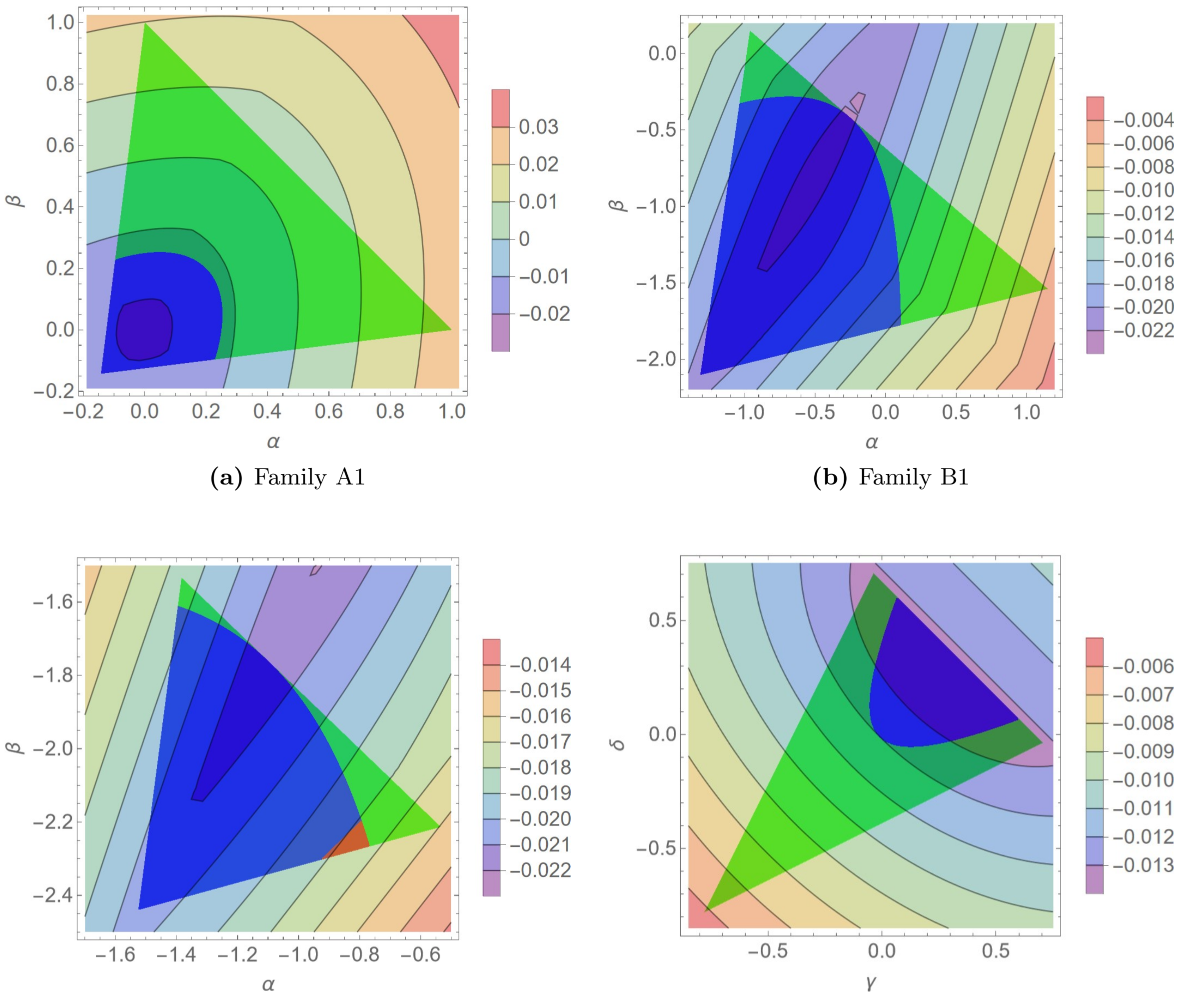

(a) Family A1

(b) Family B1

(c) Family B2

(d) Family B3

Figure 7.3.: The results of $\mathscr{C}_{GSIC\setminus P_5}$ are represented by the rainbow spectra. In (c) the red shapes show the regions in which the MUB witness consisting of three mutually unbiased bases detects bound entanglement.

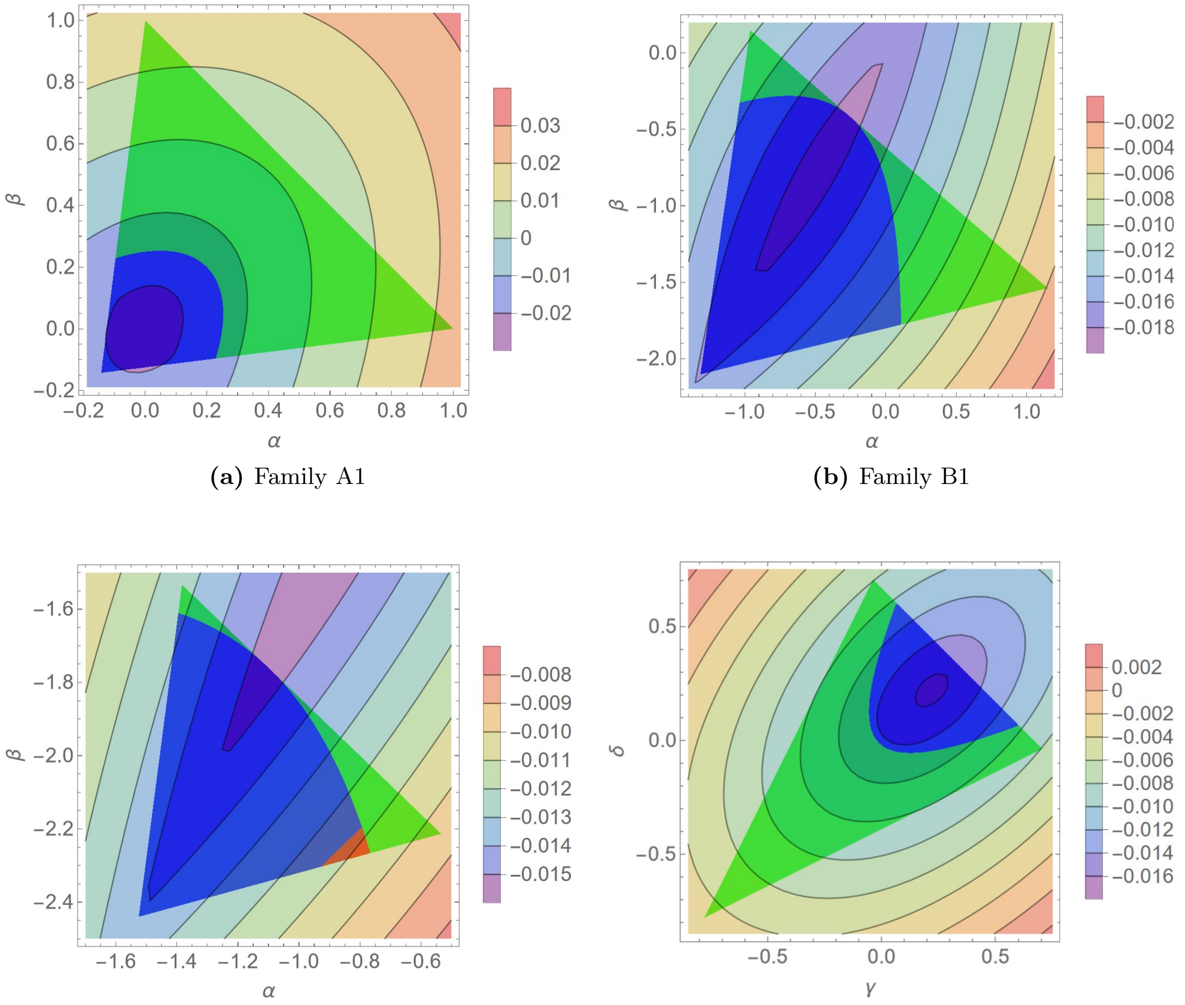

(a) Family A1

(b) Family B1

(c) Family B2

(d) Family B3

Figure 7.4.: The results of $\mathscr{C}_{GSIC\setminus P_7}$ are represented by the rainbow spectra. In (c) the red shapes show the regions in which the MUB witness consisting of three mutually unbiased bases detects bound entanglement.

Next, let us apply the SIC criteria $\mathscr{C}_{SIC\setminus\Pi_i}$ to families A1, B1, B2, and B3. The results are shown in figure 7.5. This figure represents the outcomes for all $i \in 1, 2, ..., 9$, meaning that for the examined state families, the results do not depend on which SIC operator Π_i is left out. Overall, the $\mathscr{C}_{SIC\setminus\Pi_i}$ do not detect any bound entanglement in the tested state families, but we obtain free entanglement in families A1, B1, and B3. In family A1, the free entangled region obtained is smaller than the area detected for $\mathscr{C}_{SIC}$. However, it is still larger than the free entangled area obtained by any $\mathscr{C}_{GSIC\setminus P_i}$. In families B1 and B3 the $\mathscr{C}_{SIC\setminus\Pi_i}$ also detect smaller areas of free entangled states than $\mathscr{C}_{SIC}$. Still, the circumstance that we find any entangled states in families B1 and B3, indicates that $\mathscr{C}_{SIC\setminus\Pi_i}$ could be more effective criteria than all $\mathscr{C}_{GSIC\setminus P_i}$.

It is quite surprising that $\mathscr{C}_{GSIC\setminus P_i}$ and $\mathscr{C}_{SIC\setminus\Pi_i}$ detect different entangled areas, as for complete GSIC/SIC-POVMs $\mathscr{C}_{GSIC}$ and $\mathscr{C}_{SIC}$ obtain the same entangled areas in the tested families. The differences between the GSIC-POVMs and SIC-POVMs used seem to have less impact on the effectiveness of the entanglement detection when we use complete sets of GSIC/SIC operators.

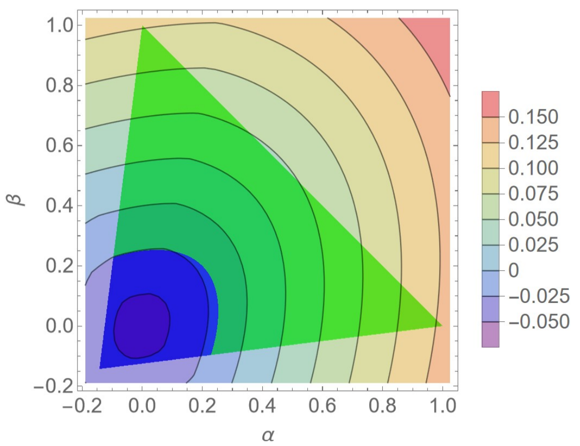

(a) Family A1

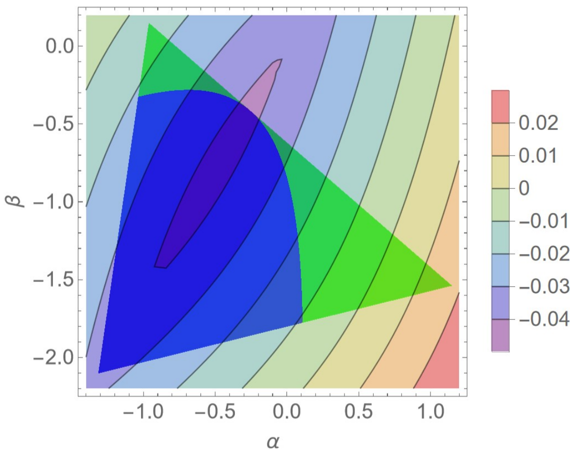

(b) Family B1

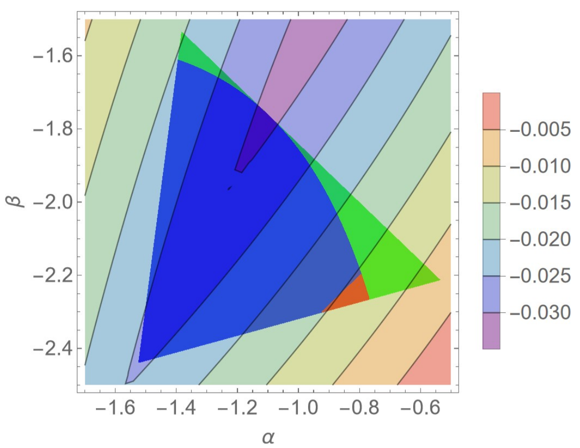

(c) Family B2

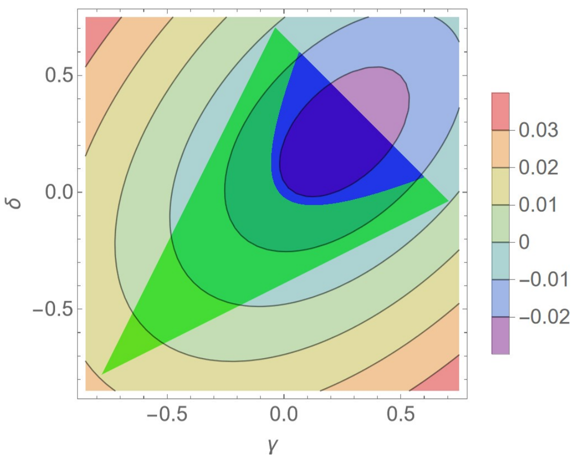

(d) Family B3

Figure 7.5.: The results of $\mathscr{C}_{SIC\backslash\Pi_i}$ $(i \in 1, 2, ..., 9)$ are represented by the rainbow spectra. In (c) the red shapes show the regions in which the MUB witness consisting of three mutually unbiased bases detects bound entanglement.

In summary, we do not detect any bound entanglement using incomplete GSIC/SIC-POVMs. However, this does not mean that $\mathscr{C}_{GSIC\backslash P_i}$ and $\mathscr{C}_{SIC\backslash\Pi_i}$ cannot detect bound entanglement in general. Perhaps, we would be more successful in detecting bound entanglement in other state families with more suitable symmetries.

Another interesting question is if we can further optimize $\mathscr{C}_{GSIC\backslash P_i}$ and $\mathscr{C}_{SIC\backslash\Pi_i}$ by deriving tighter separability bounds. For $\mathscr{C}_{GSIC\backslash P_i}$, this remains an open question. On the other hand, a tighter separability bound is not possible for any $\mathscr{C}_{SIC\backslash\Pi_i}$, since there exist separable states that already saturate the existing bounds:

$$\begin{aligned}
&\mathscr{C}_{SIC\setminus\Pi_1} = \mathscr{C}_{SIC\setminus\Pi_2} = \mathscr{C}_{SIC\setminus\Pi_3} = 0 \quad \text{for} \quad \rho = |0,0\rangle\langle 0,0|\,, \\
&\mathscr{C}_{SIC\setminus\Pi_4} = \mathscr{C}_{SIC\setminus\Pi_5} = \mathscr{C}_{SIC\setminus\Pi_6} = 0 \quad \text{for} \quad \rho = |1,1\rangle\langle 1,1|\,, \\
&\mathscr{C}_{SIC\setminus\Pi_7} = \mathscr{C}_{SIC\setminus\Pi_8} = \mathscr{C}_{SIC\setminus\Pi_9} = 0 \quad \text{for} \quad \rho = |2,2\rangle\langle 2,2|\,.
\end{aligned} \tag{7.7}$$

7.2. Higher Dimensions

In the first section of this chapter, we compared the results of $\mathscr{C}_{GSIC}$ and $\mathscr{C}_{SIC}$ for several state families in $d = 3$. Thereby, we observed that using complete GSIC-POVMs and SIC-POVMs both criteria detect the same entangled areas. The only difference we could tell was the steeper gradient of $\mathscr{C}_{SIC}$, which results in more strongly violated separability bounds for the entangled states obtained. These observations for $\mathscr{C}_{GSIC}$ and $\mathscr{C}_{SIC}$ also uphold for the state families tested in higher dimensions. To reduce the amount of repetitiveness, we will show only the results of $\mathscr{C}_{SIC}$ in this section. The results of $\mathscr{C}_{GSIC}$ can be found in the appendix.

7.2.1. Bipartite Ququart Systems

To construct a SIC-POVM in $d = 4$, we take the fiducial vector from [58, 59]. The normalized version of this vector is given by

$$|\psi_f\rangle = \begin{pmatrix} \frac{1}{2}\sqrt{\frac{1}{10}(2+\sqrt{2})(5-\sqrt{5})} \\ \frac{(\frac{1}{4}-\frac{i}{4})((1-i)+\sqrt{2})(-1+\sqrt{5}+(1+i)\sqrt{1+\sqrt{5}})}{\sqrt{2(2+\sqrt{2})(5-\sqrt{5})}} \\ \frac{i(-5+\sqrt{5})}{2\sqrt{5(2+\sqrt{2})(5-\sqrt{5})}} \\ \frac{(\frac{1}{4}-\frac{i}{4})((1-i)+\sqrt{2})(-1+\sqrt{5}-(1+i)\sqrt{1+\sqrt{5}})}{\sqrt{2(2+\sqrt{2})(5-\sqrt{5})}} \end{pmatrix}. \tag{7.8}$$

Using equation (5.15), we construct a complete set of SIC vectors. It can be found in the appendix. For bipartite ququart states, the SIC criterion detects entanglement if

$$\mathscr{C}_{SIC} = \|\mathcal{P}\|_{Tr} - \frac{1}{10} > 0. \tag{7.9}$$

Figure 7.6 shows the results for family K4. In this family, $\mathscr{C}_{SIC}$ detects both free and bound entangled areas. The latter correspond exactly to the bound entangled regions obtained by the MUB witness, which are marked by red shapes. In this region $\mathscr{C}_{SIC}$ behaves locally like a linear witness. Examining the free entangled areas detected, $\mathscr{C}_{SIC}$ shows its non-linear nature. Here, the SIC criterion obtains free entangled states close to the edge of the green positivity triangle. However, it fails to detect the free entangled states further inside the triangle that were found by the Peres-Horodecki criterion.

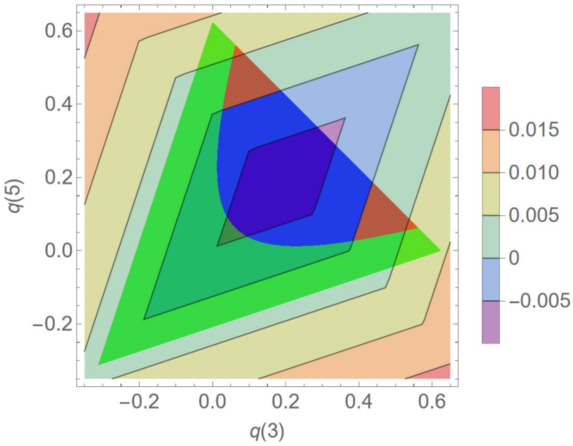

Figure 7.6.: Family K4. The result of $\mathscr{C}_{SIC}$ is represented by the rainbow spectrum. The red shapes show the regions in which the MUB witness detects bound entanglement.

7.2.2. Bipartite Ququint Systems

For $d = 5$ an exact fiducial vector can be found in [58, 59]. Unfortunately, the structure of this vector is rather complicated, which would make the computations down the stream extremely time consuming operations. For practical use, we reduce the entries of this vector to numerical values. The normalized version of the numerical fiducial vector is given by

$$|\psi_f\rangle = \begin{pmatrix} 0.391045 \\ -0.284866 - 0.647129i \\ -0.231884 - 0.198204i \\ 0.131939 - 0.109396i \\ 0.430967 + 0.197474i \end{pmatrix}. \tag{7.10}$$

By using $|\psi_f\rangle$ and equation (5.15) we obtain a complete set of SIC vectors that can be found in the appendix. For bipartite ququint states, the SIC criterion detects entanglement if

$$\mathscr{C}_{SIC} = \|\mathcal{P}\|_{Tr} - \frac{1}{15} > 0. \tag{7.11}$$

The results for family K5a and family K5b are shown in figure 7.7. In both state families $\mathscr{C}_{SIC}$ performs equally good in detecting free and bound entanglement. Compared to the results of the MUB witness, which are marked by the red shapes, $\mathscr{C}_{SIC}$ detects a larger area of bound entangled states. On the downside, $\mathscr{C}_{SIC}$ obtains a smaller region of free entangled states than the Peres-Horodecki criterion.

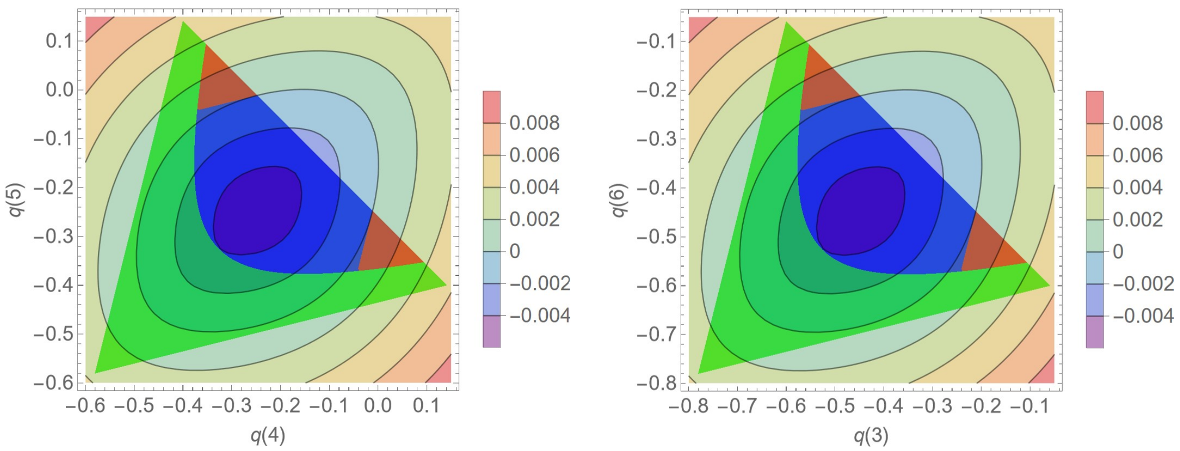

(a) Family K5a

(b) Family K5b

Figure 7.7.: The results of $\mathscr{C}_{SIC}$ are represented by the rainbow spectrum. The red shapes show the regions in which the MUB witness detects bound entanglement.

7.2.3. Bipartite Qusixt Systems

In $d = 6$ an exact fiducial vector is given in [58, 59]. Again, its structure is to complicated to perform the desired calculations in a reasonable amount of computation time. Reducing the vector's entries to numerical values fixes this problem. After normalization, the numerical fiducial vector results in

$$|\psi_f\rangle = \begin{pmatrix} 0.524447 \\ 0.025929 - 0.618186i \\ -0.128062 - 0.107276i \\ -0.360183 - 0.335003i \\ 0.0897671 - 0.00266531i \\ 0.180588 - 0.177725i \end{pmatrix}. \tag{7.12}$$

The SIC vectors that emerge from $|\psi_f\rangle$ are given in the appendix. For bipartite qusixts, the SIC criterion detects entanglement if

$$\mathscr{C}_{SIC} = \|\mathcal{P}\|_{Tr} - \frac{1}{21} > 0. \tag{7.13}$$

Figure 7.8 shows the results for family K6a and family K6b. Like before, $\mathscr{C}_{SIC}$ performs equally well for both state families, detecting free and bound entangled areas. Since for $d = 6$ a complete basis of MUBs has not been found, we compare the results of $\mathscr{C}_{SIC}$ with those of the generalized linear witness as given in equation (4.14). The bound entangled states obtained by this witness are marked by the red zones. We can see that $\mathscr{C}_{SIC}$ detects an even greater area of bound entangled states. However, as before, the SIC criterion obtains a smaller region of free entangled states than the Peres-Horodecki criterion.

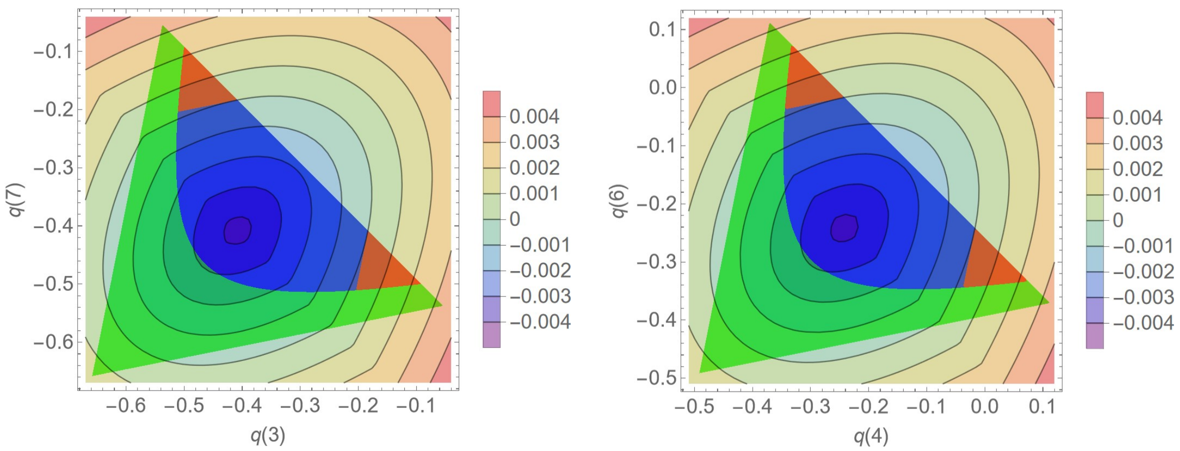

(a) Family K6a

(b) Family K6b

Figure 7.8.: The results of $\mathscr{C}_{SIC}$ are represented by the rainbow spectrum. The red shapes show the regions in which the generalized linear witness detects bound entanglement.

Overall, our calculations in this section point out a general advantage of $\mathscr{C}_{GSIC}$ and $\mathscr{C}_{SIC}$ over the MUB witness. In higher dimensions, complete sets of MUBs are extremely hard to find. Often it is not even clear, if a solution does exist. The lowest dimension for which a complete set of MUBs has not been obtained is $d = 6$. In cases like this, we still can use the generalized linear witness, but then again we cannot decompose this witness into experimentally feasible MUBs. In contrast, complete sets of numerical SIC-POVMs have been found for all $d \leq 151$ [17] and thus $\mathscr{C}_{SIC}$ is mathematically defined in these cases. Furthermore, this also enables potential experimental implementations of $\mathscr{C}_{SIC}$ in all these dimensions. For $\mathscr{C}_{GSIC}$, the situation in high dimensions is even more favorable, since in order to construct complete sets of GSIC-POVMs we only need generalized Gell-Mann matrices, which are defined in all finite dimensions.

8. Identifying Separable States in Bipartite Qutrits

In the previous chapter we successfully detected bound entanglement in several state families by using $\mathscr{C}_{GSIC}$ and $\mathscr{C}_{SIC}$. For the most part, the bound entangled areas obtained exceed those detected by the linear MUB witness. On the basis of these promising results, we wondered whether $\mathscr{C}_{GSIC}$ and $\mathscr{C}_{SIC}$ detect bound entanglement optimally for some state families. In the first two sections of this chapter, we will pursue this question for families B1, B2, and B3. Therefore, we will construct a family of separable two-qutrit states and draw our attention to states that border the bound entangled areas detected by $\mathscr{C}_{GSIC}$ and $\mathscr{C}_{SIC}$. The target will be to reconstruct these states by finding suitable parameterizations for the coefficients of the separable state family. In the last section of this chapter, we will view the task of identifying separable states as an optimization problem and apply this approach to families A1, B1, B2, and B3. Therefore we will again use the constructed family of separable states and expand its detection power by applying a group of symmetry transformations that conserve all entanglement properties in the magic simplex.

8.1. Construction of a Separable State Family

Let us consider the states of family B as defined in equation (6.16). In its matrix representation, they are given by

$$
\begin{aligned}
\rho_B &= \begin{pmatrix}
A & 0 & 0 & 0 & D & 0 & 0 & 0 & D \\
0 & B & 0 & 0 & 0 & 0 & 0 & 0 & 0 \\
0 & 0 & C & 0 & 0 & 0 & 0 & 0 & 0 \\
0 & 0 & 0 & C & 0 & 0 & 0 & 0 & 0 \\
D & 0 & 0 & 0 & A & 0 & 0 & 0 & D \\
0 & 0 & 0 & 0 & 0 & B & 0 & 0 & 0 \\
0 & 0 & 0 & 0 & 0 & 0 & B & 0 & 0 \\
0 & 0 & 0 & 0 & 0 & 0 & 0 & C & 0 \\
D & 0 & 0 & 0 & D & 0 & 0 & 0 & A
\end{pmatrix}, \\
A &= \frac{1}{90}(4\alpha + 5(\beta - 2(\gamma + \delta - 1))), \\
B &= \frac{1}{180}(-4\alpha - 5(\beta - 8\gamma + 4\delta - 4)), \\
C &= \frac{1}{180}(-4\alpha - 5(\beta + 4\gamma - 8\delta - 4)), \\
D &= \frac{1}{120}(8\alpha - 5\beta).
\end{aligned} \tag{8.1}
$$

A legitimate strategy to reconstruct separable states in this family is to use mixtures of line states. For $d = 3$ the 12 different line states are given by

$$\begin{aligned}
&\rho_{line1} = \frac{1}{3}\sum_{k=0}^{2} P_{0,k}, \quad \rho_{line2} = \frac{1}{3}\sum_{k=0}^{2} P_{1,k}, \quad \rho_{line3} = \frac{1}{3}\sum_{k=0}^{2} P_{2,k}, \\
&\rho_{line4} = \frac{1}{3}\sum_{k=0}^{2} P_{k,0}, \quad \rho_{line5} = \frac{1}{3}\sum_{k=0}^{2} P_{k,1}, \quad \rho_{line6} = \frac{1}{3}\sum_{k=0}^{2} P_{k,2}, \\
&\rho_{line7} = \frac{1}{3}\sum_{k=0}^{2} P_{k,k}, \quad \rho_{line8} = \frac{1}{3}\sum_{k=0}^{2} P_{k+1,k}, \quad \rho_{line9} = \frac{1}{3}\sum_{k=0}^{2} P_{k+2,k}, \\
&\rho_{line10} = \frac{1}{3}\sum_{k=0}^{2} P_{k,2k}, \quad \rho_{line11} = \frac{1}{3}\sum_{k=0}^{2} P_{k+1,2k}, \quad \rho_{line12} = \frac{1}{3}\sum_{k=0}^{2} P_{k+2,2k},
\end{aligned} \tag{8.2}$$

where modulus d is assumed. Taking all convex combinations of these line states leads to the kernel polytope $\mathcal{K}_3$ that is shown in [57] for families B1, B2, and B3 (as well as for family A1). Overall, $\mathcal{K}_3$ is successful in reconstructing separable states in substantial areas of these state families. However, it fails to cover most states bordering the bound entangled areas detected by $\mathscr{C}_{GSIC}$ and $\mathscr{C}_{SIC}$.

The limitations of $\mathcal{K}_3$ can be clearly illustrated in the case of family B3. Let us have a look at the matrix representation from equation (8.1). In family B3 the states bordering the bound entangled area either satisfy $C \leq D$ or $B \leq D$ or $B = C = D$. Unfortunately, the kernel polytope $\mathcal{K}_3$ cannot reproduce family B3 states with $C < D$ or $B < D$.

In order to reconstruct these states of interest, we have to assemble a separable state from scratch. Let us consider a set of 24 state vectors given by

$$\begin{aligned}
|\psi_a(1)\rangle &= \frac{1}{\sqrt{1+\mathcal{C}}}\begin{pmatrix} -1 \\ \sqrt{\mathcal{C}}e^{\frac{i\pi}{4}} \\ 0 \end{pmatrix}, \quad |\psi_b(1)\rangle = \frac{1}{\sqrt{1+\mathcal{C}}}\begin{pmatrix} \sqrt{\mathcal{C}}e^{\frac{i\pi}{4}} \\ -1 \\ 0 \end{pmatrix}, \\
|\psi_a(2)\rangle &= \frac{1}{\sqrt{1+\mathcal{C}}}\begin{pmatrix} -1 \\ \sqrt{\mathcal{C}}e^{-\frac{i\pi}{4}} \\ 0 \end{pmatrix}, \quad |\psi_b(2)\rangle = \frac{1}{\sqrt{1+\mathcal{C}}}\begin{pmatrix} \sqrt{\mathcal{C}}e^{-\frac{i\pi}{4}} \\ -1 \\ 0 \end{pmatrix}, \\
|\psi_a(3)\rangle &= \frac{1}{\sqrt{1+\mathcal{C}}}\begin{pmatrix} 1 \\ \sqrt{\mathcal{C}}e^{\frac{i\pi}{4}} \\ 0 \end{pmatrix}, \quad |\psi_b(3)\rangle = \frac{1}{\sqrt{1+\mathcal{C}}}\begin{pmatrix} \sqrt{\mathcal{C}}e^{\frac{i\pi}{4}} \\ 1 \\ 0 \end{pmatrix}, \\
|\psi_a(4)\rangle &= \frac{1}{\sqrt{1+\mathcal{C}}}\begin{pmatrix} 1 \\ \sqrt{\mathcal{C}}e^{-\frac{i\pi}{4}} \\ 0 \end{pmatrix}, \quad |\psi_b(4)\rangle = \frac{1}{\sqrt{1+\mathcal{C}}}\begin{pmatrix} \sqrt{\mathcal{C}}e^{-\frac{i\pi}{4}} \\ 1 \\ 0 \end{pmatrix},
\end{aligned} \tag{8.3}$$

$$|\psi_a(5)\rangle = \frac{1}{\sqrt{1+\mathcal{C}}}\begin{pmatrix}\sqrt{\mathcal{C}}e^{\frac{i\pi}{4}}\\0\\-1\end{pmatrix}, \quad |\psi_b(5)\rangle = \frac{1}{\sqrt{1+\mathcal{C}}}\begin{pmatrix}-1\\0\\\sqrt{\mathcal{C}}e^{\frac{i\pi}{4}}\end{pmatrix},$$

$$|\psi_a(6)\rangle = \frac{1}{\sqrt{1+\mathcal{C}}}\begin{pmatrix}\sqrt{\mathcal{C}}e^{-\frac{i\pi}{4}}\\0\\-1\end{pmatrix}, \quad |\psi_b(6)\rangle = \frac{1}{\sqrt{1+\mathcal{C}}}\begin{pmatrix}-1\\0\\\sqrt{\mathcal{C}}e^{-\frac{i\pi}{4}}\end{pmatrix},$$

$$|\psi_a(7)\rangle = \frac{1}{\sqrt{1+\mathcal{C}}}\begin{pmatrix}\sqrt{\mathcal{C}}e^{\frac{i\pi}{4}}\\0\\1\end{pmatrix}, \quad |\psi_b(7)\rangle = \frac{1}{\sqrt{1+\mathcal{C}}}\begin{pmatrix}1\\0\\\sqrt{\mathcal{C}}e^{\frac{i\pi}{4}}\end{pmatrix},$$

$$|\psi_a(8)\rangle = \frac{1}{\sqrt{1+\mathcal{C}}}\begin{pmatrix}\sqrt{\mathcal{C}}e^{-\frac{i\pi}{4}}\\0\\1\end{pmatrix}, \quad |\psi_b(8)\rangle = \frac{1}{\sqrt{1+\mathcal{C}}}\begin{pmatrix}1\\0\\\sqrt{\mathcal{C}}e^{-\frac{i\pi}{4}}\end{pmatrix},$$

$$|\psi_a(9)\rangle = \frac{1}{\sqrt{1+\mathcal{C}}}\begin{pmatrix}0\\-1\\\sqrt{\mathcal{C}}e^{\frac{i\pi}{4}}\end{pmatrix}, \quad |\psi_b(9)\rangle = \frac{1}{\sqrt{1+\mathcal{C}}}\begin{pmatrix}0\\\sqrt{\mathcal{C}}e^{\frac{i\pi}{4}}\\-1\end{pmatrix},$$

$$|\psi_a(10)\rangle = \frac{1}{\sqrt{1+\mathcal{C}}}\begin{pmatrix}0\\-1\\\sqrt{\mathcal{C}}e^{-\frac{i\pi}{4}}\end{pmatrix}, \quad |\psi_b(10)\rangle = \frac{1}{\sqrt{1+\mathcal{C}}}\begin{pmatrix}0\\\sqrt{\mathcal{C}}e^{-\frac{i\pi}{4}}\\-1\end{pmatrix},$$

$$|\psi_a(11)\rangle = \frac{1}{\sqrt{1+\mathcal{C}}}\begin{pmatrix}0\\1\\\sqrt{\mathcal{C}}e^{\frac{i\pi}{4}}\end{pmatrix}, \quad |\psi_b(11)\rangle = \frac{1}{\sqrt{1+\mathcal{C}}}\begin{pmatrix}0\\\sqrt{\mathcal{C}}e^{\frac{i\pi}{4}}\\1\end{pmatrix},$$

$$|\psi_a(12)\rangle = \frac{1}{\sqrt{1+\mathcal{C}}}\begin{pmatrix}0\\1\\\sqrt{\mathcal{C}}e^{-\frac{i\pi}{4}}\end{pmatrix}, \quad |\psi_b(12)\rangle = \frac{1}{\sqrt{1+\mathcal{C}}}\begin{pmatrix}0\\\sqrt{\mathcal{C}}e^{-\frac{i\pi}{4}}\\1\end{pmatrix}.$$

This set of vectors can be used to construct the separable state

$$\rho_s(\mathcal{C}) = \frac{1}{12}\sum_{i=1}^{12} |\psi_a(i)\rangle\langle\psi_a(i)| \otimes |\psi_b(i)\rangle\langle\psi_b(i)|. \tag{8.4}$$

To ensure that all eigenvalues of $\rho_s(\mathcal{C})$ are non-negative we have to set the parameter $\mathcal{C} \geq 0$. Our customized separable state family ρ_{sep} is then given by convex combinations of six line states and $\rho_s(\mathcal{C})$:

$$\rho_{sep} = \kappa_1\rho_{line1} + \kappa_4\rho_{line4} + \kappa_5\rho_{line5} + \kappa_6\rho_{line6} + \kappa_7\rho_{line7} + \kappa_{10}\rho_{line10} + \kappa_s\rho_s(\mathcal{C}), \tag{8.5}$$

where $0 \leq \kappa_i \leq 1$, $\sum_i \kappa_i = 1$, and $\mathcal{C} \geq 0$. Consequently, the matrix representation of this family of separable states can be written as

$$
\rho_{sep} = \begin{pmatrix}
A' & 0 & 0 & 0 & D' & 0 & 0 & 0 & D' \\
0 & B' & 0 & 0 & 0 & F' & E' & 0 & 0 \\
0 & 0 & C' & E' & 0 & 0 & 0 & F' & 0 \\
0 & 0 & F' & C' & 0 & 0 & 0 & E' & 0 \\
D' & 0 & 0 & 0 & A' & 0 & 0 & 0 & D' \\
0 & E' & 0 & 0 & 0 & B' & F' & 0 & 0 \\
0 & F' & 0 & 0 & 0 & E' & B' & 0 & 0 \\
0 & 0 & E' & F' & 0 & 0 & 0 & C' & 0 \\
D' & 0 & 0 & 0 & D' & 0 & 0 & 0 & A'
\end{pmatrix},
$$

$$
\begin{aligned}
A' &= \frac{1}{9}(\frac{6\mathcal{C}\kappa_s}{(1+\mathcal{C})^2} + \kappa_1 + 3\kappa_4 + \kappa_7 + \kappa_{10}), \\
B' &= \frac{1}{9}(\frac{3\kappa_s}{(1+\mathcal{C})^2} + \kappa_1 + 3\kappa_5 + \kappa_7 + \kappa_{10}), \\
C' &= \frac{1}{9}(\frac{3\mathcal{C}^2\kappa_s}{(1+\mathcal{C})^2} + \kappa_1 + 3\kappa_6 + \kappa_7 + \kappa_{10}), \\
D' &= \frac{1}{9}(\frac{3\mathcal{C}\kappa_s}{(1+\mathcal{C})^2} + \kappa_1 + \kappa_7 + \kappa_{10}), \\
E' &= \frac{1}{9}(\kappa_1 + e^{\frac{2i\pi}{3}}\kappa_7 - e^{\frac{i\pi}{3}}\kappa_{10}), \\
F' &= \frac{1}{9}(\kappa_1 - e^{\frac{i\pi}{3}}\kappa_7 + e^{\frac{2i\pi}{3}}\kappa_{10}).
\end{aligned} \tag{8.6}
$$

Let us now return to the family B3 states that border the detected bound entangled area. From equation (8.6) we can see that the freely selectable parameter $\mathcal{C} \geq 0$ opens up possibilities to construct states with $C' < D'$ or $B' < D'$.
In general, to reconstruct any state in family B we have to choose the state parameters from our separable family so that $\rho_{sep} = \rho_B$. Comparing the matrix representations of these two state families, the following five equations have to be satisfied:

$$
\begin{aligned}
\kappa_4 &= \frac{1}{30}(4\alpha + 5(\beta - 2(\gamma + \delta - 1))) - \frac{2\mathcal{C}\kappa_s}{(1+\mathcal{C})^2} - \kappa_1, \\
\kappa_5 &= \frac{1}{60}(-4\alpha - 5(\beta - 8\gamma + 4\delta - 4)) - \frac{\kappa_s}{(1+\mathcal{C})^2} - \kappa_1, \\
\kappa_6 &= \frac{1}{60}(-4\alpha - 5(\beta + 4\gamma - 8\delta - 4)) - \frac{\mathcal{C}^2\kappa_s}{(1+\mathcal{C})^2} - \kappa_1, \\
\kappa_7 &= \kappa_{10} = \kappa_1, \\
\kappa_s &= (\frac{3}{40}(8\alpha - 5\beta) - 3\kappa_1)\frac{(1+\mathcal{C})^2}{3\mathcal{C}}.
\end{aligned} \tag{8.7}
$$

8.2. Reconstructing Extremal Separable States

In this section we will take a closer look at the separability problem regarding the potentially separable states bordering the bound entangled areas in families B1, B2, and B3. These extremal states are located along lines for which $\mathscr{C}_{GSIC}$ and $\mathscr{C}_{SIC}$ returns the result zero. Consequently, we refer to these locations as zero lines. For all states along these zero lines, we make the assumption

$$\kappa_4 = \kappa_5 = \kappa_6 = 0. \tag{8.8}$$

Therefore, the remaining state coefficients of ρ_{sep} follow the relation $\kappa_s + 3\kappa_1 = 1$, where $0 \le \kappa_s \le 1$ and $0 \le \kappa_1 \le 1/3$. Furthermore, the conditions in equation (8.7) simplify to

$$\begin{aligned}
0 &= \frac{1}{30}(4\alpha + 5(\beta - 2(\gamma + \delta - 1))) - \frac{2\mathcal{C}\kappa_s}{(1+\mathcal{C})^2} - \kappa_1, \\
0 &= \frac{1}{60}(-4\alpha - 5(\beta - 8\gamma + 4\delta - 4)) - \frac{\kappa_s}{(1+\mathcal{C})^2} - \kappa_1, \\
0 &= \frac{1}{60}(-4\alpha - 5(\beta + 4\gamma - 8\delta - 4)) - \frac{\mathcal{C}^2\kappa_s}{(1+\mathcal{C})^2} - \kappa_1, \\
\kappa_7 &= \kappa_{10} = \kappa_1, \\
\kappa_s &= (\frac{3}{40}(8\alpha - 5\beta) - 3\kappa_1)\frac{(1+\mathcal{C})^2}{3\mathcal{C}}.
\end{aligned} \tag{8.9}$$

8.2.1. Family B1

In family B1 the zero line of $\mathscr{C}_{GSIC}$ and $\mathscr{C}_{SIC}$ is given by the equation

$$\begin{aligned}
&\beta = 0.32(-15 + 11\alpha - 5(\gamma + \delta) + \\
&\sqrt{100 - 180\alpha + 81\alpha^2 - 135\alpha(\gamma+\delta) + 150(\gamma + \gamma^2 + \delta - \frac{\gamma\delta}{2} + \delta^2)}),
\end{aligned} \tag{8.10}$$

where $\alpha \in [-0.492640, 0.0744303]$, $\gamma = -\frac{1}{\sqrt{3}}$, and $\delta = 0$. Figure 8.1a shows the location of the zero-line states marked by a white line. Substituting the expressions for β, γ, and δ into equation (8.9) leads to a simplified system of equations. Using only its second and third lines, we are able to obtain approximate solutions for $\mathcal{C}$ and κ_s as functions of α. The complete set of coefficients for the separably reconstructed zero-line states is given by

$$\begin{aligned}
\kappa_1 &= \kappa_7 = \kappa_{10} = 1.08932 - 1.2\alpha - 1.2\sqrt{0.782685 + (-1.25997 + \alpha)\alpha}, \\
\kappa_4 &= \kappa_5 = \kappa_6 = 0, \\
\kappa_s &= 1 - 3\kappa_1, \\
\mathcal{C} &= \frac{1.283 + \sqrt{0.782685 + (-1.25997 + \alpha)\alpha}}{0.492640 + \alpha}.
\end{aligned} \tag{8.11}$$

Figures 8.1b–8.1d depict the graphs of κ_1, κ_s, and $\mathcal{C}$. It should be noted that the parameter $\mathcal{C}$ has a pole exactly at the lower bound of alpha. However, in the interval $I_1 = (-0.492640, 0.0744303]$, all coefficients are described by continuous functions. Calculating the extreme values of the state coefficients as well as the extreme values of their sum confirms that for $\alpha \in I_1$ all constraints are met to constitute mathematically well defined states:

$$\begin{aligned}
&\min_{\forall\alpha\in I_1} \kappa_1 = 8.88178 \cdot 10^{-16}, \quad \max_{\forall\alpha\in I_1} \kappa_1 = 0.140883,\\
&\min_{\forall\alpha\in I_1} \kappa_s = 0.577350, \quad \max_{\forall\alpha\in I_1} \kappa_s = 1 - 2.66454 \cdot 10^{-15},\\
&\min_{\forall\alpha\in I_1} \sum_i \kappa_i = \max_{\forall\alpha\in I_1} \sum_i \kappa_i = 1, \quad i = \{1,4,5,6,7,10,s\},\\
&\min_{\forall\alpha\in I_1} \mathcal{C} = 3.73205, \quad \max_{\forall\alpha\in I_1} \mathcal{C} \to \infty.
\end{aligned} \tag{8.12}$$

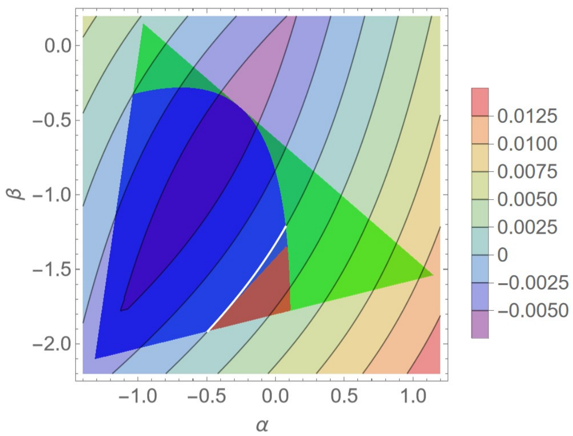

(a) Family B1

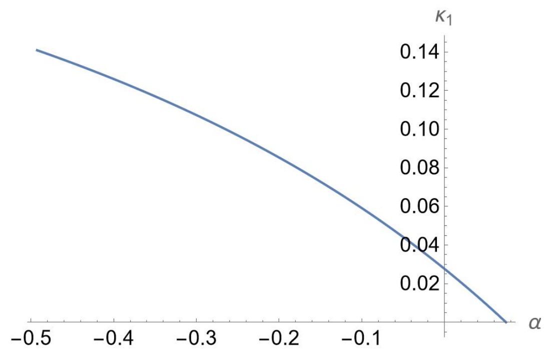

(b) κ_1 as a function of $\alpha \in I_1$.

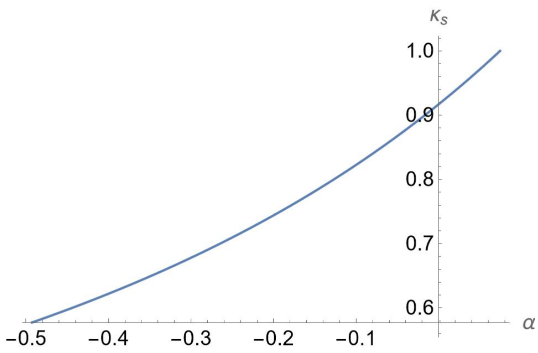

(c) κ_s as a function of $\alpha \in I_1$.

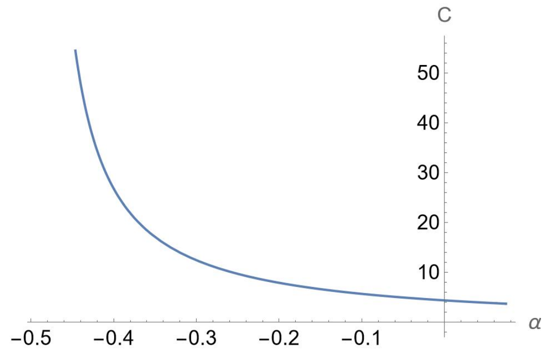

(d) $\mathcal{C}$ as a function of $\alpha \in I_1$.

Figure 8.1.: In (a) the zero-line states of family B1 are marked by the white line. (b)–(d) show the coefficients of the separably reconstructed states along the zero line.

To check whether our reconstructed separable states correspond to the B1 family states along the zero line, we calculate the fidelity. The results are depicted in figure 8.2. The fidelity F fluctuates almost everywhere along the zero line around 1 with deviations smaller than $5 \cdot 10^{-14}$. Only at the lower border of I_1 does the fidelity drop to 0.99999986, which still corresponds to a very good agreement between the reconstructed states and the zero-line states. Therefore, we conclude that in this region the states along the zero-line are separable. Consequently, $\mathscr{C}_{GSIC}$ and $\mathscr{C}_{SIC}$ optimally detect bound entanglement in family B1.

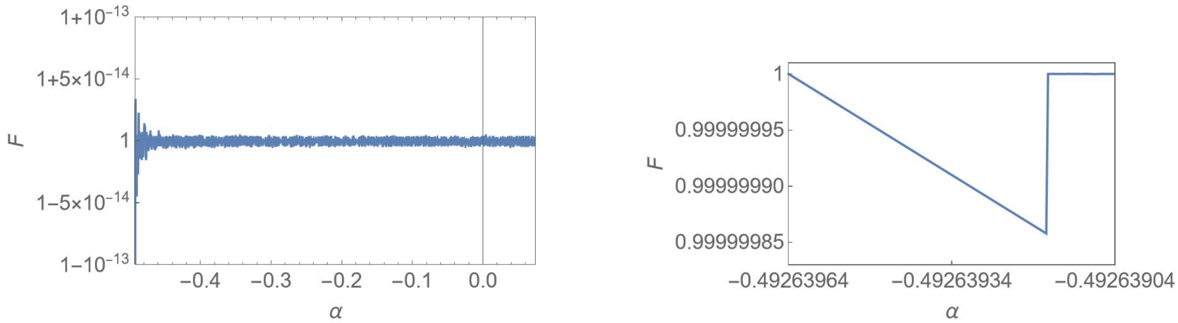

(a) Fidelity as a function of $\alpha \in I_1$.

(b) Fidelity close to the lower endpoint of I_1.

Figure 8.2.: (a) and (b) describe the closeness between the zero-line states of family B1 and the reconstructed separable states.

8.2.2. Family B2

For family B2 the zero-line states are shown in figure 8.3a. Their general shape can also be described by equation (8.10), but here $\alpha \in [-1.19444, -0.876875]$, $\gamma = -0.83$, and $\delta = 0$. With these specifications, we use the third and fifth lines of equation (8.7) to obtain approximate solutions for κ_1 and $\mathcal{C}$. The complete set of coefficients for the separably reconstructed zero-line states is given by

$$
\begin{aligned}
\kappa_1 = \kappa_7 = \kappa_{10} &= \frac{-0.624093 - 0.61\alpha + 0.0566667\sqrt{0.973272 + (-0.838889 + \alpha)\alpha}}{0.65 - \alpha + \sqrt{0.973272 + (-0.838889 + \alpha)\alpha}}, \\
\kappa_4 = \kappa_5 = \kappa_6 &= 0, \\
\kappa_s &= 1 - 3\kappa_1, \\
\mathcal{C} &= \frac{1.84444 + \sqrt{0.973272 + (-0.838889 + \alpha)\alpha}}{1.19444 + \alpha}.
\end{aligned}
\tag{8.13}
$$

The equation for $\mathcal{C}$ has a pole at $\alpha = -1.19444$. Consequently, we have to slightly adjust the value range of α to $I_2 = (-1.19444, -0.876875]$. In this interval all coefficients are given by continuous functions. The graphs of κ_1, κ_s, and $\mathcal{C}$ are shown in figures 8.3b–8.3d. Their extreme values and the extreme values of the summed state coefficients are given by

$$\begin{aligned}
&\min_{\forall\alpha\in I_2} \kappa_1 = -9.84566 \cdot 10^{-17}, \quad \max_{\forall\alpha\in I_2} \kappa_1 = 0.0566667, \\
&\min_{\forall\alpha\in I_2} \kappa_s = 0.83, \quad \max_{\forall\alpha\in I_2} \kappa_s = 1 + 2.95370 \cdot 10^{-16}, \\
&\min_{\forall\alpha\in I_2} \sum_i \kappa_i = \max_{\forall\alpha\in I_2} \sum_i \kappa_i = 1, \quad i = \{1,4,5,6,7,10,s\}, \\
&\min_{\forall\alpha\in I_2} \mathcal{C} = 10.7647, \quad \max_{\forall\alpha\in I_2} \mathcal{C} \to \infty.
\end{aligned} \tag{8.14}$$

The minimum of κ_1 is slightly negative, and the maximum of κ_s is marginally greater than one. Technically, this contradicts the constraints imposed on the state coefficients. However, the deviations are so small that we can disregard them as insignificant numerical discrepancies. We can conclude that the coefficients give rise to well defined separable states.

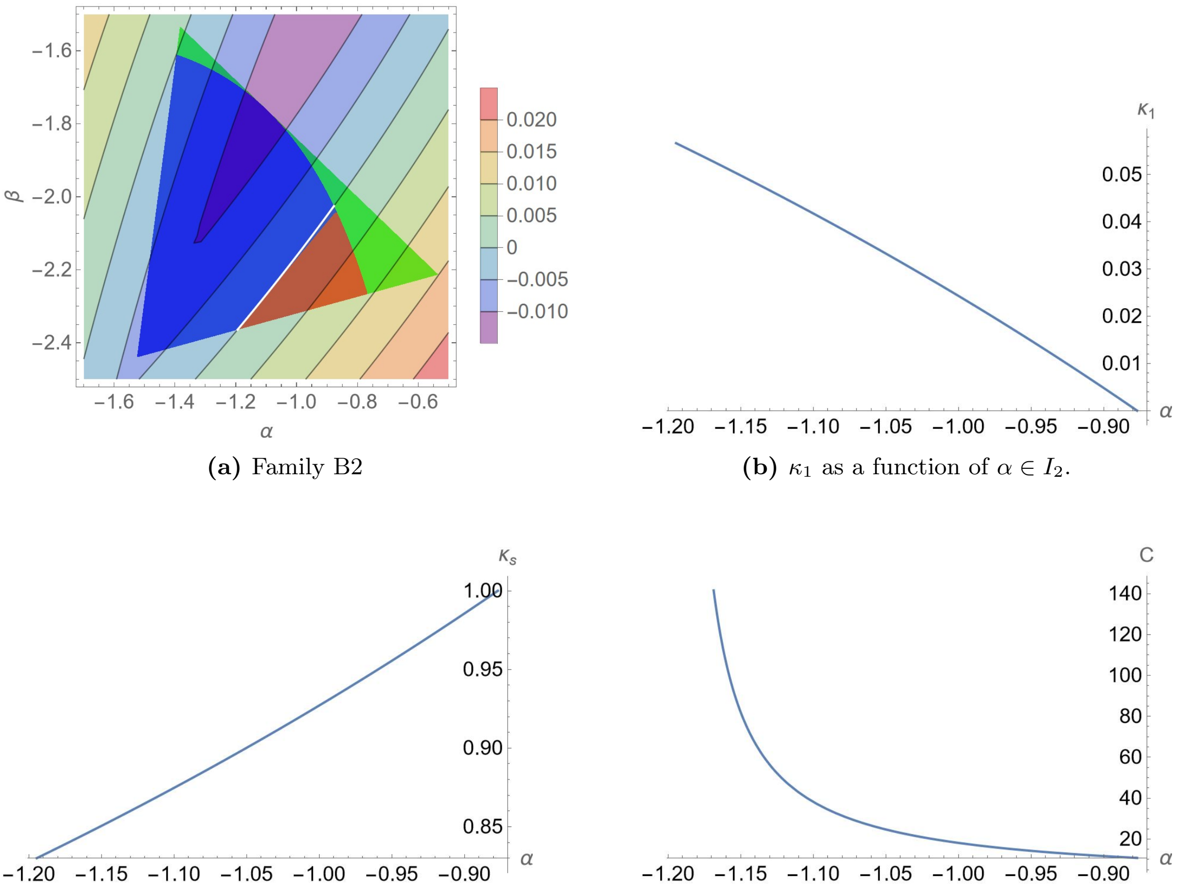

(a) Family B2

(b) κ_1 as a function of $\alpha \in I_2$.

(c) κ_s as a function of $\alpha \in I_2$.

(d) $\mathcal{C}$ as a function of $\alpha \in I_2$.

Figure 8.3.: In (a) the zero-line states of family B2 are marked by the white line. (b)–(d) show the coefficients of the separably reconstructed states along the zero line.

The fidelity between the family B2 states along the zero line and the reconstructed separable states is shown in figure 8.2. Again, it is fluctuating minimally around one. Only very close to the lower end of I_2 does the fidelity drop to 0.99999982, which we still rate as high enough to reasonably claim that the separable reconstruction was successful in the whole interval. Therefore, we conclude that $\mathscr{C}_{GSIC}$ and $\mathscr{C}_{SIC}$ also detect bound entanglement optimally in family B2.

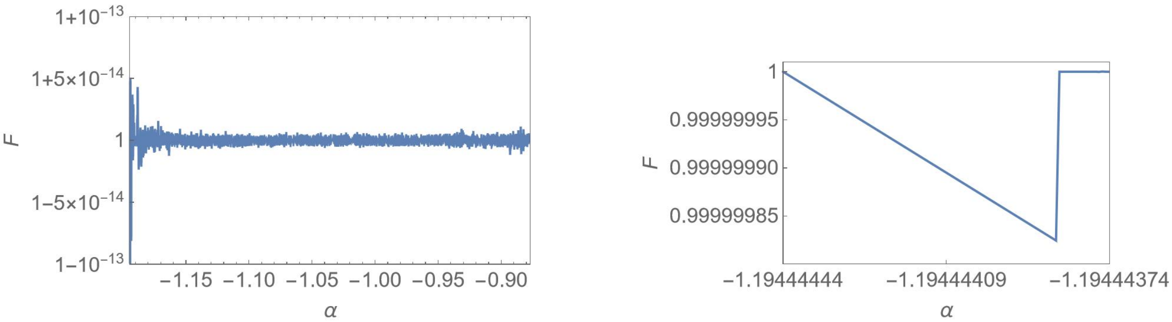

(a) Fidelity as a function of $\alpha \in I_2$. **(b)** Fidelity close to the lower endpoint of I_2.

Figure 8.4.: (a) and (b) describe the closeness between the zero-line states of family B2 and the reconstructed separable states.

8.2.3. Family B3

In family B3 the zero line of $\mathscr{C}_{GSIC}$ and $\mathscr{C}_{SIC}$ is given by the equation

$$\delta_{\pm} = \frac{\alpha}{10} + \frac{\beta}{8} + \frac{\gamma}{2} \pm \frac{\sqrt{800 + 264\alpha^2 + 600\beta + 75\beta^2 + 300\beta\gamma - 600\gamma^2 + \alpha(-960 - 420\beta + 240\gamma)}}{20\sqrt{2}}, \tag{8.15}$$

where $\alpha = \frac{5}{3}(-1 + \sqrt{3})$ and $\beta = -\frac{1}{10}$. The plus-minus symbol indicates that we have to make a case distinction.

Case 1: "δ_+"

For $\gamma \in [\frac{1}{120}(197 - 117\sqrt{3}), 0.219017]$ the equation of δ_+ describes the upper part of the zero line as pictured in figure 8.5a. We use the relations for α, β, and δ_+ as well as the first, third, and fifth line of equation (8.7) to find approximate solutions for $\mathcal{C}$ and κ_1. The reconstructed separable states for this segment of the zero line are given by the coefficients

$$\begin{aligned}
&\kappa_1 = \kappa_7 = \kappa_{10} = 0.0701921 + 0.5\gamma + 0.0117851\sqrt{13.7044 + 262.82\gamma - 600\gamma^2},\\
&\kappa_4 = \kappa_5 = \kappa_6 = 0,\\
&\kappa_s = 1 - 3\kappa_1,\\
&\mathcal{C} = \frac{-2.51873 + 7.55618\kappa_1 - 0.0514133\sqrt{164.453 + 3153.84\gamma - 7200\gamma^2}}{-1.93829 + 7.55618\kappa_1}.
\end{aligned} \tag{8.16}$$

Substituting the expression for κ_1 into the equation for $\mathcal{C}$, we can see that $\mathcal{C}$ has a pole at $\gamma = 0.219017$. The interval in which all coefficients are described by continuous functions that give rise to well-defined separable states is given by $I_{3+} = [\frac{1}{120}(197 - 117\sqrt{3}), 0.219017)$. Figures 8.5b–8.5d show the graphs of κ_1, κ_s, and $\mathcal{C}$ as functions of $\gamma \in I_{3+}$. Their extreme values and the extreme values of the summed state coefficients are given by

$$
\begin{aligned}
&\min_{\forall\gamma\in I_{3+}} \kappa_1 = 0.0466717, \qquad \max_{\forall\gamma\in I_{3+}} \kappa_1 = 0.256517, \\
&\min_{\forall\gamma\in I_{3+}} \kappa_s = 0.230449, \qquad \max_{\forall\gamma\in I_{3+}} \kappa_s = 0.859985, \\
&\min_{\forall\gamma\in I_{3+}} \sum_i \kappa_i = \max_{\forall\gamma\in I_{3+}} \sum_i \kappa_i = 1, \quad i = \{1,4,5,6,7,10,s\}, \\
&\min_{\forall\gamma\in I_{3+}} \mathcal{C} = 1.36626, \qquad \max_{\forall\gamma\in I_{3+}} \mathcal{C} \to \infty.
\end{aligned}
\tag{8.17}
$$

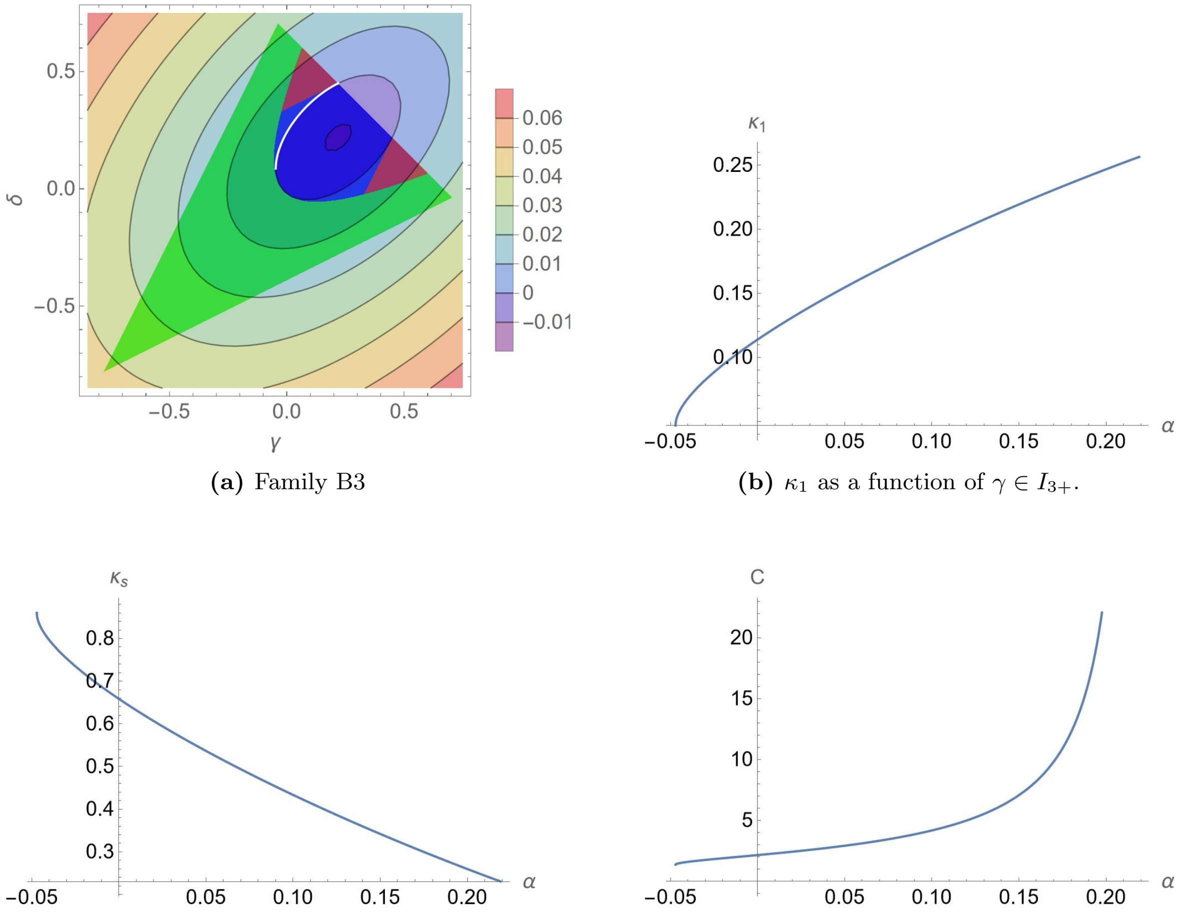

(a) Family B3

(b) κ_1 as a function of $\gamma \in I_{3+}$.

(c) κ_s as a function of $\gamma \in I_{3+}$.

(d) $\mathcal{C}$ as a function of $\gamma \in I_{3+}$.

Figure 8.5.: In (a) the zero-line states of family B3 corresponding to δ_+ are marked by the white line. (b)–(d) show the coefficients of the separably reconstructed states along this segment of the zero line.

The fidelity between the family B3 states corresponding to δ_+ and the reconstructed separable states is depicted in figure 8.6. The biggest drop of fidelity can be witnessed near the upper border of I_{3+}, where its minimal value is given by $F = 0.99999985$. Overall, the results show that the states correspond to each other with high precision. Therefore, we conclude that all states along this part of the zero line are separable.

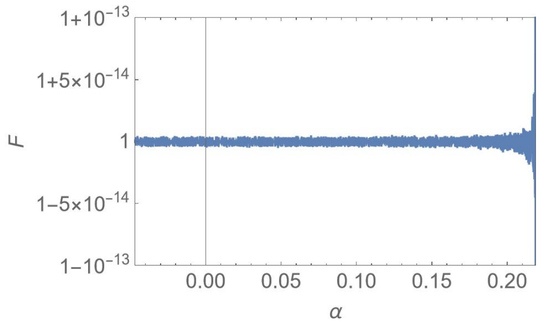

(a) Fidelity as a function of $\gamma \in I_{3+}$.

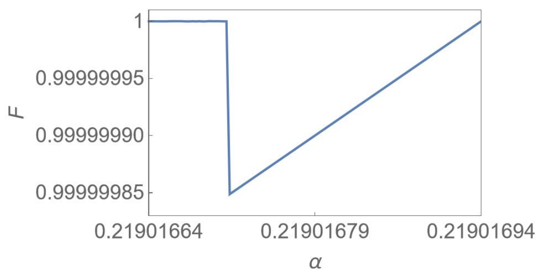

(b) Fidelity close to the upper endpoint of I_{3+}.

Figure 8.6.: (a) and (b) describe the closeness between the zero-line states of family B3 corresponding to δ_+ and the reconstructed separable states.

Case 2: "δ_-"

δ_- describes the lower part of the zero-line for $\gamma \in I_{3-} = [\frac{1}{120}(197 - 117\sqrt{3}), 0.449466]$ as pictured in figure 8.7a. Using the definitions of α and β given for family B3 as well as the relation for δ_-, we find approximate solutions for $\mathcal{C}$ and κ_1 by comparing the first, second and fifth line of equation (8.7). Along this segment of the zero-line the coefficients for the reconstructed separable states are given by

$$\begin{aligned}
&\kappa_1 = \kappa_7 = \kappa_{10} = 0.0701921 + 0.5\gamma - 0.00340207\sqrt{164.453 + (3153.84 - 7200\gamma)\gamma},\\
&\kappa_4 = \kappa_5 = \kappa_6 = 0,\\
&\kappa_s = 1 - 3\kappa_1,\\
&\mathcal{C} = \frac{27.3841 - 73.4847\gamma + 0.5\sqrt{164.453 + (3153.84 - 7200\gamma)\gamma}}{22.5793 + \sqrt{164.453 + (3153.84 - 7200\gamma)\gamma}}.
\end{aligned} \tag{8.18}$$

All coefficients correspond to continuous functions in the interval I_{3-}. The graphs of κ_1, κ_s, and $\mathcal{C}$ are shown in the figures 8.7b–8.7d. From their extreme values and the extreme values of the summed up state coefficients we can see that the coefficients give rise to well defined states for all $\gamma \in I_{3-}$:

$$\begin{aligned}
&\min_{\forall\gamma\in I_{3-}} \kappa_1 = 0.0260677, \quad \max_{\forall\gamma\in I_{3-}} \kappa_1 = 0.256517,\\
&\min_{\forall\gamma\in I_{3-}} \kappa_s = 0.230449, \quad \max_{\forall\gamma\in I_{3-}} \kappa_s = 0.921797,\\
&\min_{\forall\gamma\in I_{3+}} \sum_i \kappa_i = \max_{\forall\gamma\in I_{3+}} \sum_i \kappa_i = 1, \quad i = \{1,4,5,6,7,10,s\},
\end{aligned} \tag{8.19}$$

$$\min_{\forall\gamma\in I_{3-}} \mathcal{C} = 4.33935 \cdot 10^{-9}, \quad \max_{\forall\gamma\in I_{3-}} \mathcal{C} = 1.36603.$$

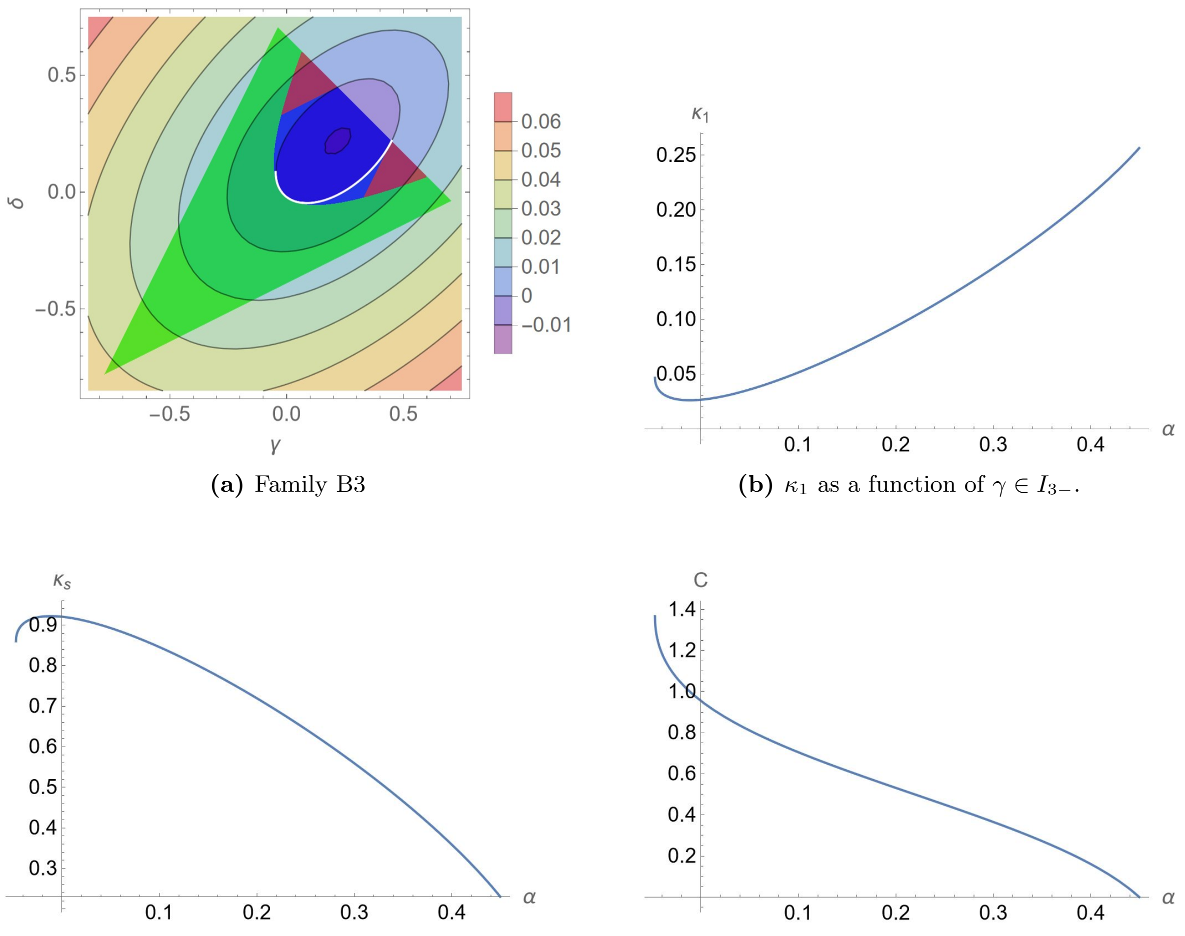

(a) Family B3

(b) κ_1 as a function of $\gamma \in I_{3-}$.

(c) κ_s as a function of $\gamma \in I_{3-}$.

(d) $\mathcal{C}$ as a function of $\gamma \in I_{3-}$.

Figure 8.7.: In (a) the zero-line states of family B3 corresponding to δ_- are marked by the white line. (b)–(d) show the coefficients of the separably reconstructed states along this segment of the zero line.

Figure 8.8 shows the fidelity between the states of family B3 corresponding to δ_- and the separably reconstructed states. Overall the results indicate that the states are practically identical. For the most part, the fidelity fluctuates insignificantly around 1. Only very close to the lower end of I_{3-} it drops to 0.99999985. However, even this minimal value indicates a very good agreement between the compared states. Therefore, we conclude that the separable reconstruction of the zero-line states corresponding to δ_- was successful.

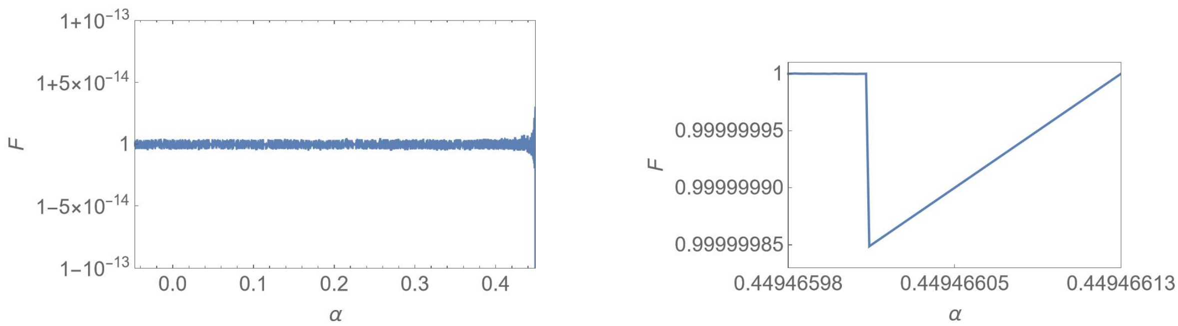

(a) Fidelity as a function of $\gamma \in I_{3-}$. **(b)** Fidelity close to the upper endpoint of I_{3-}.

Figure 8.8.: (a) and (b) describe the closeness between the zero-line states of family B3 corresponding to δ_- and the reconstructed separable states.

Case 1 & 2 Combined

Combining the segments of the zero line corresponding to δ_+ and δ_- gives all zero-line states in family B3. In figure 8.9 they are marked by a white line. We established that for both segments of the zero line the reconstructed separable states match with the regarding family B3 states. Therefore, all states on the zero line must be separable. Since every state in the convex hull of the zero line must also be separable, there are no more regions left that were not determined as either separable or bound entangled or free entangled. We conclude that $\mathscr{C}_{GSIC}$ and $\mathscr{C}_{SIC}$ detect all entangled states in family B3. Furthermore, this means that we have completely solved the separability problem for family B3.

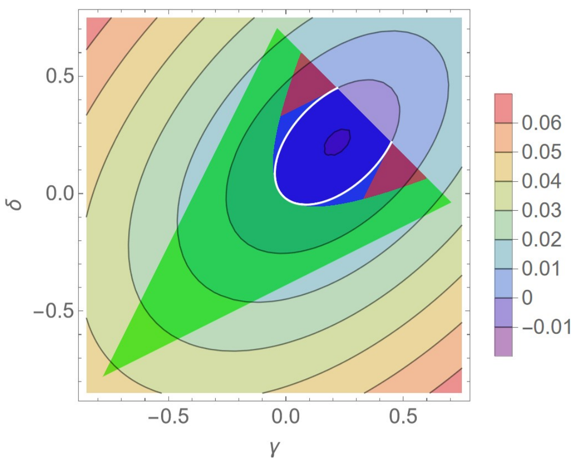

Figure 8.9.: The white line marks all zero-line states in family B3.

8.3. Identifying Separable States via Constrained Optimization

Let us consider ρ_{sep} as defined in equation (8.4). This family of separable states lies completely in the magic simplex, since it can be decomposed into a basis of bell projection operators

P_{kl}. Therefore, the symmetry transformations that conserve the entanglement class in the magic simplex also have the same effect on ρ_{sep}. Applying n such transformations separately to our family of separable states gives rise to the separable states $\rho_{sep,i}$, where $i = 1, 2, ..., n$. Depending on the composition of the seed state, some of the generated states can be duplicates. Also note that $i = 1$ corresponds to the trivial transformation, which leaves the initial state unchanged, i.e. $\rho_{sep} = \rho_{sep,1}$. Consequently, ρ_{sep} is extended to a separable polytope with up to n vertices. A state ρ is confirmed to be separable, if

$$\sum_{i=1}^{n} p_i \rho_{sep,i} = \rho, \tag{8.20}$$

where $0 \leq p_i \leq 1$ and $\sum p_i = 1$. In the magic simplex, the spectral decomposition of ρ can be written in terms of the Bell projection operators $P_{k,l}$ and their associated probabilities $\lambda_{k,l}$, which are also the eigenvalues of the state. In the case of bipartite qutrit states, defining $\vec{P} = (P_{0,0}, P_{0,1}, ..., P_{2,2})^T$ and $\vec{\lambda} = (\lambda_{0,0}, \lambda_{0,1}, ..., \lambda_{2,2})^T$ simplifies the notation to

$$\rho = \sum_{k,l=0}^{d-1} \lambda_{k,l} P_{k,l} = \vec{\lambda} \cdot \vec{P} \tag{8.21}$$

Since the transformed states $\rho_{sep,i}$ still lie in the magic simplex, we can write

$$\sum_{i=1}^{n} p_i \rho_{sep,i} - \rho = \sum_{i=1}^{n} p_i \vec{\lambda}_{sep,i} \cdot \vec{P} - \vec{\lambda} \cdot \vec{P} = 0. \tag{8.22}$$

Consequently, the matrix problem in equation (8.20) is reduced to the vector equation

$$\sum_{i=1}^{n} p_i \vec{\lambda}_{sep,i} = \vec{\lambda}. \tag{8.23}$$

For the special case of magic-simplex states, the expression obtained is a sufficient separability criterion. We can implement this vector problem by using constraint optimization.

8.3.1. Implementation for $n = 1$

ρ_{sep} alone is already a state family that can be used to potentially identify a range of separable states. To examine this case, we set $n = 1$. Therefore, equation (8.23) simplifies to

$$\vec{\lambda}_{sep} = \vec{\lambda}. \tag{8.24}$$

To implement this problem through constraint optimization, our strategy is to minimize

$$|\lambda_{0,0,sep} - \lambda_{0,0}|, \tag{8.25}$$

while using

$$\lambda_{0,1,sep} = \lambda_{0,1}, \quad \lambda_{0,2,sep} = \lambda_{0,2}, \quad ..., \quad \lambda_{2,2,sep} = \lambda_{2,2} \tag{8.26}$$

as well as $\mathcal{C} \geq 0$, $0 \leq \kappa_i \leq 1$, and $\sum \kappa_i = 1$ as constraints. If the minimization routine returns the result

$$\min |\lambda_{0,0,sep} - \lambda_{0,0}| < 10^{-10}, \tag{8.27}$$

then the state is numerically verified as separable. During the calculation process, two further simplifications turned out to be very useful. Firstly, setting

$$\kappa_1 = \kappa_7 = \kappa_{10} \tag{8.28}$$

does not harm the detection power of the separable state in the examined families A1, B1, B2, and B3, but the optimization problem converges much faster and better. In this case, the constraints $0 \leq \kappa_7 \leq 1$ and $0 \leq \kappa_{10} \leq 1$ can be left out, while the constrains involving κ_1 change to $0 \leq \kappa_1 \leq 1/3$ and $3\kappa_1 + \kappa_4 + \kappa_5 + \kappa_6 + \kappa_s = 1$. Secondly, for the zero-line states in family B1, B2, and B3, the most accurate results can be obtained by additionally setting the coefficients

$$\kappa_4 = \kappa_5 = \kappa_6 = 0. \tag{8.29}$$

Therefore, we can leave out the constraints $0 \leq \kappa_4 \leq 1$, $0 \leq \kappa_5 \leq 1$, $0 \leq \kappa_6 \leq 1$, and $0 \leq \kappa_s \leq 1$, while the condition for the sum of the state coefficients reduces to $3\kappa_1 + \kappa_s = 1$.
Let us apply the implementation for $n = 1$ to the state families A1, B1, B2, and B3. The results are shown in figure 8.10. The detected areas of separable states are enclosed by white contours.
For family A1, we only find separable states for $\alpha \in [0, 1/4]$ and $\beta = 0$. This straight line, as shown in figure 8.10a, belongs to the family of isotropic states $I(\alpha)$ [60]. For two-qutrit states, the isotropic family is separable in the interval $\alpha \in [-1/8, 1/4]$. Therefore, our calculations successfully replicate the upper border of this interval, but do not detect separable states for $\alpha < 0$.
In families B1 and B2, we detect substantial areas of separable states, as shown in figures 8.10b–8.10c. This includes even the separable states on the zero lines. However, both separable areas do not reach the upper left zone of the PPT states. Instead, the limit of each area is a diagonal line given by the equation

$$\beta = \frac{8}{5}\alpha, \tag{8.30}$$

where $\alpha \in [-\frac{5}{18}(3+\sqrt{3}), -\frac{5}{9}(-3+2\sqrt{3})]$ for family B1 and $\alpha \in [-1.525, -1.1]$ for family B2. This border describes a break in the symmetry of both state families. To show this, let us consider the matrix representation of family B given in equation (8.1). Substituting equation (8.30) into this expression results in diagonal state matrices with $D = 0$. Analyzing the separable areas obtained in families B1 and B2 uncovers that our implementation only detects separable states with $D \geq 0$. However, the potentially separable states in the upper left part of the PPT zone have $D < 0$. We conclude that our separable state family ρ_{sep} cannot reconstruct states with this symmetry.

The results for family B3 are shown in figure 8.10d. Our implementation detects that the entire area in question is separable.

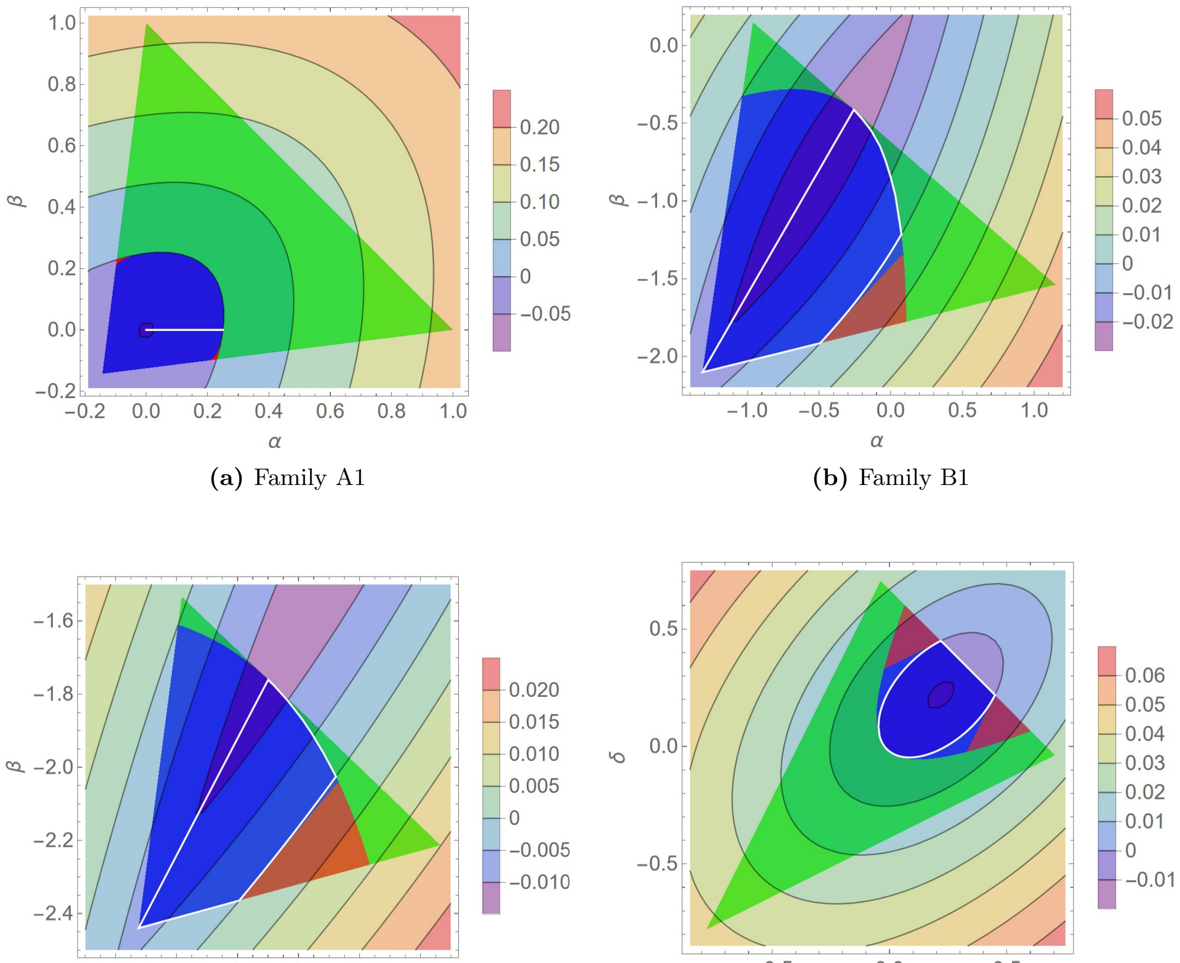

(a) Family A1

(b) Family B1

(c) Family B2

(d) Family B3

Figure 8.10.: The separable areas detected for $n = 1$ are enclosed by white contours.

8.3.2. Implementation for $n = 72$

The most general version of our family of separable states has a rather complicated structure that made the implementation for $n = 1$ already a computationally expensive calculation. In order to handle the minimization problem for a mixture of $n > 1$ separable states, we have to drastically reduce the number of state coefficients. Therefore, we employ the same approach that we used to verify the zero-line states in the case of $n = 1$. Consider ρ_{sep} with the assumptions from equations (8.28) and (8.29). Consequently, the constraints of ρ_{sep} reduce to $0 \leq \kappa_1 \leq 1/3$, $3\kappa_1 + \kappa_s = 1$, and $\mathcal{C} \geq 0$. Applying the symmetry transformations of the magic simplex to this simplified family of separable states gives rise to $n = 72$ non-repetitive separable states. Taking all these states into account, equation (8.23) evolves to

$$\sum_{i=1}^{72} p_i \vec{\lambda}_{sep,i} = \vec{\lambda}. \tag{8.31}$$

We can implement this equation through constraint optimization by minimizing

$$|\sum_{i=1}^{n} p_i \lambda_{0,0,sep,i} - \lambda_{0,0}|, \tag{8.32}$$

while using

$$\sum_{i=1}^{n} p_i \lambda_{0,1,sep,i} = \lambda_{0,1}, \quad \sum_{i=1}^{n} p_i \lambda_{0,2,sep,i} = \lambda_{0,2}, \quad ..., \quad \sum_{i=1}^{n} p_i \lambda_{2,2,sep,i} = \lambda_{2,2} \tag{8.33}$$

as well as $0 \leq p_i \leq 1$, $\sum p_i = 1$, $0 \leq \kappa_1 \leq 1/3$, and $\mathcal{C} \geq 0$ as constraints. Again, a state is numerically verified as separable if the minimization routine returns

$$\min |\sum_{i=1}^{72} p_i \lambda_{0,0,sep,i} - \lambda_{0,0}| < 10^{-10}. \tag{8.34}$$

However, the last two constraints involving κ_1 and $\mathcal{C}$ slow down the computation to the extent that it is not practical to apply this criterion to a large number of test states. To ease up the computation complexity, we transform this non-linear optimization problem into several simplified optimization problems by taking these two constraints out of the minimization routine and instead vary the values of κ_1 and $\mathcal{C}$ via Do-loops. This is possible because any arbitrary combination of $0 \leq \kappa_1 \leq 1/3$ and $\mathcal{C} \geq 0$ gives rise to well-defined states. It turned out that this strategy still leads to useful results if the configurations of the Do-loops are chosen cleverly. In our calculations we use the following setups for Do-loops:

- Configuration 1:

$$\kappa_1 = \frac{a}{30}, \quad a = 0, 1, 2, ..., 10 \quad \text{and} \quad \mathcal{C} = \frac{b}{10}, \quad b = 0, 1, 2, ..., 10. \tag{8.35}$$

- Configuration 2:

$$\kappa_1 = \frac{a}{30}, \quad a = 0, 1, 2, ..., 10 \quad \text{and} \quad \mathcal{C} = e^{b/10} - 1, \quad b = 0, 1, 2, ..., 25. \tag{8.36}$$

- Configuration 3:

$$\kappa_1 = \frac{a}{30}, \quad a = 0, 1, 2, ..., 10 \quad \text{and} \quad \mathcal{C} = e^{b^2/40} - 1, \quad b = 0, 1, 2, ..., 25. \tag{8.37}$$

Let us apply these implementations to the state families A1, B1, B2, and B3. The separable states detected are marked in figures 8.11–8.14 by enclosing white contours. Each group of figures shows the results of one state family for the three different looping configurations, as well as the result for the combined configurations.

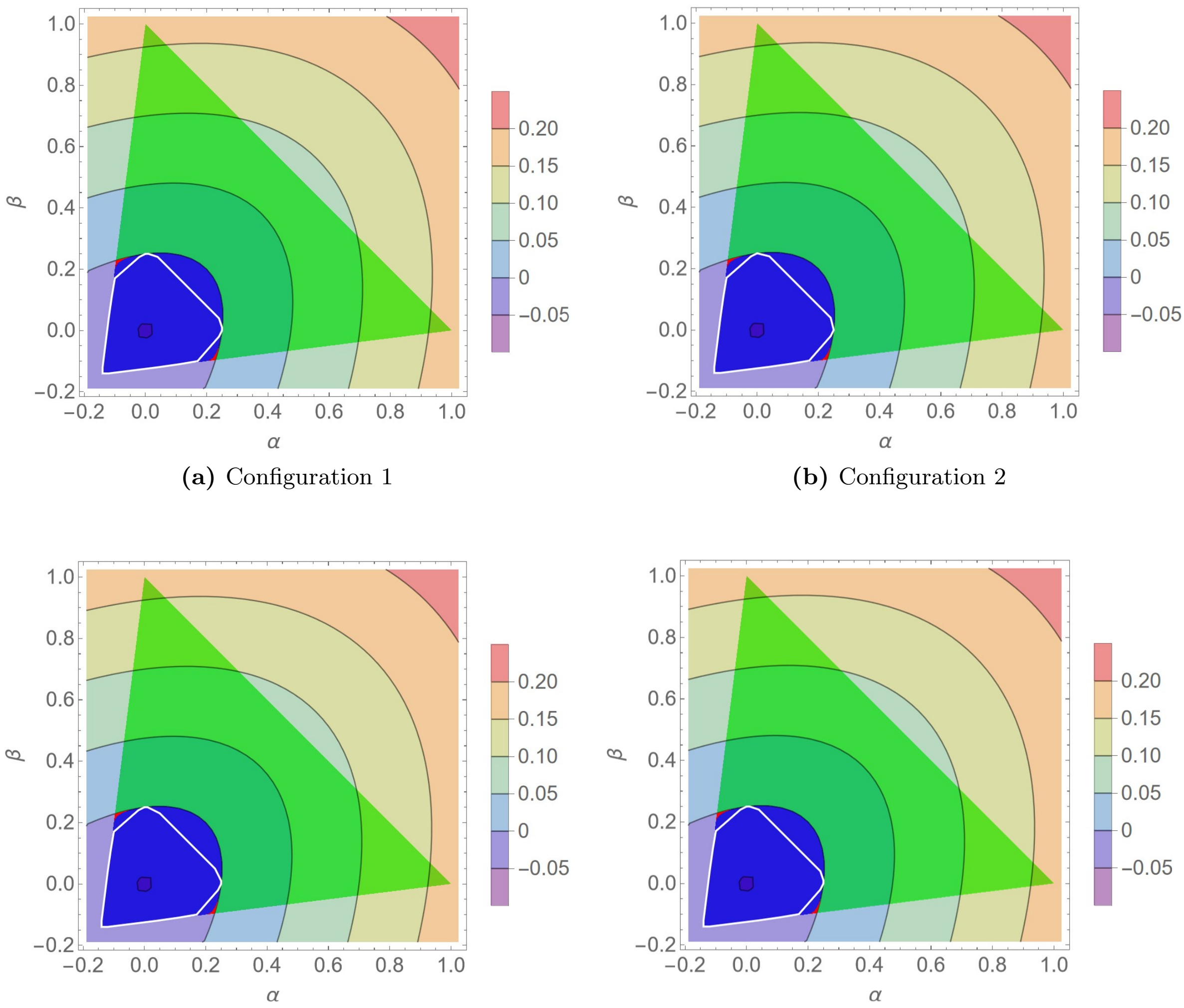

(a) Configuration 1

(b) Configuration 2

(c) Configuration 3

(d) Configurations 1–3 combined

Figure 8.11.: For $n = 72$ the configurations 1–3 were applied to family A1. The separable areas detected are enclosed by white contours.

The outcomes for family A1 are shown in figure 8.11. There is hardly any difference in the separable areas obtained between the different looping configurations. Thus, combining these results barely expands the separable area detected. However, all configurations confirm that large portions of the PPT area are separable. At two places the separable areas even reach the zero line of $\mathscr{C}_{GSIC}$ and $\mathscr{C}_{SIC}$.

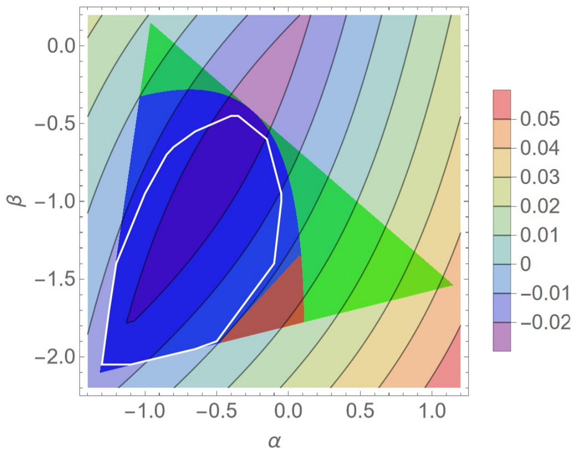

(a) Configuration 1

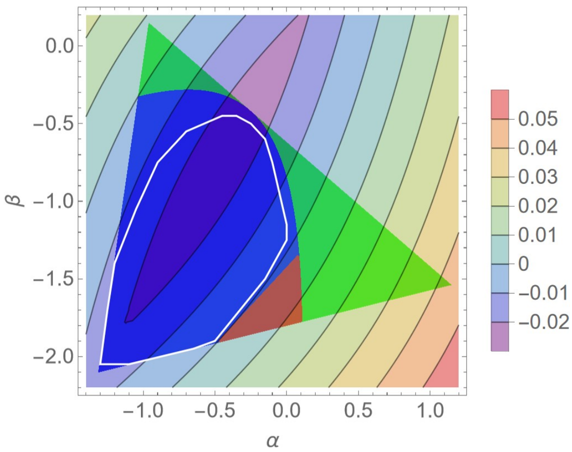

(b) Configuration 2

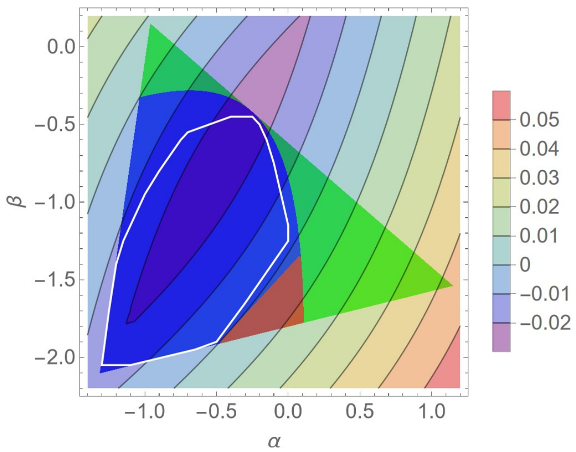

(c) Configuration 3

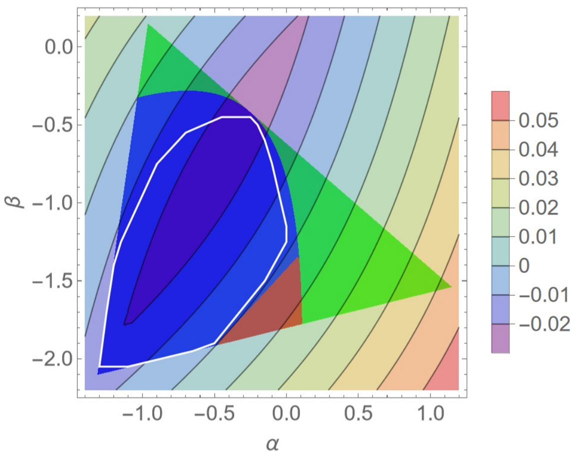

(d) Configurations 1–3 combined

Figure 8.12.: For $n = 72$ the configurations 1–3 were applied to family B1. The separable areas detected are enclosed by white contours.

Figure 8.12 shows the results for family B1. Previously, we established that in this state family our implementation for $n = 1$ does not detect separable states with $D < 0$. Clearly, our three configurations for $n = 72$ overcome this symmetry break. On the downside, they cannot confirm the separability of the zero-line states. The best results for the separable states near the zero line of $\mathscr{C}_{GSIC}$ and $\mathscr{C}_{SIC}$ are found using configuration 2, while configuration 3 is more successful in the upper right part of the PPT area. In contrast, configuration 1 does not outperform configuration 2 anywhere in family B1. Still, combining the results of all three configurations leads to a noticeably extended separable area.

The outcomes for family B2 are shown in figure 8.13. Also for this state family we established that the implementation for $n = 1$ does not detect separable states with $D < 0$. Again, our implementations for $n = 72$ detect separable states beyond this symmetry break. However, the separable areas obtained for each configuration differ significantly. Configuration 1 detects the smallest area. Especially for the separable states near the zero line of $\mathscr{C}_{GSIC}$ and $\mathscr{C}_{SIC}$ it performs poorly. A noticeable extended separable area is obtained using configuration 2. This setup is able to identify separable states much closer to the zero line. However, the best results are obtained for configuration 3. In family B2 there exists no region where configurations 1 or 2 detect separable states that are not already detected by configuration 3. Therefore, combining the results of all three configurations leads to the identical separable area as for configuration 3.

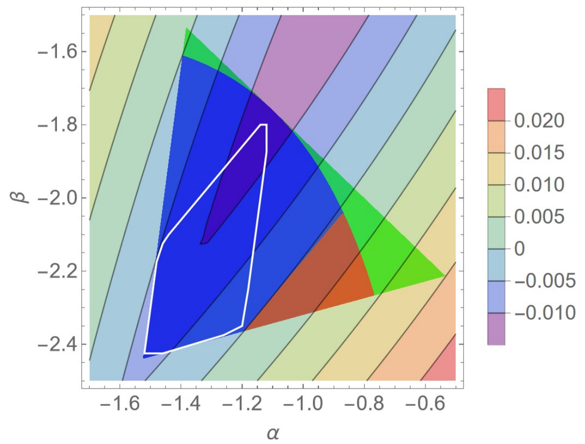

(a) Configuration 1

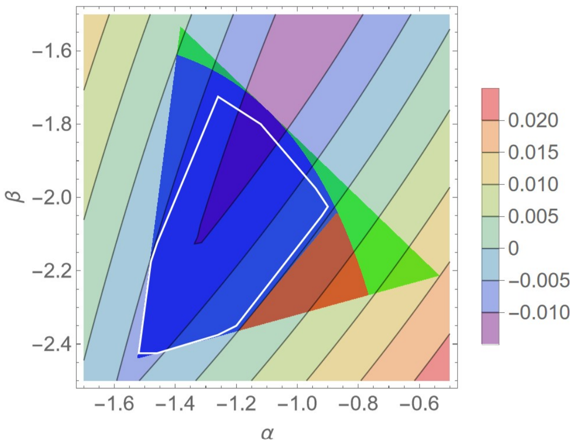

(b) Configuration 2

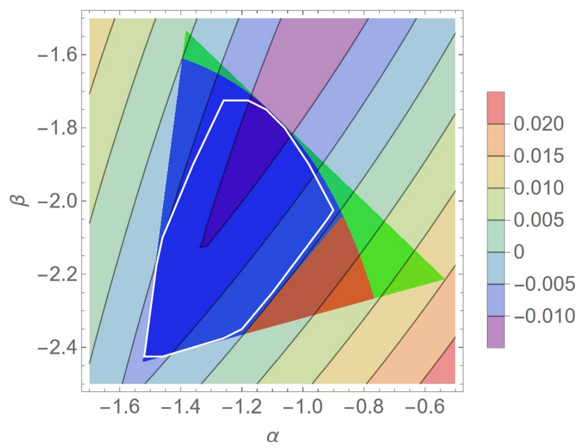

(c) Configuration 3

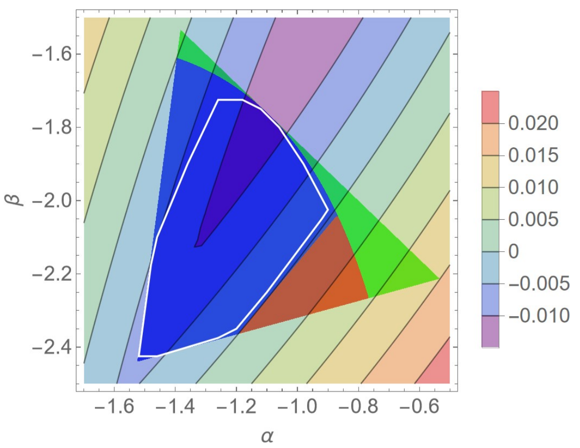

(d) Configurations 1–3 combined

Figure 8.13.: For $n = 72$ the configurations 1–3 were applied to family B2. The separable areas detected are enclosed by white contours.

For family B3 the results are shown in figure 8.14. In contrast to the implementation for $n = 1$ neither of the configurations detects all separable states, but all three configurations identify a large majority of separable states. Between configuration 1 and 2 there are areas in which the respective other preforms better. On the other hand, configuration 3 identifies only separable areas that have already been detected by configuration 2. Therefore, only configurations 1 and 2 contribute to the improved detection when combining all setups for $n = 72$.

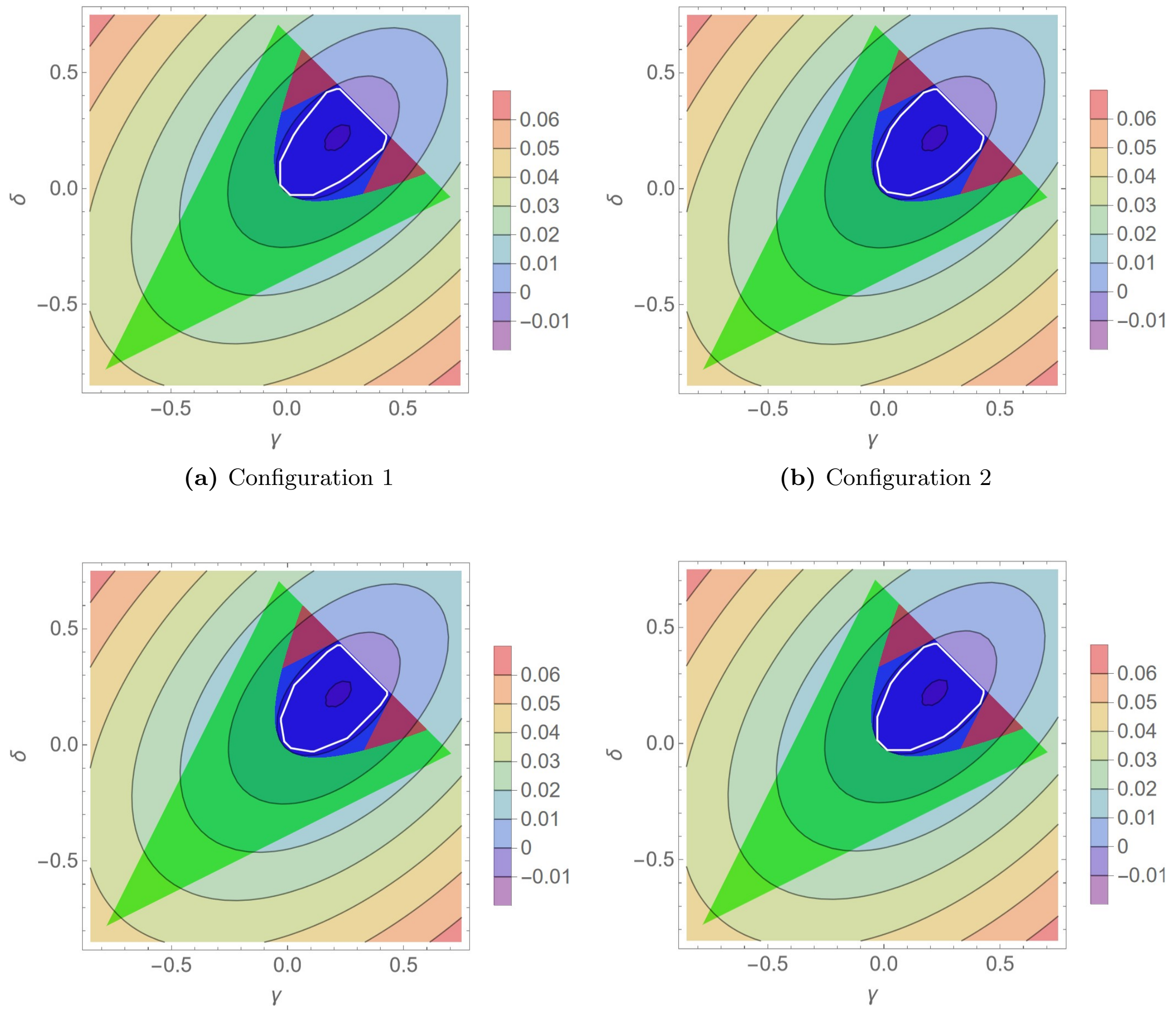

(a) Configuration 1

(b) Configuration 2

(c) Configuration 3

(d) Configurations 1–3 combined

Figure 8.14.: For $n = 72$ the configurations 1–3 were applied to family B3. The separable areas detected are enclosed by white contours.

8.3.3. Combined Results

Figure 8.15 shows the total separable areas obtained for families A1, B1, B2, and B3 combining the implementations for $n = 1$ and $n = 72$. The sufficient separability criterion for $n = 1$ proved to be very successful for the zero-line states, while the implementations for

$n = 72$ overcame certain symmetry breaks. In principle, the sufficient separability criterion for $n = 72$ would also be able to identify all separable states on the zero lines for families B1, B2, and B3, if we could include the parameters κ_1 and $\mathcal{C}$ into the minimization routine. Practically, this is not feasible for a large area of separable states because it would drastically increase the computational complexity and, therefore, also the computation time.

For family A1, the combined results are identical to the separable area detected by the implementations for $n = 72$, while for family B3 we already obtained all separable states using the criterion for $n = 1$. Conversely, combining the implementations for $n = 1$ and $n = 72$ expands the separable areas of families B1 and B2. Despite detecting large regions of separable states in families A1, B1, and B2, we are unable to fully solve the separability problem in these families.

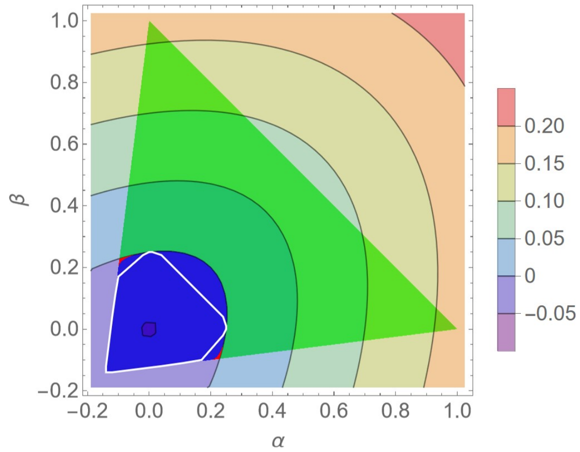

(a) Family A1

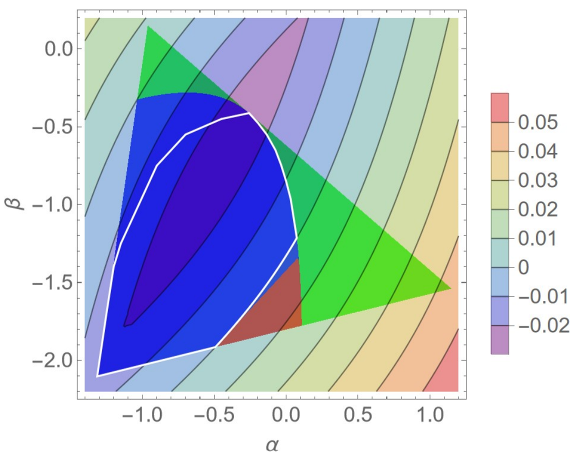

(b) Family B1

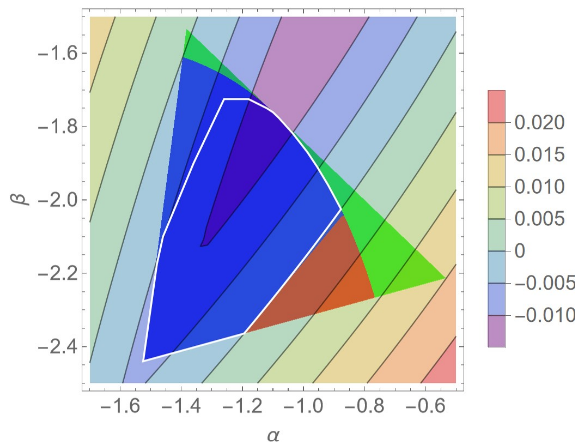

(c) Family B2

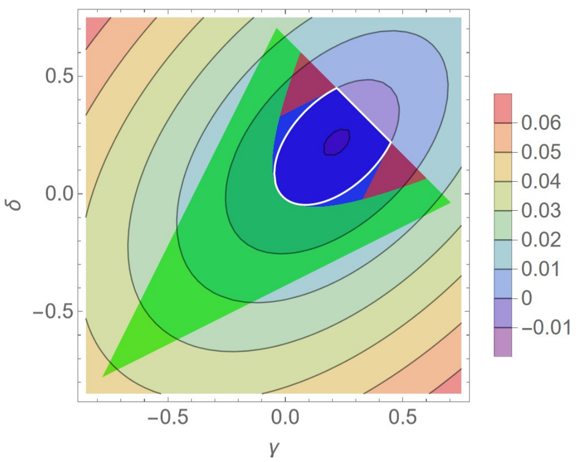

(d) Family B3

Figure 8.15.: Results of $n = 1$ and $n = 72$ combined. The separable areas detected are enclosed by white contours.

9. Summary & Conclusions

During this thesis, we examined separability problems of selected state families within the magic simplex, a mathematical object defined by convex combinations of Bell projection operators. Generally, bipartite systems with overall dimension $d > 6$ can contain entangled states that remain positive under partial transposition and therefore fail to be detected by the Peres-Horodecki criterion [4]. To unveil such bound entangled states, we focused on the necessary separability criteria $\mathscr{C}_{GSIC}$ [13] and $\mathscr{C}_{SIC}$ [16], which use GSIC-POVMs and SIC-POVMs, respectively. For comparison, we often applied an entanglement witness composed of MUBs, the so-called MUB witness [8]. GSIC-POVMs, SIC-POVMs, and MUBs alike share the prospect of experimental feasibility. However, the first two types of measurements are especially interesting for the purpose of entanglement detection, since they can be constructed in a wider range of dimensions than complete sets of MUBs. For the detection of separable states, we assembled a family of separable states in the magic simplex and further expanded it by means of entanglement-class-conserving symmetries [20]. The task was then to show that the states in question are part of this family.

The search for bound entanglement was carried out in several bipartite state families of dimensions 3×3, 4×4, 5×5, and 6×6. Overall, $\mathscr{C}_{GSIC}$ and $\mathscr{C}_{SIC}$ obtained bound entangled areas in all but one of the tested state families. Even more, they always detected the exact same bound entangled and free entangled areas. This further underlines the close relationship between GSIC-POVMs and SIC-POVMs. In nearly all examined state families $\mathscr{C}_{GSIC}$ and $\mathscr{C}_{SIC}$ turned out to be more successful than the MUB witness. Only in the examined 4×4 state family $\mathscr{C}_{GSIC}$, $\mathscr{C}_{SIC}$, and the MUB witness obtained the same area of bound entangled states. Since there has not been found a complete set of MUBs in dimension $d = 6$, we rather applied the generalized linear witness [9] to the 6×6 state families. This entanglement witness can be viewed as an extension of the MUB witness for arbitrary dimensions, which unfortunately cannot, in general, guarantee a simple experimental implementation. In the tested families of 6×6 states, the MUB witness detected a smaller area of bound entanglement than $\mathscr{C}_{GSIC}$ and $\mathscr{C}_{SIC}$.

The most detailed analysis was provided for 3×3 systems. Here, we examined four state families denoted by A1, B1, B2, and B3. In the case of family A1, $\mathscr{C}_{GSIC}$, $\mathscr{C}_{SIC}$, and the MUB witness did not detect any bound entanglement. However, the results of the quasi-pure concurrence [21] confirmed the existence of bound entangled states in this family. In all other investigated 3×3 state families $\mathscr{C}_{GSIC}$, $\mathscr{C}_{SIC}$, and the MUB witness obtained substantial areas of bound entangled states. Again, the former two criteria clearly outperformed the latter one. Nevertheless, the MUB witness showed an extraordinary property. It still detected a small area of bound entanglement in family B2, if one mutually unbiased basis was left out of the witness. We proceeded to explore, what happens if one element of the GSIC-POVM or the

SIC-POVM is left out of $\mathscr{C}_{GSIC}$ or $\mathscr{C}_{SIC}$, respectively. Unfortunately, these adapted criteria did not detect any bound entanglement in the examined state families, but they produced slightly varying results in terms of the obtained free entangled areas. In detail, both types of adapted criteria detected free entangled states in family A, but only those utilizing incomplete SIC-POVMs obtained free entangled areas in families B1 and B3.

The construction of a separable state family ρ_{sep} in the 3×3-dimensional magic simplex was carried out by mixing several line states and a customized separable state. We then proceeded to compare the density matrices of ρ_{sep} and family B. The latter contains, among other things, the state families B1, B2, and B3. From this comparison, we extracted several equations that relate the coefficients of ρ_{sep} and family B to each other. Making further assumptions, we found suitable parameterizations for the state coefficients of ρ_{sep} that allowed us to reconstruct the states bordering the bound entangled areas in families B1, B2, and B3 as detected by $\mathscr{C}_{GSIC}$ and $\mathscr{C}_{SIC}$. As a result, we can confirm that all states satisfying the Peres-Horodecki criterion along these bound entangled areas must be separable. Therefore, $\mathscr{C}_{GSIC}$ and $\mathscr{C}_{SIC}$ both detect bound entanglement optimally in these families. For family B3, the described approach even led to a complete solution of the separability problem.

Applying n entanglement-class-conserving symmetries to ρ_{sep} gave rise to an extended separable state family $\sum_{i=1}^{n} p_i \rho_{sep,i}$. Since this family still lies completely within the magic simplex, we could expand it into a basis of Bell projection operators. The resulting representation of $\sum_{i=1}^{n} p_i \rho_{sep,i}$ enabled us to reformulate the task of identifying separable states in the magic simplex as a vector equation that was implemented as a non-linear optimization problem with constraints. In the trivial case of $n = 1$, $p_1 = 1$, and $\rho_{sep,1} = \rho_{sep}$, we successfully confirmed our previous results and even extended the detected area of separable states in families B1 and B2. Furthermore, we were able to also detect some separable states in family A1. For $n = 72$, the computation complexity of the resulting optimization problem forced us to tighten the restrictions on the values of multiple state coefficients. These measures eventually transformed the identification of separable states into several simplified optimization problems. As a result, we were able to extend the detected separable areas in some regions of families A1, B1, and B2. However, the additional restrictions negatively influenced our ability to detect extremal separable states bordering the bound entangled areas.

Regarding the detection of bound entanglement, our results show a clear advantage of $\mathscr{C}_{GSIC}$ and $\mathscr{C}_{SIC}$ over the MUB witness in the investigated state families. This can partly be explained by the fact that the MUB witness is linear, while the other two criteria have a non-linear structure. Therefore, it would be interesting to explore whether MUBs can also be used to construct a similar non-linear necessary separability criterion. Nevertheless, the advantage of $\mathscr{C}_{GSIC}$ and $\mathscr{C}_{SIC}$ would remain in dimensions where complete sets of MUBs have not been found. Another task of further research could be to compare $\mathscr{C}_{GSIC}$ and $\mathscr{C}_{SIC}$ more in depth. For complete sets GSIC-POVMs and SIC-POVMs, we always obtained the same entangled areas. This is not entirely unexpected because of the close relationship between GSIC-POVMs and SIC-POVMs. After all, the definition of GSIC-POVMs even contains SIC-POVMs as a special case, and $\mathscr{C}_{GSIC}$ can be viewed as a generalized version of $\mathscr{C}_{SIC}$. However, the construction of GSIC-POVMs used does not satisfy the properties of SIC-POVMs. The question therefore arises whether there exist entangled states that can be detected by either $\mathscr{C}_{GSIC}$ or $\mathscr{C}_{SIC}$, but not by both. At least in the case of the utilized incomplete GSIC-POVMs and SIC-POVMs, the resulting necessary separability criteria showed this behavior. Finally, our schemes for detecting separable states through constraint optimization may be improved, if we remove some of the self-imposed restrictions from the regarding implementations. However, this would significantly increase the computation complexity and may require a modified optimization algorithm that can deal with larger numbers of parameters and constraints.

References

[1] M. A. Nielsen. Cluster-state quantum computation. *Reports on Mathematical Physics*, 57(1):147–161, 2006.

[2] D. Bouwmeester, J.-W. Pan, K. Mattle, M. Eibl, H. Weinfurter, and A. Zeilinger. Experimental quantum teleportation. *Nature*, 390:575–579, 1997.

[3] A. K. Ekert. Quantum cryptography based on bell's theorem. *Phys. Rev. Lett.*, 67:661–663, 1991.

[4] A. Peres. Separability criterion for density matrices. *Phys. Rev. Lett.*, 77:1413–1415, 1996.

[5] M. Horodecki, P. Horodecki, and R. Horodecki. Separability of mixed states: necessary and sufficient conditions. *Physics Letters A*, 223(1):1–8, 1996.

[6] M. Horodecki, P. Horodecki, and R. Horodecki. Mixed-state entanglement and distillation: Is there a "bound" entanglement in nature? *Phys. Rev. Lett.*, 80:5239–5242, 1998.

[7] J. Schwinger. Unitary operator bases*. *Proceedings of the National Academy of Sciences*, 46(4):570–579, 1960.

[8] C. Spengler, M. Huber, S. Brierley, T. Adaktylos, and B. C. Hiesmayr. Entanglement detection via mutually unbiased bases. *Phys. Rev. A*, 86:022311, 2012.

[9] E. Kilian. Bound entanglement detection via mutually unbiased bases. *Master's thesis, University of Vienna*, 2018.

[10] I. D. Ivonovic. Geometrical description of quantal state determination. *Journal of Physics A: Mathematical and General*, 14(12):3241, 1981.

[11] W. K. Wootters and B. D. Fields. Optimal state-determination by mutually unbiased measurements. *Annals of Physics*, 191(2):363–381, 1989.

[12] D. M. Appleby. Symmetric informationally complete measurements of arbitrary rank. *Optics and Spectroscopy*, 103:416–428, 2007.

[13] L.-M. Lai, T. Li, S.-M. Fei, and Z.-X. Wang. Entanglement criterion via general symmetric informationally complete measurements. *Quantum Information Processing*, 17:314, 2018.

[14] G. Zauner. Quantendesigns – Grundzüge einer nichtkommutativen Designtheorie. *PhD thesis, University of Vienna*, 1999.

[15] J. M. Renes, R. Blume-Kohout, A. J. Scott, and C. M. Caves. Symmetric informationally complete quantum measurements. *Journal of Mathematical Physics*, 45(6):2171–2180, 2004.

[16] J. Shang, A. Asadian, H. Zhu, and O. Gühne. Enhanced entanglement criterion via symmetric informationally complete measurements. *Phys. Rev. A*, 98:022309, 2018.

[17] C. A. Fuchs, M. C. Hoang, and B. C. Stacey. The sic question: History and state of play. *Axioms*, 6(21), 2017.

[18] G. Gour and A. Kalev. Construction of all general symmetric informationally complete measurements. *Journal of Physics A: Mathematical and Theoretical*, 47(33):335302, 2014.

[19] B. Baumgartner, B. Hiesmayr, and H. Narnhofer. A special simplex in the state space for entangled qudits. *Journal of Physics A: Mathematical and Theoretical*, 40(28):7919, 2007.

[20] C. Popp and B. Hiesmayr. Almost complete solution for the np-hard separability problem of bell diagonal qutrits. *Scientific Reports*, 12:12472, 2022.

[21] J. Bae, M. Tiersch, S. Sauer, F. de Melo, F. Mintert, B. Hiesmayr, and A. Buchleitner. Detection and typicality of bound entangled states. *Phys. Rev. A*, 80:022317, 2009.

[22] F. Bloch. Nuclear induction. *Phys. Rev.*, 70(7–8):460–474, 1946.

[23] M. Nielsen and I. Chuang. *Quantum Computation and Quantum Information.* Cambridge University Press, 1st edition, 2000.

[24] R. A. Bertlmann and P. Krammer. Bloch vectors for qudits. *arXiv:0806.1174 [quant-ph]*, 2008.

[25] M. Gell-Mann. Symmetries of baryons and mesons. *Phys. Rev.*, 125(3):1067–1084, 1962.

[26] C. H. Bennett, G. Brassard, C. Crépeau, R. Jozsa, A. Peres, and W. K. Wootters. Teleporting an unknown quantum state via dual classical and einstein-podolsky-rosen channels. *Phys. Rev. Lett.*, 70:1895–1899, 1993.

[27] R. Jozsa. Fidelity for mixed quantum states. *Journal of Modern Optics*, 41(12):2315–2323, 1994.

[28] L. P. Hughston, R. Jozsa, and W. K. Wootters. A complete classification of quantum ensembles having a given density matrix. *Physics Letters A*, 183(1):14–18, 1993.

[29] A. Uhlmann. The “transition probability” in the state space of a *-algebra. *Reports on Mathematical Physics*, 9(2):273–279, 1976.

[30] A. Ekert and P. Knight. Entangled quantum systems and the schmidt decomposition. *American Journal of Physics*, 63:415, 1995.

[31] E. Størmer. Positive linear maps of operator algebras. *Acta Mathematica*, 110:233–278, 1963.

[32] S. L. Woronowicz. Positive maps of low dimensional matrix algebras. *Reports on Mathematical Physics*, 10:165–183, 1976.

[33] C. H. Bennett, G. Brassard, S. Popescu, B. Schumacher, J. A. Smolin, and W. K. Wootters. Purification of noisy entanglement and faithful teleportation via noisy channels. *Phys. Rev. Lett.*, 76:722–725, 1996.

[34] S. Banach. Sur les fonctionnelles linéaires. *Studia Mathematica*, 1:211–216, 1929.

[35] R. T. Rockafellar. *Convex Analysis.* Princeton University Press, 1st edition, 1970.

[36] B. M. Terhal. Bell inequalities and the separability criterion. *Physics Letters A*, 271(5):319–326, 2000.

[37] M. Lewenstein, B. Kraus, J. I. Cirac, and P. Horodecki. Optimization of entanglement witnesses. *Phys. Rev. A*, 62:052310, 2000.

[38] N. BOHR. The quantum postulate and the recent development of atomic theory. *Nature*, 121:580–590, 1928.

[39] C. Spengler, M. Huber, S. Brierley, T. Adaktylos, and B. C. Hiesmayr. Entanglement detection via mutually unbiased bases. *Phys. Rev. A*, 86:022311, 2012.

[40] S. Bandyopadhyay, P. O. Boykin, V. Roychowdhury, and F. Vatan. A new proof for the existence of mutually unbiased bases. *Algorithmica*, 34:512–528, 2002.

[41] D. Gottesman, A. Kitaev, and J. Preskill. Encoding a qubit in an oscillator. *Phys. Rev. A*, 64:012310, Jun 2001.

[42] J. Bae, B. C. Hiesmayr, and D. McNulty. Linking entanglement detection and state tomography via quantum 2-designs. *New Journal of Physics*, 21(1):013012, 2019.

[43] J. Bae, A. Bera, D. Chruściński, B. C. Hiesmayr, and D. McNulty. How many measurements are needed to detect bound entangled states? *arXiv:2108.01109 [quant-ph]*, 2021.

[44] C. Spengler, M. Huber, and B. C. Hiesmayr. A composite parameterization of unitary groups, density matrices and subspaces. *Journal of Physics A: Mathematical and Theoretical*, 43(385306), 2010.

[45] C. Spengler, M. Huber, and B. C. Hiesmayr. Composite parameterization and haar measure for all unitary and special unitary groups. *Journal of Physics A: Mathematical and Theoretical*, 53(013501), 2012.

[46] C. Spengler. Composite parameterization and haar measure for unitary groups. *Wolfram Library Archive, MathSource*, 2011.

[47] S. T. Flammia, A. Silberfarb, and C. M. Caves. Minimal informationally complete measurements for pure states. *Foundations of Physics*, 35:1985–2006, 2005.

[48] J. M. Renes, R. Blume-Kohout, A. J. Scott, and C. M. Caves. Symmetric informationally complete quantum measurements. *Journal of Mathematical Physics*, 45(6):2171–2180, 2004.

[49] T. DURT, B.-G. ENGLERT, I. BENGTSSON, and K. ŻYCZKOWSKI. On mutually unbiased bases. *International Journal of Quantum Information*, 08(04):535–640, 2010.

[50] H. Narnhofer. Entanglement reflected in wigner functions. *Journal of Physics A: Mathematical and General*, 39(22):7051, 2006.

[51] B. Baumgartner, B. C. Hiesmayr, and H. Narnhofer. State space for two qutrits has a phase space structure in its core. *Phys. Rev. A*, 74:032327, 2006.

[52] B. Baumgartner, B. Hiesmayr, and H. Narnhofer. The geometry of bipartite qutrits including bound entanglement. *Physics Letters A*, 372(13):2190–2195, 2008.

[53] S. A. Hill and W. K. Wootters. Entanglement of a pair of quantum bits. *Phys. Rev. Lett.*, 78:5022–5025, 1997.

[54] F. Mintert, M. Kuś, and A. Buchleitner. Concurrence of mixed multipartite quantum states. *Phys. Rev. Lett.*, 95:260502, 2005.

[55] W. K. Wootters. Entanglement of formation of an arbitrary state of two qubits. *Phys. Rev. Lett.*, 80:2245–2248, 1998.

[56] F. Mintert and A. Buchleitner. Concurrence of quasipure quantum states. *Phys. Rev. A*, 72:012336, 2005.

[57] B. C. Hiesmayr. Free versus bound entanglement, a np-hard problem tackled by machine learning. *Scientific Reports*, 11(19739), 2021.

[58] D. M. Appleby, H. Yadsan-Appleby, and G. Zauner. Galois automorphisms of a symmetric measurement. *arXiv:1209.1813 [math-ph]*, 2012.

[59] G. Zauner. SIC fiducials. `http://www.gerhardzauner.at/sicfiducials.html`, 2010–2012. Last accessed 27 September 2022.

[60] M. Horodecki and P. Horodecki. Reduction criterion of separability and limits for a class of distillation protocols. *Phys. Rev. A*, 59:4206–4216, 1999.

A. Appendix

Supplemental Results of $\mathscr{C}_{GSIC}$

Bipartite Qutrit Systems – Incomplete GSIC-POVMs

Let us come back to the GSIC criteria for $d = 3$ as discussed in the seventh chapter. Leaving out one GSIC operator P_i we obtain in total 9 different GSIC criteria $\mathscr{C}_{GSIC\setminus P_i}$. The bounds of all $\mathscr{C}_{GSIC\setminus P_i}$ are given in equations (7.4) and (7.5). Previously, we discussed the results of $\mathscr{C}_{GSIC\setminus P_5}$ and $\mathscr{C}_{GSIC\setminus P_7}$ for families A1, B1, B2, and B3. The remaining cases are shown in figures A.1–A.7. Their results are very similar to those of $\mathscr{C}_{GSIC\setminus P_5}$ and $\mathscr{C}_{GSIC\setminus P_7}$. The differences are rather subtle and do not change the overall findings. Neither of the criteria obtains any bound entanglement, and we detect only free entangled states in family A1.

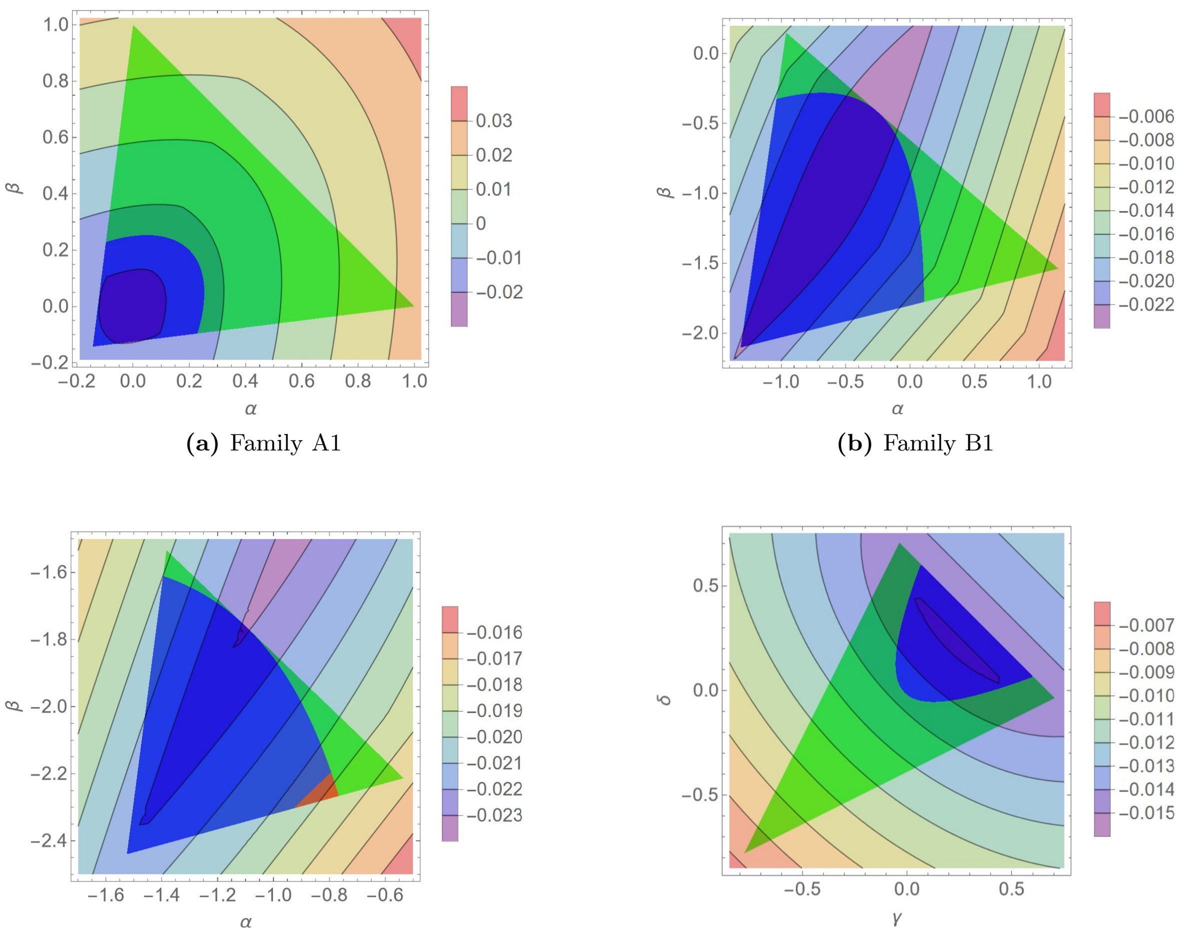

(a) Family A1

(b) Family B1

(c) Family B2

(d) Family B3

Figure A.1.: The results of $\mathscr{C}_{GSIC\setminus P_1}$ are represented by the rainbow spectra. In (c) the red shapes show the regions in which the MUB witness consisting of three mutually unbiased bases detects bound entanglement.

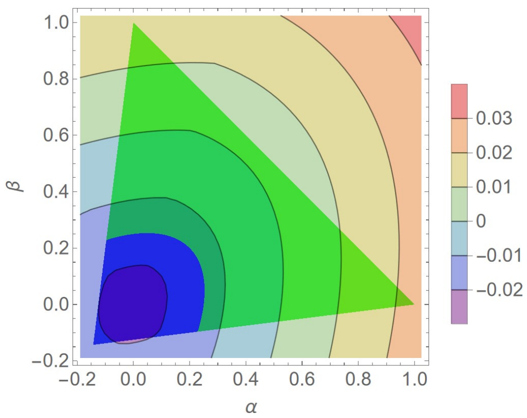

(a) Family A1

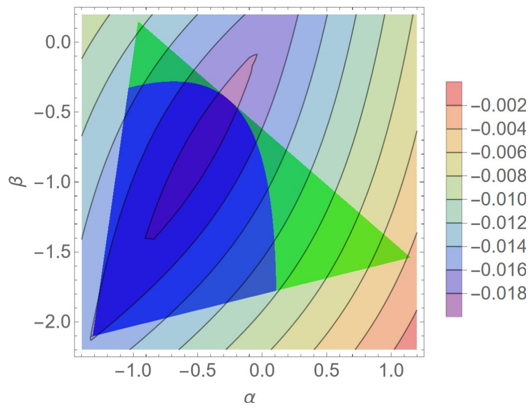

(b) Family B1

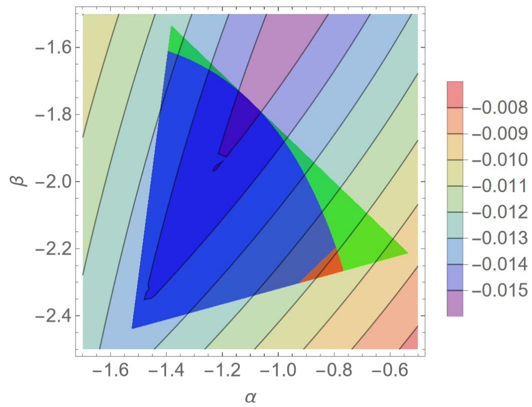

(c) Family B2

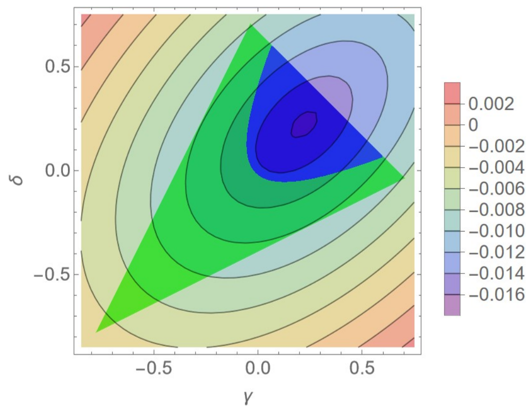

(d) Family B3

Figure A.2.: The results of $\mathscr{C}_{GSIC \setminus P_2}$ are represented by the rainbow spectra. In (c) the red shapes show the regions in which the MUB witness consisting of three mutually unbiased bases detects bound entanglement.

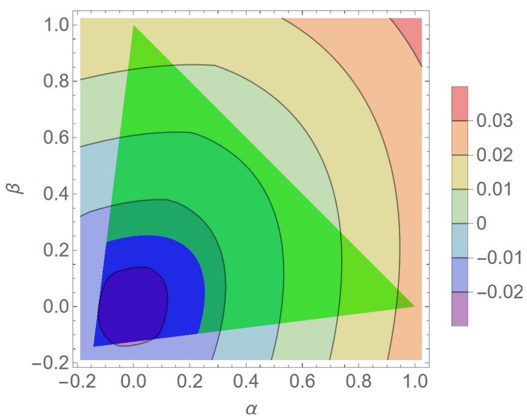

(a) Family A1

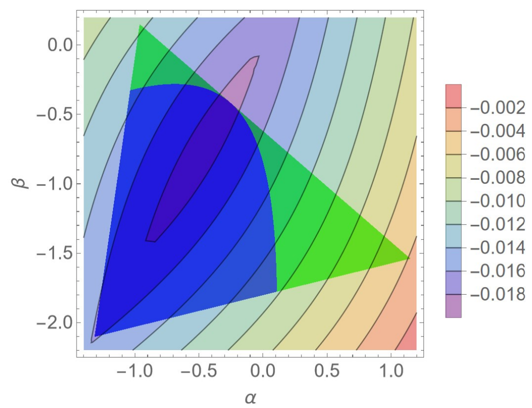

(b) Family B1

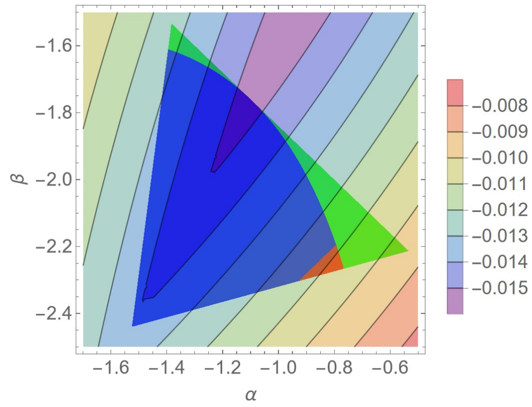

(c) Family B2

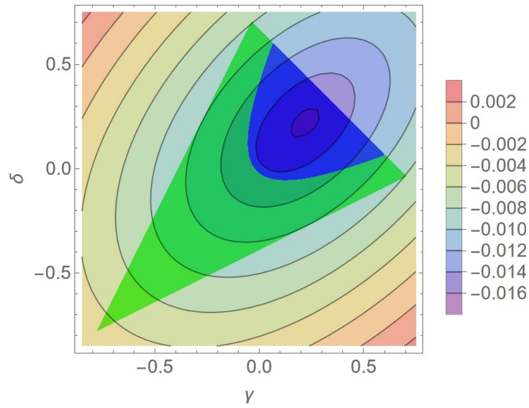

(d) Family B3

Figure A.3.: The results of $\mathscr{C}_{GSIC\setminus P_3}$ are represented by the rainbow spectra. In (c) the red shapes show the regions in which the MUB witness consisting of three mutually unbiased bases detects bound entanglement.

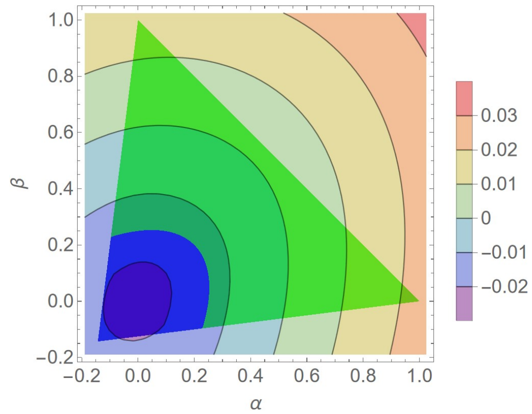

(a) Family A1

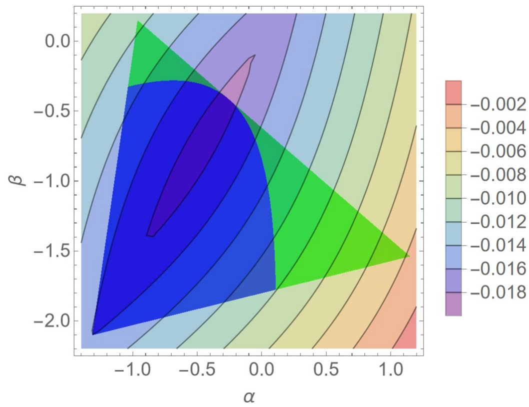

(b) Family B1

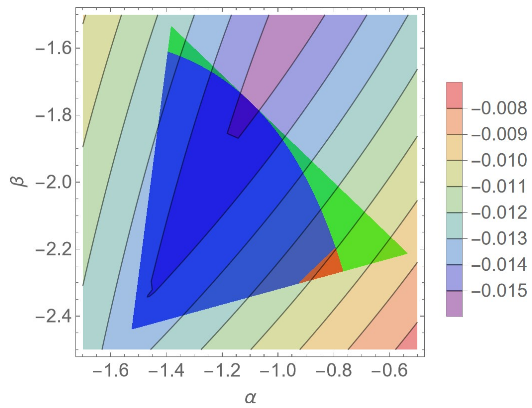

(c) Family B2

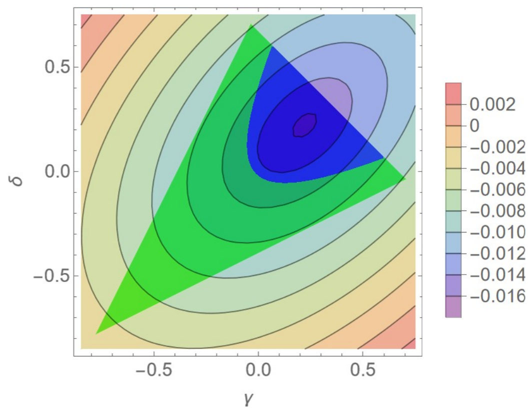

(d) Family B3

Figure A.4.: The results of $\mathscr{C}_{GSIC\setminus P_4}$ are represented by the rainbow spectra. In (c) the red shapes show the regions in which the MUB witness consisting of three mutually unbiased bases detects bound entanglement.

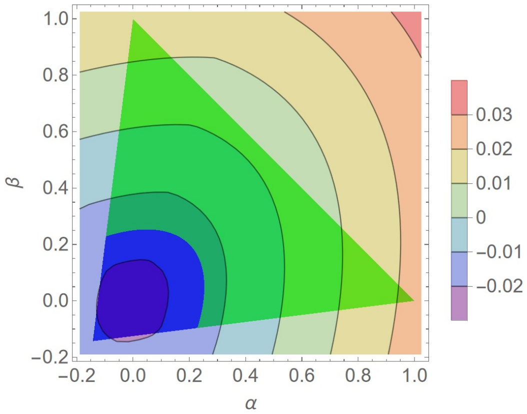

(a) Family A1

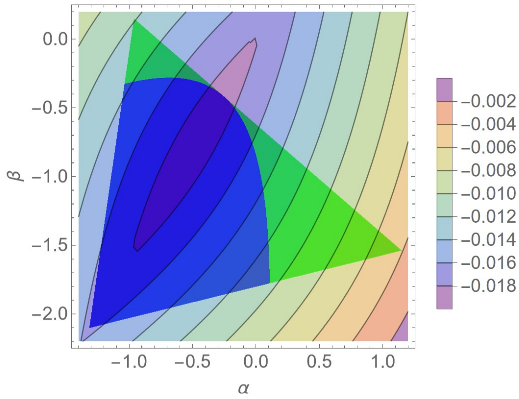

(b) Family B1

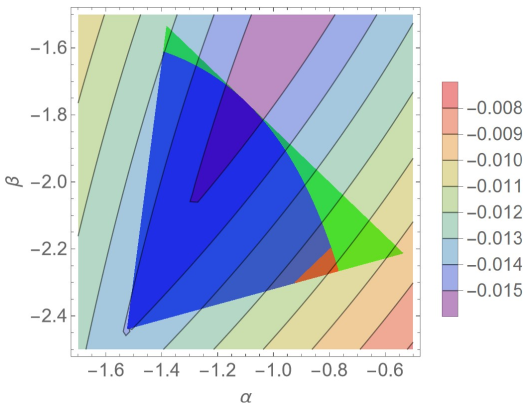

(c) Family B2

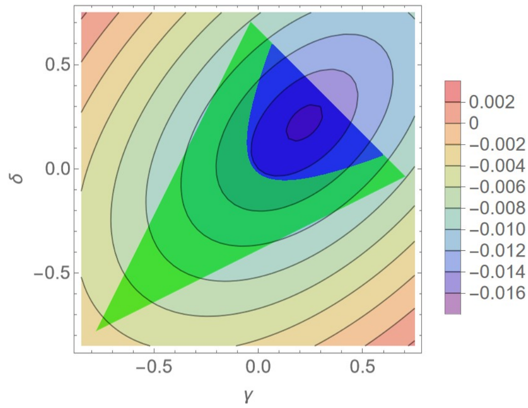

(d) Family B3

Figure A.5.: The results of $\mathscr{C}_{GSIC \setminus P_6}$ are represented by the rainbow spectra. In (c) the red shapes show the regions in which the MUB witness consisting of three mutually unbiased bases detects bound entanglement.

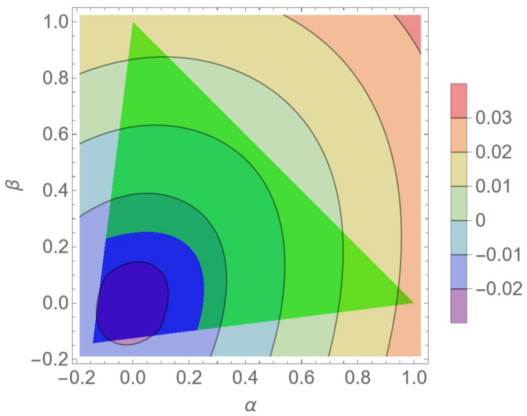

(a) Family A1

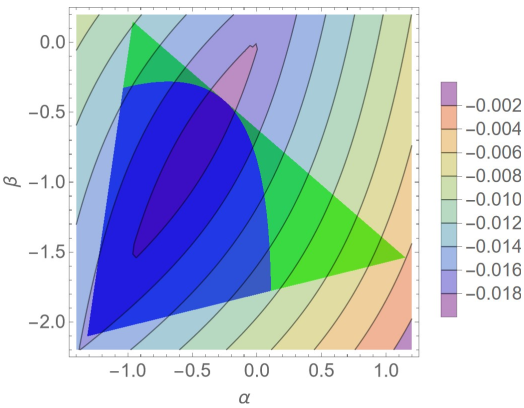

(b) Family B1

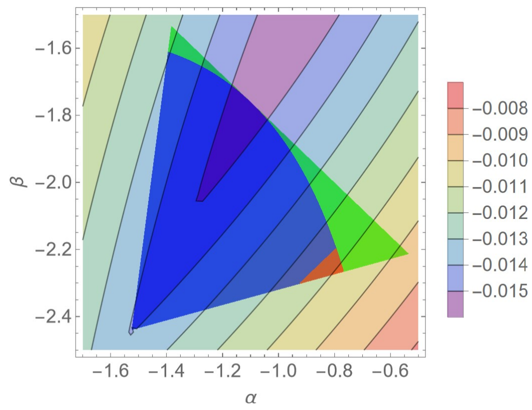

(c) Family B2

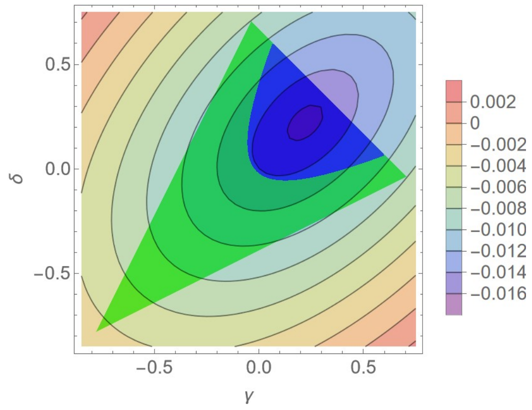

(d) Family B3

Figure A.6.: The results of $\mathscr{C}_{GSIC\setminus P_8}$ are represented by the rainbow spectra. In (c) the red shapes show the regions in which the MUB witness consisting of three mutually unbiased bases detects bound entanglement.

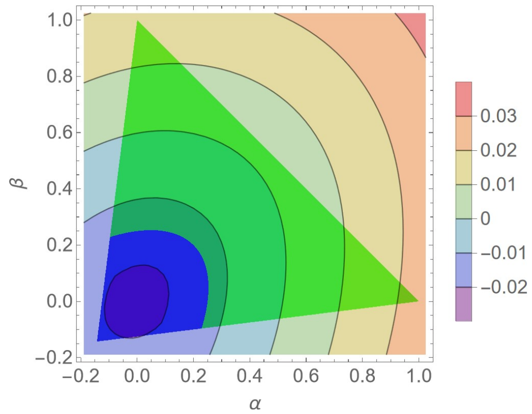

(a) Family A1

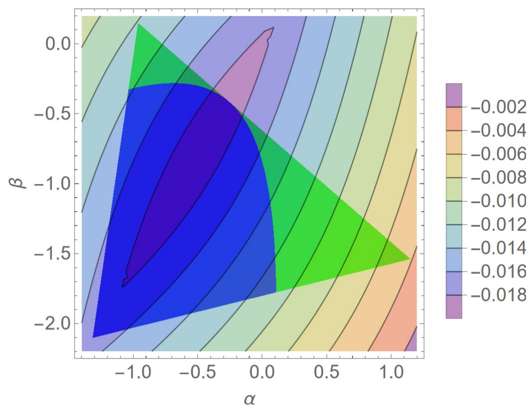

(b) Family B1

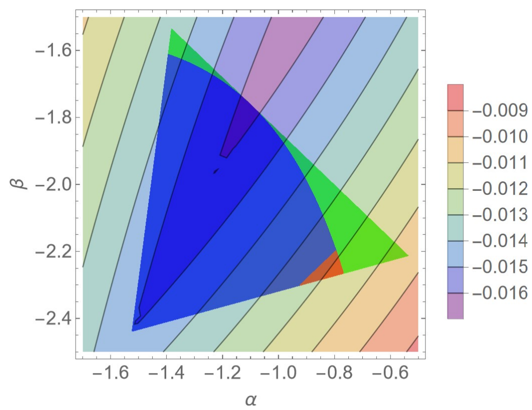

(c) Family B2

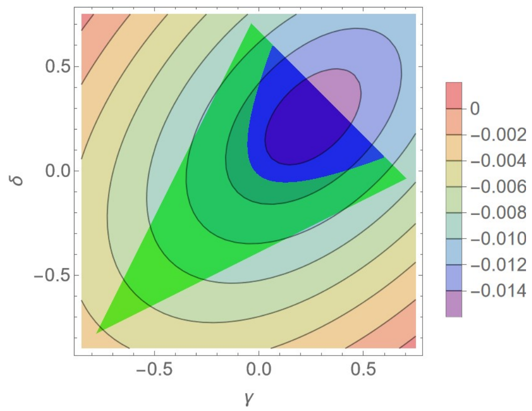

(d) Family B3

Figure A.7.: The results of $\mathscr{C}_{GSIC\setminus P_9}$ are represented by the rainbow spectra. In (c) the red shapes show the regions in which the MUB witness consisting of three mutually unbiased bases detects bound entanglement.

Higher Dimensions

Let us consider the GSIC-POVMs that emerge from equation (5.7) for the cases $d = \{4, 5, 6\}$. We can use these measurements to obtain $\mathscr{C}_{GSIC}$ for bipartite ququart, ququint, and qusixt states. The resulting GSIC criteria detect entanglement if

$$\begin{aligned}
\mathscr{C}_{GSIC} &= \|\mathcal{P}\|_{Tr} - \frac{16a+1}{20} > 0, \quad \text{for } d = 4, \\
\mathscr{C}_{GSIC} &= \|\mathcal{P}\|_{Tr} - \frac{25a+1}{30} > 0, \quad \text{for } d = 5, \\
\mathscr{C}_{GSIC} &= \|\mathcal{P}\|_{Tr} - \frac{36a+1}{42} > 0, \quad \text{for } d = 6.
\end{aligned} \tag{A.1}$$

Thereby, the allowed values of the parameter t lie in the intervals

$$\begin{aligned}
&t \in [-0.0037, 0.0043]\backslash\{0\}, \quad \text{for } d = 4, \\
&t \in [-0.0015, 0.0018]\backslash\{0\}, \quad \text{for } d = 5, \\
&t \in [-0.00073, 0.00092]\backslash\{0\}, \quad \text{for } d = 6.
\end{aligned} \tag{A.2}$$

For the examined state families, we achieve maximal violations of the separability bounds by setting $t = \{0.0043, 0.0018, 0.00092\}$ for $d = \{4, 5, 6\}$.
Figures A.8–A.10 show the results of $\mathscr{C}_{GSIC}$ in families K4, K5a, K5b, K6a, and K6b. In family K4 $\mathscr{C}_{GSIC}$ obtains the same bound entangled area as the MUB witness, and in families K5a and K5b $\mathscr{C}_{GSIC}$ detects even larger bound entangled regions than the MUB witness. For families K6a and K6b, we compare the results of $\mathscr{C}_{GSIC}$ with the outcomes of the generalized linear witness. It turns out that in both families $\mathscr{C}_{GSIC}$ obtains larger bound entangled areas. In all state families discussed the entangled states detected by $\mathscr{C}_{GSIC}$ coincidence with those detected by $\mathscr{C}_{SIC}$. The only difference between the results of the two criteria is that $\mathscr{C}_{SIC}$ produces a steeper gradient.

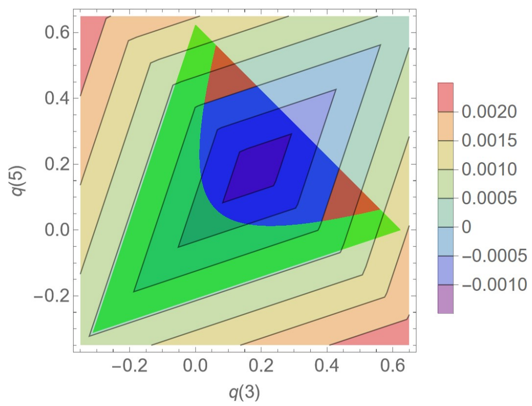

Figure A.8.: Family K4. The result of $\mathscr{C}_{GSIC}$ is represented by the rainbow spectrum. The red shapes show the regions in which the MUB witness detects bound entanglement.

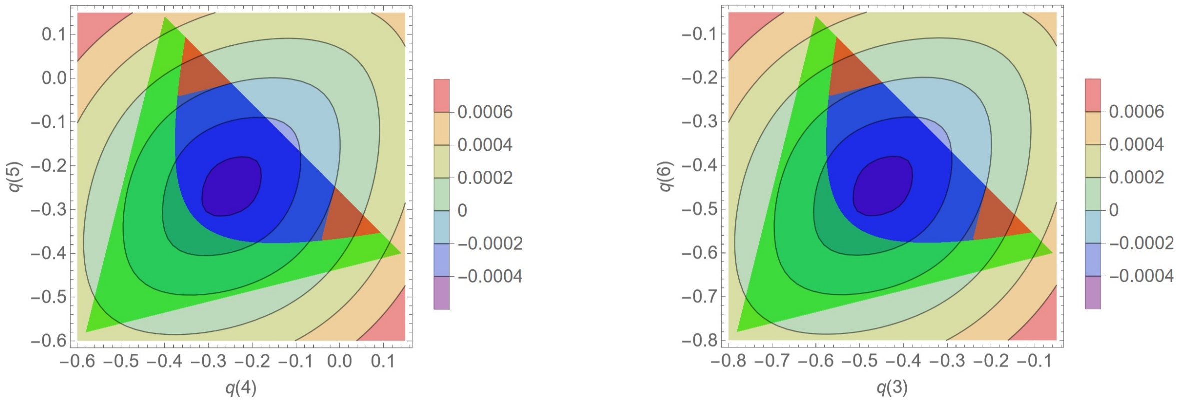

(a) Family K5a **(b)** Family K5b

Figure A.9.: The results of $\mathscr{C}_{GSIC}$ are represented by the rainbow spectrum. The red shapes show the regions in which the MUB witness detects bound entanglement.

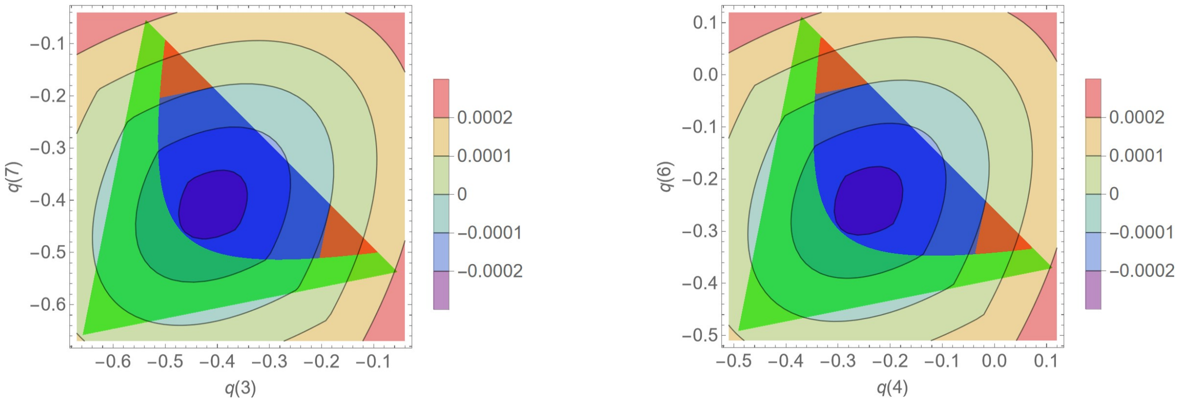

(a) Family K6a **(b)** Family K6b

Figure A.10.: The results of $\mathscr{C}_{GSIC}$ are represented by the rainbow spectrum. The red shapes show the regions in which the generalized linear witness detects bound entanglement.

SIC Vectors

By using equation (5.15) as well as the fiducial vectors from equations (7.8), (7.10), and (7.12), we construct complete set of SIC vectors for $d = \{4, 5, 6\}$.

$d = 4$

$$|S_1\rangle = \begin{pmatrix} \frac{1}{2}\sqrt{\frac{1}{10}\left(2+\sqrt{2}\right)\left(5-\sqrt{5}\right)} \\ \frac{\left(\frac{1}{4}-\frac{i}{4}\right)\left(\sqrt{2}+(1-i)\right)\left(-1+\sqrt{5}+(1+i)\sqrt{1+\sqrt{5}}\right)}{\sqrt{2\left(2+\sqrt{2}\right)\left(5-\sqrt{5}\right)}} \\ \frac{i\left(\sqrt{5}-5\right)}{2\sqrt{5\left(2+\sqrt{2}\right)\left(5-\sqrt{5}\right)}} \\ \frac{\left(\frac{1}{4}-\frac{i}{4}\right)\left(\sqrt{2}+(1-i)\right)\left(-1+\sqrt{5}-(1+i)\sqrt{1+\sqrt{5}}\right)}{\sqrt{2\left(2+\sqrt{2}\right)\left(5-\sqrt{5}\right)}} \end{pmatrix}, \quad |S_2\rangle = \begin{pmatrix} \frac{1}{2}\sqrt{\frac{1}{10}\left(2+\sqrt{2}\right)\left(5-\sqrt{5}\right)} \\ \frac{\left(\frac{1}{4}+\frac{i}{4}\right)\left(\sqrt{2}+(1-i)\right)\left(-1+\sqrt{5}+(1+i)\sqrt{1+\sqrt{5}}\right)}{\sqrt{2\left(2+\sqrt{2}\right)\left(5-\sqrt{5}\right)}} \\ -\frac{i\left(\sqrt{5}-5\right)}{2\sqrt{5\left(2+\sqrt{2}\right)\left(5-\sqrt{5}\right)}} \\ -\frac{\left(\frac{1}{4}+\frac{i}{4}\right)\left(\sqrt{2}+(1-i)\right)\left(-1+\sqrt{5}-(1+i)\sqrt{1+\sqrt{5}}\right)}{\sqrt{2\left(2+\sqrt{2}\right)\left(5-\sqrt{5}\right)}} \end{pmatrix}, \tag{A.3}$$

$$|S_3\rangle = \begin{pmatrix} \frac{1}{2}\sqrt{\frac{1}{10}\left(2+\sqrt{2}\right)\left(5-\sqrt{5}\right)} \\ -\frac{\left(\frac{1}{4}-\frac{i}{4}\right)\left(\sqrt{2}+(1-i)\right)\left(-1+\sqrt{5}+(1+i)\sqrt{1+\sqrt{5}}\right)}{\sqrt{2\left(2+\sqrt{2}\right)\left(5-\sqrt{5}\right)}} \\ \frac{i\left(\sqrt{5}-5\right)}{2\sqrt{5\left(2+\sqrt{2}\right)\left(5-\sqrt{5}\right)}} \\ -\frac{\left(\frac{1}{4}-\frac{i}{4}\right)\left(\sqrt{2}+(1-i)\right)\left(-1+\sqrt{5}-(1+i)\sqrt{1+\sqrt{5}}\right)}{\sqrt{2\left(2+\sqrt{2}\right)\left(5-\sqrt{5}\right)}} \end{pmatrix}, \quad |S_4\rangle = \begin{pmatrix} \frac{1}{2}\sqrt{\frac{1}{10}\left(2+\sqrt{2}\right)\left(5-\sqrt{5}\right)} \\ -\frac{\left(\frac{1}{4}+\frac{i}{4}\right)\left(\sqrt{2}+(1-i)\right)\left(-1+\sqrt{5}+(1+i)\sqrt{1+\sqrt{5}}\right)}{\sqrt{2\left(2+\sqrt{2}\right)\left(5-\sqrt{5}\right)}} \\ -\frac{i\left(\sqrt{5}-5\right)}{2\sqrt{5\left(2+\sqrt{2}\right)\left(5-\sqrt{5}\right)}} \\ \frac{\left(\frac{1}{4}+\frac{i}{4}\right)\left(\sqrt{2}+(1-i)\right)\left(-1+\sqrt{5}-(1+i)\sqrt{1+\sqrt{5}}\right)}{\sqrt{2\left(2+\sqrt{2}\right)\left(5-\sqrt{5}\right)}} \end{pmatrix},$$

$$|S_5\rangle = \begin{pmatrix} \frac{\left(\frac{1}{4}-\frac{i}{4}\right)\left(\sqrt{2}+(1-i)\right)\left(-1+\sqrt{5}-(1+i)\sqrt{1+\sqrt{5}}\right)}{\sqrt{2\left(2+\sqrt{2}\right)\left(5-\sqrt{5}\right)}} \\ \frac{1}{2}\sqrt{\frac{1}{10}\left(2+\sqrt{2}\right)\left(5-\sqrt{5}\right)} \\ \frac{\left(\frac{1}{4}-\frac{i}{4}\right)\left(\sqrt{2}+(1-i)\right)\left(-1+\sqrt{5}+(1+i)\sqrt{1+\sqrt{5}}\right)}{\sqrt{2\left(2+\sqrt{2}\right)\left(5-\sqrt{5}\right)}} \\ \frac{i\left(\sqrt{5}-5\right)}{2\sqrt{5\left(2+\sqrt{2}\right)\left(5-\sqrt{5}\right)}} \end{pmatrix}, \quad |S_6\rangle = \begin{pmatrix} -\frac{i\left(\sqrt{2}+(1-i)\right)\left(-1+\sqrt{5}-(1+i)\sqrt{1+\sqrt{5}}\right)}{4\sqrt{\left(2+\sqrt{2}\right)\left(5-\sqrt{5}\right)}} \\ \left(\frac{1}{4}+\frac{i}{4}\right)\sqrt{\frac{1}{5}\left(2+\sqrt{2}\right)\left(5-\sqrt{5}\right)} \\ \frac{\left((1+i)+i\sqrt{2}\right)\left(-1+\sqrt{5}+(1+i)\sqrt{1+\sqrt{5}}\right)}{4\sqrt{\left(2+\sqrt{2}\right)\left(5-\sqrt{5}\right)}} \\ \left(-\frac{1}{2}+\frac{i}{2}\right)\sqrt{\frac{5-\sqrt{5}}{10\left(2+\sqrt{2}\right)}} \end{pmatrix},$$

$$|S_7\rangle = \begin{pmatrix} -\frac{\left(\frac{1}{4}+\frac{i}{4}\right)\left(\sqrt{2}+(1-i)\right)\left(-1+\sqrt{5}-(1+i)\sqrt{1+\sqrt{5}}\right)}{\sqrt{2\left(2+\sqrt{2}\right)\left(5-\sqrt{5}\right)}} \\ \frac{1}{2}i\sqrt{\frac{1}{10}\left(2+\sqrt{2}\right)\left(5-\sqrt{5}\right)} \\ -\frac{\left(\frac{1}{4}+\frac{i}{4}\right)\left(\sqrt{2}+(1-i)\right)\left(-1+\sqrt{5}+(1+i)\sqrt{1+\sqrt{5}}\right)}{\sqrt{2\left(2+\sqrt{2}\right)\left(5-\sqrt{5}\right)}} \\ \frac{1}{2}\sqrt{\frac{5-\sqrt{5}}{5\left(2+\sqrt{2}\right)}} \end{pmatrix}, \quad |S_8\rangle = \begin{pmatrix} -\frac{\left(\sqrt{2}+(1-i)\right)\left(-1+\sqrt{5}-(1+i)\sqrt{1+\sqrt{5}}\right)}{4\sqrt{\left(2+\sqrt{2}\right)\left(5-\sqrt{5}\right)}} \\ \left(-\frac{1}{4}+\frac{i}{4}\right)\sqrt{\frac{1}{5}\left(2+\sqrt{2}\right)\left(5-\sqrt{5}\right)} \\ \frac{\left(\sqrt{2}+(1-i)\right)\left(-1+\sqrt{5}+(1+i)\sqrt{1+\sqrt{5}}\right)}{4\sqrt{\left(2+\sqrt{2}\right)\left(5-\sqrt{5}\right)}} \\ \frac{\left(\frac{1}{2}+\frac{i}{2}\right)\left(\sqrt{5}-5\right)}{\sqrt{10\left(2+\sqrt{2}\right)\left(5-\sqrt{5}\right)}} \end{pmatrix},$$

$$|S_9\rangle = \begin{pmatrix} \frac{i\left(\sqrt{5}-5\right)}{2\sqrt{5\left(2+\sqrt{2}\right)\left(5-\sqrt{5}\right)}} \\ \frac{\left(\frac{1}{4}-\frac{i}{4}\right)\left(\sqrt{2}+(1-i)\right)\left(-1+\sqrt{5}-(1+i)\sqrt{1+\sqrt{5}}\right)}{\sqrt{2\left(2+\sqrt{2}\right)\left(5-\sqrt{5}\right)}} \\ \frac{1}{2}\sqrt{\frac{1}{10}\left(2+\sqrt{2}\right)\left(5-\sqrt{5}\right)} \\ \frac{\left(\frac{1}{4}-\frac{i}{4}\right)\left(\sqrt{2}+(1-i)\right)\left(-1+\sqrt{5}+(1+i)\sqrt{1+\sqrt{5}}\right)}{\sqrt{2\left(2+\sqrt{2}\right)\left(5-\sqrt{5}\right)}} \end{pmatrix}, \quad |S_{10}\rangle = \begin{pmatrix} \frac{\sqrt{5}-5}{2\sqrt{5\left(2+\sqrt{2}\right)\left(5-\sqrt{5}\right)}} \\ \frac{\left(\frac{1}{4}-\frac{i}{4}\right)\left(\sqrt{2}+(1-i)\right)\left(-1+\sqrt{5}-(1+i)\sqrt{1+\sqrt{5}}\right)}{\sqrt{2\left(2+\sqrt{2}\right)\left(5-\sqrt{5}\right)}} \\ \frac{1}{2}i\sqrt{\frac{1}{10}\left(2+\sqrt{2}\right)\left(5-\sqrt{5}\right)} \\ -\frac{\left(\frac{1}{4}-\frac{i}{4}\right)\left(\sqrt{2}+(1-i)\right)\left(-1+\sqrt{5}+(1+i)\sqrt{1+\sqrt{5}}\right)}{\sqrt{2\left(2+\sqrt{2}\right)\left(5-\sqrt{5}\right)}} \end{pmatrix},$$

$$|S_{11}\rangle = \begin{pmatrix} -\frac{i\left(\sqrt{5}-5\right)}{2\sqrt{5\left(2+\sqrt{2}\right)\left(5-\sqrt{5}\right)}} \\ \frac{\left(\frac{1}{4}-\frac{i}{4}\right)\left(\sqrt{2}+(1-i)\right)\left(-1+\sqrt{5}-(1+i)\sqrt{1+\sqrt{5}}\right)}{\sqrt{2\left(2+\sqrt{2}\right)\left(5-\sqrt{5}\right)}} \\ -\frac{1}{2}\sqrt{\frac{1}{10}\left(2+\sqrt{2}\right)\left(5-\sqrt{5}\right)} \\ \frac{\left(\frac{1}{4}-\frac{i}{4}\right)\left(\sqrt{2}+(1-i)\right)\left(-1+\sqrt{5}+(1+i)\sqrt{1+\sqrt{5}}\right)}{\sqrt{2\left(2+\sqrt{2}\right)\left(5-\sqrt{5}\right)}} \end{pmatrix}, \quad |S_{12}\rangle = \begin{pmatrix} \frac{1}{2}\sqrt{\frac{5-\sqrt{5}}{5\left(2+\sqrt{2}\right)}} \\ \frac{\left(\frac{1}{4}-\frac{i}{4}\right)\left(\sqrt{2}+(1-i)\right)\left(-1+\sqrt{5}-(1+i)\sqrt{1+\sqrt{5}}\right)}{\sqrt{2\left(2+\sqrt{2}\right)\left(5-\sqrt{5}\right)}} \\ -\frac{1}{2}i\sqrt{\frac{1}{10}\left(2+\sqrt{2}\right)\left(5-\sqrt{5}\right)} \\ -\frac{\left(\frac{1}{4}-\frac{i}{4}\right)\left(\sqrt{2}+(1-i)\right)\left(-1+\sqrt{5}+(1+i)\sqrt{1+\sqrt{5}}\right)}{\sqrt{2\left(2+\sqrt{2}\right)\left(5-\sqrt{5}\right)}} \end{pmatrix},$$

$$|S_{13}\rangle = \begin{pmatrix} \frac{\left(\frac{1}{4}-\frac{i}{4}\right)\left(\sqrt{2}+(1-i)\right)\left(-1+\sqrt{5}+(1+i)\sqrt{1+\sqrt{5}}\right)}{\sqrt{2\left(2+\sqrt{2}\right)\left(5-\sqrt{5}\right)}} \\ \frac{i\left(\sqrt{5}-5\right)}{2\sqrt{5\left(2+\sqrt{2}\right)\left(5-\sqrt{5}\right)}} \\ \frac{\left(\frac{1}{4}-\frac{i}{4}\right)\left(\sqrt{2}+(1-i)\right)\left(-1+\sqrt{5}-(1+i)\sqrt{1+\sqrt{5}}\right)}{\sqrt{2\left(2+\sqrt{2}\right)\left(5-\sqrt{5}\right)}} \\ \frac{1}{2}\sqrt{\frac{1}{10}\left(2+\sqrt{2}\right)\left(5-\sqrt{5}\right)} \end{pmatrix}, \quad |S_{14}\rangle = \begin{pmatrix} -\frac{\left(\sqrt{2}+(1-i)\right)\left(-1+\sqrt{5}+(1+i)\sqrt{1+\sqrt{5}}\right)}{4\sqrt{\left(2+\sqrt{2}\right)\left(5-\sqrt{5}\right)}} \\ \frac{\left(\frac{1}{2}+\frac{i}{2}\right)\left(\sqrt{5}-5\right)}{\sqrt{10\left(2+\sqrt{2}\right)\left(5-\sqrt{5}\right)}} \\ \frac{\left(\sqrt{2}+(1-i)\right)\left(-1+\sqrt{5}-(1+i)\sqrt{1+\sqrt{5}}\right)}{4\sqrt{\left(2+\sqrt{2}\right)\left(5-\sqrt{5}\right)}} \\ \left(-\frac{1}{4}+\frac{i}{4}\right)\sqrt{\frac{1}{5}\left(2+\sqrt{2}\right)\left(5-\sqrt{5}\right)} \end{pmatrix},$$

$$|S_{15}\rangle = \begin{pmatrix} \frac{\left(\frac{1}{4}+\frac{i}{4}\right)\left(\sqrt{2}+(1-i)\right)\left(-1+\sqrt{5}+(1+i)\sqrt{1+\sqrt{5}}\right)}{\sqrt{2\left(2+\sqrt{2}\right)\left(5-\sqrt{5}\right)}} \\ \frac{\sqrt{5}-5}{2\sqrt{5\left(2+\sqrt{2}\right)\left(5-\sqrt{5}\right)}} \\ \frac{\left(\frac{1}{4}+\frac{i}{4}\right)\left(\sqrt{2}+(1-i)\right)\left(-1+\sqrt{5}-(1+i)\sqrt{1+\sqrt{5}}\right)}{\sqrt{2\left(2+\sqrt{2}\right)\left(5-\sqrt{5}\right)}} \\ -\frac{1}{2}i\sqrt{\frac{1}{10}\left(2+\sqrt{2}\right)\left(5-\sqrt{5}\right)} \end{pmatrix}, \quad |S_{16}\rangle = \begin{pmatrix} -\frac{i\left(\sqrt{2}+(1-i)\right)\left(-1+\sqrt{5}+(1+i)\sqrt{1+\sqrt{5}}\right)}{4\sqrt{\left(2+\sqrt{2}\right)\left(5-\sqrt{5}\right)}} \\ \left(-\frac{1}{2}+\frac{i}{2}\right)\sqrt{\frac{5-\sqrt{5}}{10\left(2+\sqrt{2}\right)}} \\ \frac{\left((1+i)+i\sqrt{2}\right)\left(-1+\sqrt{5}-(1+i)\sqrt{1+\sqrt{5}}\right)}{4\sqrt{\left(2+\sqrt{2}\right)\left(5-\sqrt{5}\right)}} \\ \left(\frac{1}{4}+\frac{i}{4}\right)\sqrt{\frac{1}{5}\left(2+\sqrt{2}\right)\left(5-\sqrt{5}\right)} \end{pmatrix}.$$

$d = 5$

$$|S_1\rangle = \begin{pmatrix} 0.391045 \\ -0.284866 - 0.647129i \\ -0.231884 - 0.198204i \\ 0.131939 - 0.109396i \\ 0.430967 + 0.197474i \end{pmatrix}, \quad |S_2\rangle = \begin{pmatrix} 0.391045 \\ 0.527428 - 0.470897i \\ 0.304099 + 0.0240524i \\ -0.171042 + 0.0109517i \\ 0.320985 - 0.348852i \end{pmatrix},$$

$$|S_3\rangle = \begin{pmatrix} 0.391045 \\ 0.610834 + 0.356099i \\ -0.260159 + 0.159286i \\ 0.144813 + 0.0916758i \\ -0.232588 - 0.413076i \end{pmatrix}, \quad |S_4\rangle = \begin{pmatrix} 0.391045 \\ -0.149912 + 0.690978i \\ 0.116847 - 0.281783i \\ -0.0632705 - 0.159286i \\ -0.464732 + 0.0935564i \end{pmatrix},$$

$$|S_5\rangle = \begin{pmatrix} 0.391045 \\ -0.703485 + 0.0709493i \\ 0.0710966 + 0.296648i \\ -0.0424392 + 0.166055i \\ -0.0546327 + 0.470897i \end{pmatrix}, \quad |S_6\rangle = \begin{pmatrix} 0.430967 + 0.197474i \\ 0.391045 \\ -0.284866 - 0.647129i \\ -0.231884 - 0.198204i \\ 0.131939 - 0.109396i \end{pmatrix}, \tag{A.4}$$

$$|S_7\rangle = \begin{pmatrix} 0.464732 - 0.0935564i \\ 0.316362 + 0.22985i \\ 0.703485 - 0.0709493i \\ 0.231884 + 0.198204i \\ -0.144813 - 0.0916758i \end{pmatrix}, \quad |S_8\rangle = \begin{pmatrix} 0.320985 - 0.348852i \\ 0.12084 + 0.371906i \\ -0.149912 + 0.690978i \\ -0.231884 - 0.198204i \\ -0.0424392 + 0.166055i \end{pmatrix},$$

$$|S_9\rangle = \begin{pmatrix} 0.0546327 - 0.470897i \\ -0.12084 + 0.371906i \\ -0.610834 - 0.356099i \\ 0.231884 + 0.198204i \\ 0.171042 - 0.0109517i \end{pmatrix}, \quad |S_{10}\rangle = \begin{pmatrix} -0.232588 - 0.413076i \\ -0.316362 + 0.22985i \\ 0.527428 - 0.470897i \\ -0.231884 - 0.198204i \\ -0.0632705 - 0.159286i \end{pmatrix},$$

$$|S_{11}\rangle = \begin{pmatrix} 0.131939 - 0.109396i \\ 0.430967 + 0.197474i \\ 0.391045 \\ -0.284866 - 0.647129i \\ -0.231884 - 0.198204i \end{pmatrix}, \quad |S_{12}\rangle = \begin{pmatrix} -0.0632705 - 0.159286i \\ 0.430967 + 0.197474i \\ 0.12084 + 0.371906i \\ 0.610834 + 0.356099i \\ 0.0710966 + 0.296648i \end{pmatrix},$$

$$|S_{13}\rangle = \begin{pmatrix} -0.171042 + 0.0109517i \\ 0.430967 + 0.197474i \\ -0.316362 + 0.22985i \\ -0.703485 + 0.0709493i \\ 0.116847 - 0.281783i \end{pmatrix}, \quad |S_{14}\rangle = \begin{pmatrix} -0.0424392 + 0.166055i \\ 0.430967 + 0.197474i \\ -0.316362 - 0.22985i \\ 0.527428 - 0.470897i \\ -0.260159 + 0.159286i \end{pmatrix},$$

$$|S_{15}\rangle = \begin{pmatrix} 0.144813 + 0.0916758i \\ 0.430967 + 0.197474i \\ 0.12084 - 0.371906i \\ -0.149912 + 0.690978i \\ 0.304099 + 0.0240524i \end{pmatrix}, \quad |S_{16}\rangle = \begin{pmatrix} -0.231884 - 0.198204i \\ 0.131939 - 0.109396i \\ 0.430967 + 0.197474i \\ 0.391045 \\ -0.284866 - 0.647129i \end{pmatrix},$$

$$|S_{17}\rangle = \begin{pmatrix} -0.116847 + 0.281783i \\ 0.0424392 - 0.166055i \\ 0.232588 + 0.413076i \\ -0.12084 + 0.371906i \\ 0.284866 + 0.647129i \end{pmatrix}, \quad |S_{18}\rangle = \begin{pmatrix} 0.304099 + 0.0240524i \\ -0.0632705 - 0.159286i \\ -0.0546327 + 0.470897i \\ -0.316362 - 0.22985i \\ -0.284866 - 0.647129i \end{pmatrix},$$

$$|S_{19}\rangle = \begin{pmatrix} -0.0710966 - 0.296648i \\ -0.144813 - 0.0916758i \\ -0.320985 + 0.348852i \\ 0.316362 - 0.22985i \\ 0.284866 + 0.647129i \end{pmatrix}, \quad |S_{20}\rangle = \begin{pmatrix} -0.260159 + 0.159286i \\ -0.171042 + 0.0109517i \\ -0.464732 + 0.0935564i \\ 0.12084 + 0.371906i \\ -0.284866 - 0.647129i \end{pmatrix},$$

$$|S_{21}\rangle = \begin{pmatrix} -0.284866 - 0.647129i \\ -0.231884 - 0.198204i \\ 0.131939 - 0.109396i \\ 0.430967 + 0.197474i \\ 0.391045 \end{pmatrix}, \quad |S_{22}\rangle = \begin{pmatrix} -0.149912 + 0.690978i \\ -0.260159 + 0.159286i \\ 0.131939 - 0.109396i \\ -0.0546327 + 0.470897i \\ -0.316362 + 0.22985i \end{pmatrix},$$

$$|S_{23}\rangle = \begin{pmatrix} 0.527428 - 0.470897i \\ 0.0710966 + 0.296648i \\ 0.131939 - 0.109396i \\ -0.464732 + 0.0935564i \\ 0.12084 - 0.371906i \end{pmatrix}, \quad |S_{24}\rangle = \begin{pmatrix} -0.703485 + 0.0709493i \\ 0.304099 + 0.0240524i \\ 0.131939 - 0.109396i \\ -0.232588 - 0.413076i \\ 0.12084 + 0.371906i \end{pmatrix},$$

$$|S_{25}\rangle = \begin{pmatrix} 0.610834 + 0.356099i \\ 0.116847 - 0.281783i \\ 0.131939 - 0.109396i \\ 0.320985 - 0.348852i \\ -0.316362 - 0.22985i \end{pmatrix}.$$

$d = 6$

$$|S_1\rangle = \begin{pmatrix} 0.524447 \\ 0.025929 - 0.618186i \\ -0.128062 - 0.107276i \\ -0.360183 - 0.335003i \\ 0.0897671 - 0.00266531i \\ 0.180588 - 0.177725i \end{pmatrix}, \quad |S_2\rangle = \begin{pmatrix} 0.524447 \\ 0.548329 - 0.286638i \\ 0.156935 - 0.0572665i \\ 0.360183 + 0.335003i \\ -0.0471918 - 0.0764079i \\ -0.0636204 - 0.245256i \end{pmatrix},$$

$$|S_3\rangle = \begin{pmatrix} 0.524447 \\ 0.5224 + 0.331548i \\ -0.0288731 + 0.164543i \\ -0.360183 - 0.335003i \\ -0.0425753 + 0.0790732i \\ -0.244208 - 0.067531i \end{pmatrix}, \quad |S_4\rangle = \begin{pmatrix} 0.524447 \\ -0.025929 + 0.618186i \\ -0.128062 - 0.107276i \\ 0.360183 + 0.335003i \\ 0.0897671 - 0.00266531i \\ -0.180588 + 0.177725i \end{pmatrix}, \tag{A.5}$$

$$|S_5\rangle = \begin{pmatrix} 0.524447 \\ -0.548329 + 0.286638i \\ 0.156935 - 0.0572665i \\ -0.360183 - 0.335003i \\ -0.0471918 - 0.0764079i \\ 0.0636204 + 0.245256i \end{pmatrix}, \quad |S_6\rangle = \begin{pmatrix} 0.524447 \\ -0.5224 - 0.331548i \\ -0.0288731 + 0.164543i \\ 0.360183 + 0.335003i \\ -0.0425753 + 0.0790732i \\ 0.244208 + 0.067531i \end{pmatrix},$$

$$|S_7\rangle = \begin{pmatrix} 0.180588 - 0.177725i \\ 0.524447 \\ 0.025929 - 0.618186i \\ -0.128062 - 0.107276i \\ -0.360183 - 0.335003i \\ 0.0897671 - 0.00266531i \end{pmatrix}, \quad |S_8\rangle = \begin{pmatrix} 0.067531 - 0.244208i \\ 0.454184 + 0.262223i \\ 0.618186 + 0.025929i \\ 0.164543 + 0.0288731i \\ 0.144426 + 0.470212i \\ -0.00266531 - 0.0897671i \end{pmatrix},$$

$$|S_9\rangle = \begin{pmatrix} -0.0636204 - 0.245256i \\ 0.262223 + 0.454184i \\ -0.025929 + 0.618186i \\ -0.156935 + 0.0572665i \\ 0.110029 - 0.479429i \\ -0.0897671 + 0.00266531i \end{pmatrix}, \quad |S_{10}\rangle = \begin{pmatrix} -0.177725 - 0.180588i \\ 0. + 0.524447i \\ -0.618186 - 0.025929i \\ 0.107276 - 0.128062i \\ -0.335003 + 0.360183i \\ 0.00266531 + 0.0897671i \end{pmatrix},$$

$$|S_{11}\rangle = \begin{pmatrix} -0.244208 - 0.067531i \\ -0.262223 + 0.454184i \\ 0.025929 - 0.618186i \\ -0.0288731 + 0.164543i \\ 0.470212 - 0.144426i \\ 0.0897671 - 0.00266531i \end{pmatrix}, \quad |S_{12}\rangle = \begin{pmatrix} -0.245256 + 0.0636204i \\ -0.454184 + 0.262223i \\ 0.618186 + 0.025929i \\ -0.0572665 - 0.156935i \\ -0.479429 - 0.110029i \\ -0.00266531 - 0.0897671i \end{pmatrix},$$

$$|S_{13}\rangle = \begin{pmatrix} 0.0897671 - 0.00266531i \\ 0.180588 - 0.177725i \\ 0.524447 \\ 0.025929 - 0.618186i \\ -0.128062 - 0.107276i \\ -0.360183 - 0.335003i \end{pmatrix}, \quad |S_{14}\rangle = \begin{pmatrix} 0.0425753 - 0.0790732i \\ 0.180588 - 0.177725i \\ 0.262223 + 0.454184i \\ 0.5224 + 0.331548i \\ 0.128062 + 0.107276i \\ -0.110029 + 0.479429i \end{pmatrix},$$

$$|S_{15}\rangle = \begin{pmatrix} -0.0471918 - 0.0764079i \\ 0.180588 - 0.177725i \\ -0.262223 + 0.454184i \\ -0.548329 + 0.286638i \\ -0.128062 - 0.107276i \\ 0.470212 - 0.144426i \end{pmatrix}, \quad |S_{16}\rangle = \begin{pmatrix} -0.0897671 + 0.00266531i \\ 0.180588 - 0.177725i \\ -0.524447 \\ 0.025929 - 0.618186i \\ 0.128062 + 0.107276i \\ -0.360183 - 0.335003i \end{pmatrix},$$

$$|S_{17}\rangle = \begin{pmatrix} -0.0425753 + 0.0790732i \\ 0.180588 - 0.177725i \\ -0.262223 - 0.454184i \\ 0.5224 + 0.331548i \\ -0.128062 - 0.107276i \\ -0.110029 + 0.479429i \end{pmatrix}, \quad |S_{18}\rangle = \begin{pmatrix} 0.0471918 + 0.0764079i \\ 0.180588 - 0.177725i \\ 0.262223 - 0.454184i \\ -0.548329 + 0.286638i \\ 0.128062 + 0.107276i \\ 0.470212 - 0.144426i \end{pmatrix},$$

$$|S_{19}\rangle = \begin{pmatrix} -0.360183 - 0.335003i \\ 0.0897671 - 0.00266531i \\ 0.180588 - 0.177725i \\ 0.524447 \\ 0.025929 - 0.618186i \\ -0.128062 - 0.107276i \end{pmatrix}, \quad |S_{20}\rangle = \begin{pmatrix} -0.335003 + 0.360183i \\ 0.0764079 - 0.0471918i \\ 0.245256 - 0.0636204i \\ 0. + 0.524447i \\ 0.286638 + 0.548329i \\ 0.0572665 + 0.156935i \end{pmatrix},$$

$$|S_{21}\rangle = \begin{pmatrix} 0.360183 + 0.335003i \\ 0.0425753 - 0.0790732i \\ 0.244208 + 0.067531i \\ -0.524447 \\ -0.5224 - 0.331548i \\ 0.0288731 - 0.164543i \end{pmatrix}, \quad |S_{22}\rangle = \begin{pmatrix} 0.335003 - 0.360183i \\ -0.00266531 - 0.0897671i \\ 0.177725 + 0.180588i \\ 0. - 0.524447i \\ 0.618186 + 0.025929i \\ -0.107276 + 0.128062i \end{pmatrix},$$

$$|S_{23}\rangle = \begin{pmatrix} -0.360183 - 0.335003i \\ -0.0471918 - 0.0764079i \\ 0.0636204 + 0.245256i \\ 0.524447 \\ -0.548329 + 0.286638i \\ 0.156935 - 0.0572665i \end{pmatrix}, \quad |S_{24}\rangle = \begin{pmatrix} -0.335003 + 0.360183i \\ -0.0790732 - 0.0425753i \\ -0.067531 + 0.244208i \\ 0. + 0.524447i \\ 0.331548 - 0.5224i \\ -0.164543 - 0.0288731i \end{pmatrix},$$

$$|S_{25}\rangle = \begin{pmatrix} -0.128062 - 0.107276i \\ -0.360183 - 0.335003i \\ 0.0897671 - 0.00266531i \\ 0.180588 - 0.177725i \\ 0.524447 \\ 0.025929 - 0.618186i \end{pmatrix}, \quad |S_{26}\rangle = \begin{pmatrix} -0.0288731 + 0.164543i \\ -0.470212 + 0.144426i \\ 0.0897671 - 0.00266531i \\ 0.244208 + 0.067531i \\ -0.262223 + 0.454184i \\ -0.025929 + 0.618186i \end{pmatrix},$$

$$|S_{27}\rangle = \begin{pmatrix} 0.156935 - 0.0572665i \\ -0.110029 + 0.479429i \\ 0.0897671 - 0.00266531i \\ 0.0636204 + 0.245256i \\ -0.262223 - 0.454184i \\ 0.025929 - 0.618186i \end{pmatrix}, \quad |S_{28}\rangle = \begin{pmatrix} -0.128062 - 0.107276i \\ 0.360183 + 0.335003i \\ 0.0897671 - 0.00266531i \\ -0.180588 + 0.177725i \\ 0.524447 \\ -0.025929 + 0.618186i \end{pmatrix},$$

$$|S_{29}\rangle = \begin{pmatrix} -0.0288731 + 0.164543i \\ 0.470212 - 0.144426i \\ 0.0897671 - 0.00266531i \\ -0.244208 - 0.067531i \\ -0.262223 + 0.454184i \\ 0.025929 - 0.618186i \end{pmatrix}, \quad |S_{30}\rangle = \begin{pmatrix} 0.156935 - 0.0572665i \\ 0.110029 - 0.479429i \\ 0.0897671 - 0.00266531i \\ -0.0636204 - 0.245256i \\ -0.262223 - 0.454184i \\ -0.025929 + 0.618186i \end{pmatrix},$$

$$|S_{31}\rangle = \begin{pmatrix} 0.025929 - 0.618186i \\ -0.128062 - 0.107276i \\ -0.360183 - 0.335003i \\ 0.0897671 - 0.00266531i \\ 0.180588 - 0.177725i \\ 0.524447 \end{pmatrix}, \quad |S_{32}\rangle = \begin{pmatrix} -0.331548 + 0.5224i \\ -0.107276 + 0.128062i \\ -0.479429 - 0.110029i \\ 0.0790732 + 0.0425753i \\ 0.177725 + 0.180588i \\ -0.454184 + 0.262223i \end{pmatrix},$$

$$|S_{33}\rangle = \begin{pmatrix} 0.548329 - 0.286638i \\ 0.128062 + 0.107276i \\ -0.470212 + 0.144426i \\ 0.0471918 + 0.0764079i \\ -0.180588 + 0.177725i \\ 0.262223 - 0.454184i \end{pmatrix}, \quad |S_{34}\rangle = \begin{pmatrix} -0.618186 - 0.025929i \\ 0.107276 - 0.128062i \\ -0.335003 + 0.360183i \\ 0.00266531 + 0.0897671i \\ -0.177725 - 0.180588i \\ 0. + 0.524447i \end{pmatrix},$$

$$|S_{35}\rangle = \begin{pmatrix} 0.5224 + 0.331548i \\ -0.128062 - 0.107276i \\ -0.110029 + 0.479429i \\ -0.0425753 + 0.0790732i \\ 0.180588 - 0.177725i \\ -0.262223 - 0.454184i \end{pmatrix}, \quad |S_{36}\rangle = \begin{pmatrix} -0.286638 - 0.548329i \\ -0.107276 + 0.128062i \\ 0.144426 + 0.470212i \\ -0.0764079 + 0.0471918i \\ 0.177725 + 0.180588i \\ 0.454184 + 0.262223i \end{pmatrix}.$$